DYNAMICS OF MINERALIZATION DURING BONE DEVELOPMENT

by

John-David P. McElderry

A dissertation submitted in partial fulfillment
of the requirements for the degree of
Doctor of Philosophy
(Chemistry)
in The University of Michigan
2012

Doctoral Committee:

Professor Michael D. Morris, Chair
Professor Zhan Chen
Professor Renny Franceschi
Professor Robert T. Kennedy

ACKNOWLEDGMENTS

The work comprised in this thesis is based on a number of invaluable learning experiences from friends and colleagues. The best classroom setting I found myself in was just sitting down with my colleagues to sort out our ideas on a pad of paper. My adviser, Dr. Michael Morris, treated me as an expert spectroscopist from the beginning and placed great responsibility upon my shoulders. He created a work environment where my efforts were valued. I am deeply grateful for the many hours he put into sorting through my data alongside me. My collaborator and cognate committee member, Dr. Renny Franceschi, acted as a second adviser throughout my PhD. He guided my research into paths that I have found to be truly fascinating.

Lastly, my darling wife, Kristin has been an endless source of optimism and support through the whole process. She encouraged me to set goals for my PhD and to achieve them by setting smaller goals weekly and monthly. She has been a trusted confidant and a loyal friend. I cannot possibly document the ways she has improved my experience here at the University of Michigan.

CONTENTS

LIST OF FIGURES

LIST OF TABLES

LIST OF APPENDICES

ABSTRACT

Mineralization is an important process in bone growth, development and regeneration. Mineral deposition and crystallization in tissue are protein-mediated processes where the properties of the mineral are largely dictated by the function of specific proteins. Currently, the mechanism of mineralization is a hotly debated topic. The focus of this thesis is to better understand the dynamic process of mineral formation in bone and to identify physiological influences that affect the mineral pathway or the mineral product. First, the effect of carbonate substitution on crystal properties was explored using a series of B-type carbonated apatites (0.2–10.5 wt% CO_3^{2-}). It was determined that apatite crystal size is dependent on carbonate substitution due to the amount of strain it puts on the crystal lattice. Next, mineralization kinetics was observed in actively mineralizing *ex vivo* neonatal murine calvaria using Raman spectroscopy as a real-time monitor of mineral properties. Periodic deposition of apatitic mineral occurred with near-daily frequency for up to 6 days. Timing of the mineral events were compared to the expression of circadian-clock component *Period1* using a *firefly luciferase* bioluminescence reporter gene. The calvaria most actively deposited mineral in the early evening around 9pm. These experiments were repeated in calvaria infected with an adenovirus carrying the *bone sialoprotein* (BSP) gene. The resulting overexpression of BSP significantly modified the mineralization pathway. BSP induced formation of amorphous calcium phosphate during the first 30 hours followed by a transformation into

small hydrated crystals over 40 hours duration. Mineral growth was also observed in fractured murine tibiae after 5 weeks of healing. Both wild-type and *Brtl*/- mice were screened for mineral crystallinity and carbonate content. *Brtl*/- mice experienced a delay in mineralization by containing underdeveloped mineral with poor crystallinity and high carbonate content. Lastly, fresh murine femora were frozen and thawed several times to test the consistency of Raman bone quality metrics through the preservation of unfixed bone tissue. Collagen-matrix metrics were significantly affected after four freeze/thaw cycles. Mineral metrics were also affected but to a lesser degree. For Raman studies of fresh bone, one freeze/thawing is recommended.

CHAPTER I
PROCESSES OF MINERAL FORMATION IN MAMMALIAN BONE

1 Thesis Rationale

The discovery and development of the next generation of pharmaceutical agents for bone diseases rely on our understanding of the mechanisms of bone metabolism. Bone mineralization (calcification) is an important process in bone formation with bone mineral being a key component in calcium homeostasis and skeletal strength. Although the mineral is malformed in many metabolic bone diseases, causal relationships often cannot be established on the molecular level due to a general lack of understanding of the mechanism of mineral formation. By and large, bone mineral has been assumed to be a static material only capable of change through dissolution and reformation. However, in the brief time window of mineral deposition it is hypothesized that bone mineral is a dynamic solid that is susceptible to protein interactions, which dictate the characteristics of the mineral product. This thesis explores the dynamic nature of bone mineral during mineralization with the intent to identify important protein influences that affect mineral formation.

2 Introduction to Biomineralization

Mineralization is a process common to many organisms across all of the animal kingdoms.[1] In most organisms, mineral is formed within an organic matrix template by native physical and chemical processes.[2] The formation of tiny crystals within a shaped matrix can result in elaborate mineral patterns with complex symmetry. This can be seen in spiraled conch shells (calcite), needle-shaped or circular diatoms (silica), and even in petrified wood in which the dead cells of a tree serve as the template for quartz formation. Mammals also experience mineralization as part of a natural skeletal physiology. About 65% of total skeletal weight in humans can be attributed to bone mineral, the rest being the organic matrix.[3] Shape, size, crystal order, orientation, and even imperfections in the mineral are the culmination of physiological factors that fulfill two important functions: first, to add rigidity to the skeleton, and second to serve as a readily accessible ion store.[4]

Diverse formations can be found in different tissues in the body which can provide either rigidity (high mineral content) or flexibility (low mineral content), and can have specialized functions. For example bones in the inner ear have a high mineral content and so transmit sound waves efficiently. Also, tooth enamel contains elongated and highly crystalline mineral that can withstand enormous loads. Accessibility to the ions comprising bone mineral is crucial for many systems in the body. It is in a delicate equilibrium between free ions and the solid phase, readily dissolved and reformed according to necessity. For example, nursing mothers experience a decrease in bone density but return to normal levels after weaning. [5, 6]

Mineralization is a lifelong process. In fetal development, a complete cartilaginous skeleton with digits and joints is formed by 8 weeks gestation.[7] The first

signs of bone mineralization have been observed after 12 weeks, [8], however the bulk of mineralization occurs in the third trimester.[7] Cranial bones maintain soft tissue sutures through adolescence until after 20 years and some facial sutures remain patent until about 70 years of life. [9] Mineralization is also a key process in tissue repair during fracture healing.

3 Mineral Structure and Formation in Bone

Bone mineral is a crystalline material formed from regulated precipitation of calcium and phosphate ions. The most common crystal formed in bone has a hydroxyapatite-like structure, with a basic chemical formula $Ca_{10}(PO_4)_6(OH)_2$. Other crystals of the form $Ca_x(PO4)_y$ may occur in bone tissue, such as brushite, $CaHPO_4 \cdot 2H_2O$, and octacalcium phosphate (OCP), $Ca_8H_2(PO_4)_6 \cdot 5H_2O$; however these alternate formations are less stable than apatite at physiological pH and are most common in pathological bone.[1, 10] Tooth also contains hydroxyapatite-like mineral although it differs in shape, size and perfection.

Imperfections to the lattice are present in bone mineral and can have a significant effect on stability. Crystal stability is directly related to acid-base solubility[11] which has an important role in physiological processes which dissolve mineral, such as bone repair and calcium homeostatis. Imperfections are mainly caused by non-stoichiometric substitutions of ionic species which put strain on the crystal lattice. Common substitutions are Na^+, K^+, Mg^{2+}, Sr^{2+}, Fe^{2+}, Zn^{2+}, F-, Cl^-, and CO_3^{2-}.[12] These substitutions are regulated by size restraints, charge balance, and to some degree diet. Table 1 contains relative amounts of ionic substitutions commonly found in bone and

tooth mineral. The most prevalent substitution is that of carbonate which can be found at levels of 4–10 wt% in bone mineral. In contrast, dental enamel has a carbonate level of 1–4 wt% and is much more resistant to acid-dissolution. Carbonate is so essential to solubility that scientists refer to bone mineral as carbonated apatite (CAp). Carbonate can occupy two sites in the lattice. Substitution for phosphate ions, called B-type, is the majority of the carbonate substitution. A small amount of carbonate substitutes for hydroxyl ions, called A-type. Increased solubility in B-type carbonates is due in part to Ca^{2+}–CO_3^{2-} bonds being weaker than Ca^{2+}–PO_4^{3-} bonds. [12] Charge balance is maintained by a loss of Ca^{2+} neighboring the phosphate site. A-type carbonate induces a considerable amount of lattice strain due to the narrow channel into which carbonate must fit. In this case, charge balance is maintained with the loss of two OH^- for every one CO_3^{2-}. Synthetic apatites of the A-type typically require temperatures in excess of 1000°C while B-type typically will form at 50–100°C.[13, 14]

Crystal formation of bone apatite occurs in primarily two steps: nucleation and propagation. Nucleation is characterized by the aggregation of solution ions into an ordered structure with only a few unit cells. Following nucleation, the propagation step is the spontaneous precipitation of ions onto the face of pre-formed crystals. Willard Gibbs established classical nucleation theory (CNT) by describing the formation of spherical water droplets from vapor.[15] This has also been the accepted thermodynamic model for describing solid precipitation from solution for simple systems. CNT describes the nucleation process as a dynamic equilibrium between solvated ions and nanoscopic precipitated crystals. Because of high surface area, these nanoscopic crystals spontaneously redissolve. Only crystals above a certain critical size are stable enough to

continue in the crystal formation process. Figure 1.1 shows the combined effects of surface and volume free energies on crystal formation which illustrates the energy barrier that defines the critical size.

While it is helpful to picture the nucleation process in the context of CNT, there is considerable evidence that bone mineral does not nucleate immediately into the apatite structure.[1, 16-19] Posner described the nucleation of bone apatite as the formation of amorphous calcium phosphate clusters which eventually collapse into an ordered lattice structure.[20] These aggregates were later called Posner clusters. More recently Crane et al. showed that mineral deposited early in the bone formation process contains a considerable amount of HPO_4^{2-} which is characteristic of OCP.[17] The existence of a precursor state to apatite has not been agreed upon at this point because of the transient nature of the state and the difficulty of *in situ* observation.[18, 21, 22]

4 Role of Collagen in Mineralization

The mineralization process is facilitated by a type-I collagen matrix which serves as a template for mineral formation. The collagen matrix is the protein component of the overall structural composite and makes up about 90% of the total protein excreted by bone forming cells. The remainder is non-collagenous proteins which serve various physiological functions including the nucleation and inhibition of bone mineral formation.

Type-I collagen forms a 3-dimensional structure that extends throughout bone[1], and is also present in tendon. Collagen fibrils are elongated structures of parallel collagen units intertwined in either a woven structure which is randomly oriented, or a plywood-

like structure having ordered orientations of fibrils in layers. Each collagen unit is approximately 300 nm long and overlaps neighboring units by about 67 nm.[23] Fibrils contain gap regions of 40 nm between end-to-end collagen units. These are the accepted sites of mineral formation. Mineral size and shape are thought to be restricted by the gap region dimensions. This restriction is analogous to ice cubes frozen in a tray. Mineral formed in fibrils tend to be uniform, having a plate-like shape of approximately 45x25x5 nm. Interestingly, the longest dimension, the crystallographic c-axis, is aligned parallel to the collagen axis and has roughly the dimension of the gap region. Ectopic mineral which forms outside of the fibril tends to be larger crystals. However, Chen et al. challenged the gap-region size-restriction hypothesis by showing that when the organic component of mature bone is removed a continuous network of mineral remains intact.[24] This means that mineral in mature bone outgrows the gap region and interfaces with neighboring mineral. Therefore both mineral and matrix components of bone form a continuous 3-dimensional ultra-structure.

Collagen matrix has also been implicated as an active participant in mineralization beyond serving as a passive template. In 1973, Katz and Li [25] postulated that collagen catalyzes mineral nucleation with the diffusion of mineral ions into the fibril being the rate-limiting step. More recently, Nudelman et al. [16] showed evidence supporting the collagen-catalyst postulate by taking a series of 3-dimensional transmission electron micrographs (TEM) of horse tendon cryogenically frozen at various times in the midst of mineralization. They found Posner clusters adhered to the outside of the fibril at specific locations nearest the C-terminus of the collagen molecule. Molecular dynamic simulations of the system revealed that these clusters first form a negatively

charged complex with acidic proteins, then attach and enter into the fibril at the most positively charged site. Based on this evidence, electrostatic interaction governs the diffusion of ACP into collagen.

5 Role of Non-collagenous Proteins

Physiologic mineralization is a highly mediated process where non-collagenous proteins (NCPs) assist the nucleation and propagation of bone mineral, presumably in the gap regions of collagen fibrils. There are many proteins that are suspected of having a direct role in biomineralization. These have been reviewed recently by Gorski.[26]. Several SIBLING proteins (small integrin binding ligand, N-linked glycoproteins), particularly bone sialoprotein (BSP) and dentin matrix protein 1 (DMP1), have been shown to promote mineral nucleation in the extracellular matrix.[27, 28] Hunter and coworkers have shown that repeated acidic residues such as glutamic acid (Glu) present in BSP have high binding affinities to apatitic mineral.[29-33] BSP also contains chains of sialic acid which bind tightly to the alpha 2 chain of type-I collagen in the gap region.[34] He and coworkers showed that DMP1 also has high acidic residue content which forms a β-sheet and sequesters ions in solution before directing them to the N-terminus of the collagen protein in the gap region.[27, 35, 36] There is evidence showing that the acidic protein osteocalcin behaves as an inhibitor of nucleation in solution, however upon binding to a rigid scaffold behaves as a crystal nucleator. Although this has not yet been shown for BSP and DMP1, it is possible that the nucleating properties of the protein change as a function of binding to collagen and therefore can direct site specific mineralization.

6 Cellular Activity in Mineral Deposition and Absorption

Bone is a living organ which contains various types of cells working toward maintaining material strength and directing access to mineral stores. Bone maintenance requires the removal of damaged bone and the deposition of new bone. This is referred to as bone remodeling. Three cells are mainly responsible for remodeling. Osteoblasts are derived from multipotent mesenchymal stem cells (MSCs) which are also the precursors to myoblasts in muscle, chondrocytes in cartilage, and adipocytes in fat tissue.[37] Osteoblasts are the bone forming cells responsible for depositing osteoid which is the unmineralized organic matrix. Individual collagen strands are produced within the cell membrane and excreted to form fibrils in the extracellular space.[38] After the matrix is deposited, osteoblasts release mineral nucleating proteins that catalyze the mineralization process. Osteoblasts surround themselves with osteoid and end up completely encapsulated. These cells will then differentiate further into osteocytes.[39] Osteocytes are integral to the bone formation process because they are able to transduce mechanical stimulation into chemical signals to direct bone modeling/remodeling.[40] The third type of cell, osteoclasts, is derived from hematopoietic stem cells of a macrophage lineage.[41] These large cells attach to the bone surface and seal off a zone in preparation for bone resorption. Within the sealed zone the pH is acidic for inducing mineral dissolution and creating optimal conditions for enzymatic activity.[42] After osteoclasts leave the region, osteoblast progenitor cells are recruited to attach to the surface and deposit osteoid; and the process of bone mineralization begins again.

Pharmaceuticals for preventing bone loss due to systemic diseases have primarily targeted bone formation/resorption pathways on the cellular level. For example, post-menopausal osteoporosis is thought to be a condition of reduced osteoblast activity. This

disturbs the bone modeling/resorption balance and results in a net loss of bone over time. The most common drugs are catabolism inhibitors, which decrease resorption activity. Bisphosphonates (BPs), such as alendronate (Fosamax), zolendronic acid (Zometa), ibandronate (Boniva), and risedronate (Actonel) bind tightly to the surface of bone mineral and disrupt osteoclast activity. BP's all share the same general chemical formula $(PO_3)CXY(PO_3)$, where X and Y components can vary. Bisphosphonates bind much in the same way as pyrophosphate, but are more resistant to enzymatic hydrolysis. [43] Another anti-catabolic pharmaceutical agent for treating systemic bone loss is a RANK-ligand inhibitor (Denosumab), which disrupts signaling for osteoclast differentiation. There are only a few pharmaceuticals on the market that can be classified as true anabolic agents, which stimulate bone formation by increasing osteoblast activity. The only one currently used in the U.S. is the recombinant peptide of the 1-34 segment of human parathyroid hormone (PTH), also known as teriparatide (Forteo). In bone, PTH promotes osteoblast differentiation from MSCs thereby supplying the tissue with an increased number of bone forming cells. [44] Although these agents significantly impact the amount of mineral in the bone, bone fragility is not simply a matter of reduced mineral content. Rather, there is a growing body of evidence that shows that there are differences in mineral crystallinity and carbonate content that are associated with bone strength. [46-52] There are currently no pharmaceuticals that directly intervene in the mineralization process on the molecular level in part because the mechanism is still incompletely understood. However, when the roles of mineralizing proteins are better understood, it may be possible to design anabolic agents to specifically target steps in mineral formation to optimize mineral properties in regenerated bone tissue.

Table 1.1 Ionic composition of bovine cortical bone mineral from Ref [10]

Component	wt %
Ca^{2+}	36.6
PO_4^{3-}	17.1
CO_3^{2-}	4.8
Na^{+}	1.0
K^{+}	0.07
Mg^{2+}	0.6
Sr^{+}	0.05
Cl^{-}	0.1
F^{-}	0.1
Ca/P molar	1.65

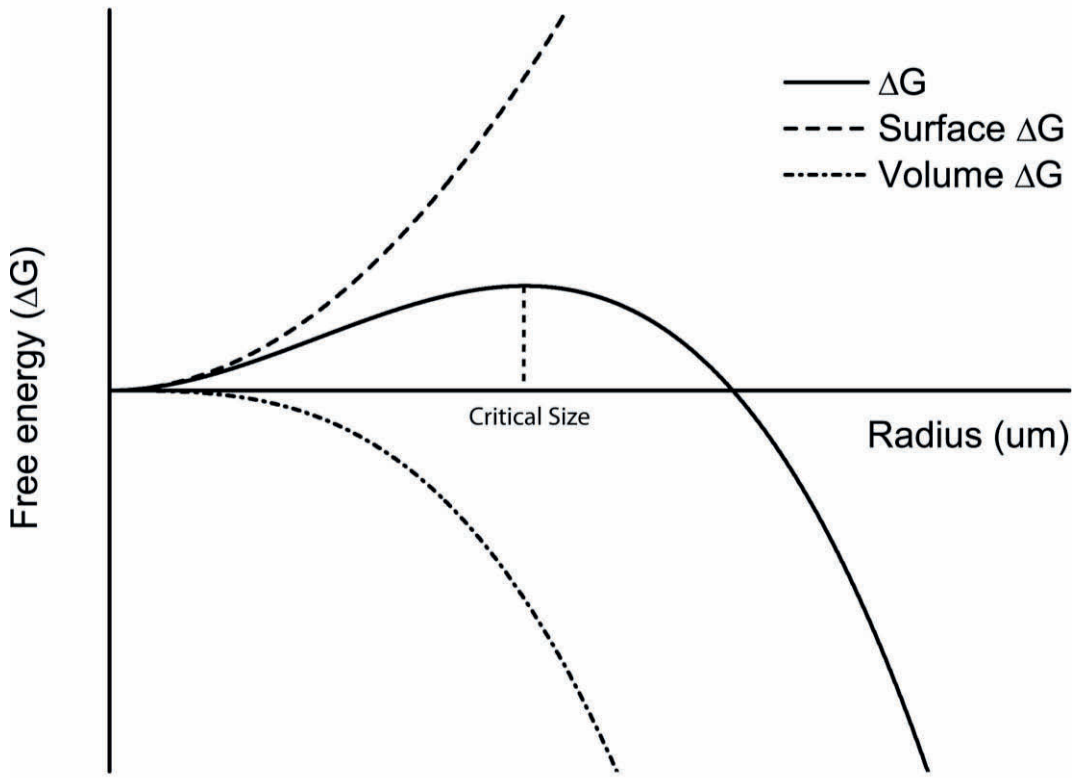

Figure 1.1 Free energy diagram illustrating the thermodynamics of classical nucleation theory in crystals. Formation of an energy barrier at a critical particle radius (r_c) is due to the sum of surface free energy ΔG_s and volume free energy ΔG_v relative to particle size. Figure adapted from Ref [15].

References

1. Lowenstam HA, Weiner S (1989) On Biomineralization. Oxford University Press, Inc., New York

2. Weiner S, Sagi I, Addadi L (2005) Structural biology. Choosing the crystallization path less traveled. Science 309:1027-1028

3. Trotter M, Hixon BB (1974) Sequential changes in weight, density, and percentage ash weight of human skeletons from an early fetal period through old age. Anat Rec 179:1-18

4. Neuman WF, Neuman MW (1953) The nature of the mineral phase of bone. Chem Rev 53:1-45

5. Wysolmerski JJ (2002) The evolutionary origins of maternal calcium and bone metabolism during lactation. J Mammary Gland Biol Neoplasia 7:267-276

6. Kovacs CS, Kronenberg HM (2006) Skeletal Physiology: Pregnancy and Lactation. In: Favus MJ (ed) Primer on the Metabolic Bone Diseases and Disorders of Mineral Metabolism. The American Society for Bone and Mineral Research, Washington D. C., p 63-67

7. Kovacs CS (2006) Skeletal Physiology: Fetus and Neonate. In: Favus MJ (ed) Primer on the Metabolic Bone Diseases and Disorders of Mineral Metabolism. The american Society for Bone and Mineral Research, Washington D. C., p 50-55

8. Oyedepo AC, Henshaw DL (1997) Calcification of the lumbar vertebrae during human fetal development. Calcif Tissue Int 61:179-182

9. Opperman LA (2000) Cranial sutures as intramembranous bone growth sites. Dev Dyn 219:472-485

10. Elliott JC (2002) Calcium phosphate biominerals. In: Kohn MJ, Rakovan J, Hughes JM (eds) Phosphates: Geochemical, Geobiological and Material impoertance, Reviews in Mineralogy and Geochemistry. Mineralogical Society of America, Washington, DC, p 631-672

11. Nelson DGA, Barry JC, Shields CP, Glena R, Featherstone JDB (1989) Crystal Morphology, Composition and Dissolution Behavior of Carbonated Apatites Prepared at Controlled pH and Temperature. Journal of Colloid and Interface Science 130:467-479

12. Wopenka B, Pasteris JD (2005) A mineralogical perspective on the apatite in bone. Materials Science & Engineering 25:131-143

13. Suetsugu Y, Shimoya I, Tanaka J (1998) Configuration of carbonate ions in apatite structure determined by polarized infrared spectroscopy. J. Am. Ceram. Soc. 81:746-746

14. Penel G, Leroy G, Rey C, Bres E (1998) MicroRaman Spectral Study of the PO4 and CO3 Vibrational Modes in Synthetic and Biological Apatites. Calcified Tissue International V63:475-481

15. Erdemir D, Lee AY, Myerson AS (2009) Nucleation of crystals from solution: classical and two-step models. Acc Chem Res 42:621-629

16. Nudelman F, Pieterse K, George A, Bomans PHH, Friedrich H, Brylka LJ, Hilbers PAJ, With Gd, Sommerdijk NAJM (2010) The role of collagen in bone apatite formation in the presence of hydroxyapatite nucleation inhibitors. Nature Materials 9:1004-1009

17. Crane NJ, Popescu V, Morris MD, Steenhuis P, Ignelzi JMA (2006) Raman spectroscopic evidence for octacalcium phosphate and other transient mineral species deposited during intramembranous mineralization. Bone 39:434-442

18. Weiner S (2006) Transient precursor strategy in mineral formation of bone. Bone 39:431-433

19. Dey A, Bomans PH, Muller FA, Will J, Frederik PM, de With G, Sommerdijk NA (2010) The role of prenucleation clusters in surface-induced calcium phosphate crystallization. Nat Mater 9:1010-1014

20. Posner AS, Betts F (1975) Synthetic amorphous calcium phosphate and its relation to bone mineral structure. Acc Chem Res 8:273-281

21. Grynpas MD, Omelon S (2007) Transient precursor strategy or very small biological apatite crystals? Bone 41:162-164

22. Colfen H (2010) Biomineralization: A crystal-clear view. Nat Mater 9:960-961

23. Wallace JM, Erickson B, Les CM, Orr BG, Banaszak Holl MM (2010) Distribution of type I collagen morphologies in bone: relation to estrogen depletion. Bone 46:1349-1354

24. Chen PY, Toroian D, Price PA, McKittrick J (2011) Minerals form a continuum phase in mature cancellous bone. Calcif Tissue Int 88:351-361

25. Katz EP, Li ST (1973) Structure and function of bone collagen fibrils. J Mol Biol 80:1-15

26. Gorski JP (2012) Biomineralization of bone: a fresh view of the roles of non-collagenous proteins. Front Biosci 17:2598-2621

27. He G, Dahl T, Veis A, George A (2003) Nucleation of apatite crystals in vitro by self-assembled dentin matrix protein 1. Nat Mater 2:552-558

28. Chen J, Shapiro HS, Sodek J (1992) Development expression of bone sialoprotein mRNA in rat mineralized connective tissues. J Bone Miner Res 7:987-997

29. Goldberg HA, Warner KJ, Stillman MJ, Hunter GK (1996) Determination of the hydroxyapatite-nucleating region of bone sialoprotein. Connect Tissue Res 35:385-392

30. Hunter GK, Goldberg HA (1994) Modulation of crystal formation by bone phosphoproteins: role of glutamic acid-rich sequences in the nucleation of hydroxyapatite by bone sialoprotein. Biochem J 302 (Pt 1):175-179

31. Hunter GK, Goldberg HA (1993) Nucleation of hydroxyapatite by bone sialoprotein. Proc Natl Acad Sci U S A 90:8562-8565

32. Hunter GK, Hauschka PV, Poole AR, Rosenberg LC, Goldberg HA (1996) Nucleation and inhibition of hydroxyapatite formation by mineralized tissue proteins. Biochem J 317 (Pt 1):59-64

33. Hunter GK, Kyle CL, Goldberg HA (1994) Modulation of crystal formation by bone phosphoproteins: structural specificity of the osteopontin-mediated inhibition of hydroxyapatite formation. Biochem J 300 (Pt 3):723-728

34. Fujisawa R, Nodasaka Y, Kuboki Y (1995) Further characterization of interaction between bone sialoprotein (BSP) and collagen. Calcif Tissue Int 56:140-144

35. He G, Gajjeraman S, Schultz D, Cookson D, Qin C, Butler WT, Hao J, George A (2005) Spatially and temporally controlled biomineralization is facilitated by interaction between self-assembled dentin matrix protein 1 and calcium phosphate nuclei in solution. Biochemistry 44:16140-16148

36. He G, George A (2004) Dentin matrix protein 1 immobilized on type I collagen fibrils facilitates apatite deposition in vitro. J Biol Chem 279:11649-11656

37. Aubin JE (2008) Mesenchymal Stem Cells and Osteoblast Differentiation. In: Bilezikian JP, Raisz LG, Martin TJ (eds) Principles of Bone Biology. Academic Press, Burlington, p 85-108

38. Kuivaniemi H, Tromp G, Prockop DJ (1991) Mutations in collagen genes: causes of rare and some common diseases in humans. FASEB J 5:2052-2060

39. Dallas SL, Bonewald LF (2010) Dynamics of the transition from osteoblast to osteocyte. Ann N Y Acad Sci 1192:437-443

40. Klein-Nulend J, Bonewald LF (2008) The Osteocyte. In: Bilezikian JP, Raisz LG, Martin TJ (eds) Principles of Bone Biology. Academic Press, Burlington, p 153-174

41. Takahashi N, Udagawa N, Kobayashi Y, Takami M, Martin TJ, Suda T (2008) Osteoclast Generation. In: Bilezikian JP, Raisz LG, Martin TJ (eds) Principles of Bone Biology. Academic Press, Burlington, p 175-192

42. Vaananen HK, Zhao H (2008) Osteoclast Function: Biology and Mechanisms. In: Bilezikian JP, Raisz LG, Martin TJ (eds) Principles of Bone Biology. Academic Press, Burlington, p 193-210

43. Roelofs AJ, Ebetino FH, Reszka AA, Russell RGG, Rogers MJ (2008) Bisphosphonates: Mechanisms of Action. In: Bilezikian JP, Raisz LG, Martin TJ (eds) Principles of Bone Biology. Academic Press, New York, p 1737-1768

44. Karaplis AC, Goltzman D (1999) PTHrP: Of Molecules, Mice, and Men. In: Seibel MJ, Robins SP, Bilezikian JP (eds) Dynamics of Bone and Cartilage Metabolism. Academic Press, San Diego, p 203-216

45. Neer RM, Arnaud CD, Zanchetta JR, Prince R, Gaich GA, Reginster JY, Hodsman AB, Eriksen EF, Ish-Shalom S, Genant HK, Wang O, Mitlak BH (2001) Effect of parathyroid hormone (1-34) on fractures and bone mineral density in postmenopausal women with osteoporosis. N Engl J Med 344:1434-1441

46. Burket J, Gourion-Arsiquaud S, Havill LM, Baker SP, Boskey AL, van der Meulen MC (2011) Microstructure and nanomechanical properties in osteons relate to tissue and animal age. J Biomech 44:277-284

47. Morris MD, Mandair GS (2011) Raman assessment of bone quality. Clin Orthop Relat Res 469:2160-2169

48. Donnelly E, Boskey AL, Baker SP, van der Meulen MC (2010) Effects of tissue age on bone tissue material composition and nanomechanical properties in the rat cortex. J Biomed Mater Res A 92:1048-1056

49. Ruppel ME, Miller LM, Burr DB (2008) The effect of the microscopic and nanoscale structure on bone fragility. Osteoporos Int 19:1251-1265

50. Paschalis EP, Mendelsohn R, Boskey AL (2011) Infrared assessment of bone quality: a review. Clin Orthop Relat Res 469:2170-2178

51. McCreadie BR, Morris MD, Chen TC, Sudhaker Rao D, Finney WF, Widjaja E, Goldstein SA (2006) Bone tissue compositional differences in women with and without osteoporotic fracture. Bone 39:1190-1195

52. Riggs BL, Parfitt AM (2005) Drugs used to treat osteoporosis: the critical need for a uniform nomenclature based on their action on bone remodeling. J Bone Miner Res 20:177-184

CHAPTER II
RAMAN INSTRUMENTATION AND ANALYSIS OF BONE MINERAL

1 Bone Mineral Analysis Techniques

Spectroscopy and crystallography have been important tools for studying the chemistry of bone mineral and model compounds. The first image of bone calcium absorption by x-rays was famously taken in 1895 when Wilhelm Röntgen took a radiograph of his wife's left hand. In 1926, X-ray crystallography was performed on bone mineral by W. F. DeJong, who published a diffraction pattern that resembled a poorly resolved pattern of hydroxyapatite. In the 1960's and 70's Posner et al. and other investigators incorporated infrared and Raman spectroscopies into their analysis of model compounds to better understand the role of carbonate and hydroxide ions on bone mineral structure and solubility.[1-3] In 1984, Glimcher et al. used phosphorous-31 magic angle spinning solid-state nuclear magnetic resonance (MAS NMR) to probe the chemical environment around the phosphate ion. [4, 5] Since then, this technique has been used to characterize the mineral surface and protein binding.[6-8] These techniques continue to contribute to the understanding of bone structure and function.

Raman and infrared spectroscopies have facilitated *in situ* studies of bone chemical composition, which eventually led to stainless chemical imaging of bone tissue.

Raman analysis became particularly useful for fresh tissue analysis because no tissue preparation is required. Even non-invasive Raman spectroscopy and low definition tomography is possible.[9] These techniques continue to be important tools for bone mineral analysis and have become useful for matrix protein analysis as well.

The work included in this dissertation relies heavily on Raman spectroscopy. Therefore a brief overview of Raman theory is included in this chapter along with a description of a Raman microscope suitable for extended time measurements. X-ray powder diffraction and solid-state NMR have also been used for data collection in this thesis as have other imaging techniques including atomic-force microscopy, fluorescence microscopy, bioluminescence microscopy, and micro-computed tomography. Descriptions of these techniques can be found in the chapters in which they are used.

The work included in this dissertation builds upon previous studies of bone mineral structure analysis by adding a time component to determine the *in situ* kinetics of mineral formation. A crystal size metric is defined in Chapter 6 for Raman and ^{31}P NMR spectroscopies for the purpose of assessing crystal growth dynamics. Chapter 3 explores the time-dependent behavior of normal developing bone tissue and its relation to circadian rhythms in the body. Perturbation to the normal dynamics of mineralization by overexpression of the nucleating protein BSP is discussed in Chapter 4. Chapter 5 discusses mineralization and collagen development in fracture healing cases in the presence of collagen defects and bisphosphonate treatment. Chapter 7 discusses the limits of freezing fresh bone for preservation in a Raman study.

2 Overview of Theory of Solid-state Raman Spectroscopy

The majority of the measurements discussed in this dissertation are of optical measurements on tissue, especially Raman spectroscopy. A basic understanding of the Raman effect in crystalline solids is useful. Similar to infra-red spectroscopy, Raman spectroscopy is a vibrational spectroscopy which probes the intramolecular and lattice vibrations of molecules. The Raman effect is a two-photon light scattering phenomenon in which energy is lost or gained through an inelastic process. Energy is exchanged between the incident photon and the interacting molecule. When a photon enters the vicinity of a molecule, its additional electric field induces a transient electronic state, called a virtual state, equal to the energy of the photon. The virtual state is a short-lived association between the photon and the molecule on the order of 10^{-14}–10^{-15} s.[10] During this period the added oscillations of the electric field induce a time-dependent dipole to form. This dipole can induce molecular motion or combine with preexisting molecular motion. The energy of the scattered photon can be

$$E_{scatter} = E_{incident} - E_{vibration} \quad (1)$$

$$= E_{incident} + E_{vibration} \quad (2)$$

$$= E_{incident} \quad (3)$$

where Eqn. 1 describes a Stokes shift, Eqn. 2 describes an anti-Stokes shift, and Eqn. 3 describes elastic scatter. Approximately one in every 10^7 photons is Raman-scattered and the remainder is elastically scattered (Rayleigh scatter). The basic measurement of Raman spectroscopy is $E_{vibration}$ and has the units cm^{-1} or wavenumber.

$E_{vibration}$ is indicative of the environment surrounding a molecular bond. A simple model for a bond is the harmonic oscillator, in which two masses are attached by a spring. The molecular forces (F) and the energy of vibration are approximated by

$$F = -k\Delta x \tag{4}$$

$$E_{vibration} = \frac{1}{2\pi}\left(n + \frac{1}{2}\right)\sqrt{\frac{k}{\mu}} \tag{5}$$

where Δx is mass displacement, k is the spring constant, n is the harmonic state of vibration, and μ is the reduced mass of the system.[11] In condensed matter, molecular vibrations are affected by neighboring molecules which in effect act as external springs pushing on the molecule in various directions. Although these interactions are much weaker than covalent bonds they can induce measurable changes on the effective spring constant of a system. Therefore, $E_{vibration}$ is sensitive to any change in the electronic environment immediately surrounding the molecule including solvation, hydrogen bonding, and steric constraints. A spectral band is the result of many photons originating from a distribution of vibrational environments for a molecular bond in the material. Amorphous materials, such as glass, have broad bands with widths in the range of 30 – 80 cm^{-1} whereas crystalline materials may have band widths in the range of 4–30 cm^{-1}. Energy distributions dependent on random events such as this have a Gaussian profile, G(v). There is also a sizeable contribution to broadening from uncertainty in $E_{scatter}$. Scattered photons can have a range of energies dependent on the life-time of the virtual state. Distributions of energies based on life-time broadening have a Lorentzian profile, L(v).[12] Therefore, the true band profile for a Raman band is the convolution of the two broadening functions, called the Voigt function:

$$Raman\ Profile = (L * G)(v) \tag{6}$$

The Voigt function is difficult to use in routine calculations and is commonly approximated by a linear combination of the two functions, called a pseudo-Voigt function:

$$Raman\ Profile = cL(v) + (1 - c)G(v) \quad (7)$$

where c is the proportion of Lorentzian contribution to band broadening. The pseudo-Voigt function is used extensively throughout this thesis for measuring band widths and digitally resolving overlapped peaks.

A molecule may have several vibrational modes with different $E_{vibration}$ based on geometrical factors. A three-dimensional molecule having a non-linear configuration with N atoms will have 3N – 6 vibrational modes. For example, the phosphate ion (PO_4^{3-}) forms a tetrahedron with five atoms having 3*(5) – 6 = 9 vibrations. These vibrations have degeneracy, meaning that the molecule can vibrate in several directions with identical shape distortion. Degenerate vibrations have equal energies and are essentially indistinguishable. The vibrations for phosphate in the gas phase are ν_1 (singly degenerate), ν_2 (doubly degenerate), ν_3 (triply degenerate), and ν_4 (triply degenerate).[13] The intensity of Raman bands depends on the symmetry of the vibration, with higher orders of symmetry having more intense bands. An illustration of the PO_4^{3-} stretches is shown in Figure 2.1B. The totally symmetric stretch ν_1 is much stronger than the other stretches.

For phosphate-containing solids the naming convention is the same; however, anisotropic distortions may cause a loss of degeneracy. This can be seen in the 550–650 cm^{-1} band envelope of apatites. The PO_4^{3-} ν_4 band is split into three poorly resolved bands. (see Figure 2.1D) Furthermore, band splitting arises in polymorphic solids in which several crystalline phases are formed, and in some crystalline material in which the

lattice contains multiple sites for a given molecule. This can be seen in some carbonated apatites (CAps) where CO_3^{2-} is substituted non-stoichiometrically. The increased lattice strain surrounding the CO_3^{2-} substitution sites creates an environment that is different than in the perfect lattice and can be distinguished spectroscopically. Stoichiometric apatite has a PO_4^{3-} ν_1 band at 961 cm^{-1}, whereas the B-type ν_1 band is at 957 cm^{-1}, and the A-type ν_1 band is a doublet at 947 cm^{-1} and 956 cm^{-1} (see Figure 2.1) The splitting of the PO_4^{3-} ν_1 band is most apparent in A-type CAp because of the high lattice strain induced from fitting CO_3^{2-} into the much smaller OH^- site. Multiple PO_4^{3-} ν_1 bands are not observed for B-type CAp because CO_3^{2-} and PO_4^{3-} have similar ionic volumes and substitution induces much less strain on the lattice. However, B-type distortion does induce spectroscopic changes, which will be discussed in Chapter 6.

Raman spectroscopy is a convenient technique for studying fresh tissue. Interference from water is almost undetectable because water has only asymmetric stretching modes. The Raman technique has been applied extensively to the study of calcified tissues for these reasons and because of the high intensity of the ν_1 band of the symmetrical PO_4^{3-} ion. The ν_1 band is most commonly used when signal-to-noise is an issue.

The most significant interference problem for Raman spectroscopy is fluorescence, which can be overwhelming in tissue. Protein fluorescence interference is lowest in the near-infrared part of the spectrum where few fluorophores emit. However, silicon-based detectors lose quantum efficiency in the near infrared beyond ~900 nm and do not respond to wavelengths much higher than 1050 nm. Therefore, common tissue Raman spectroscopy sources are 785 nm and 830 nm laser. For these lasers Raman shifts

below about 2000 cm^{-1} are easily within the wavelength region of silicon detector response. There is better detector quantum efficiency if a 785 nm laser is used, but lower fluorescence background if an 830 nm laser is used.

3 Instrumentation for Live Tissue Culture Microscopy

All Raman spectra in this thesis were acquired on one of two Raman systems. A description of the locally constructed 785 nm Raman microscope used in Chapters 5, 6, and 7 can be found in Ref [14]. Spectra of tissue cultures, described in Chapters 3 and 4, were acquired using a custom-built inverted Raman microscope built around a Nikon Eclipse microscope frame (Nikon Instruments, Melville, NY). The microscope has two channels for simultaneous Raman spectroscopy and fluorescence imaging. The Raman channel includes an 830 nm diode laser (Invictus, Kaiser Optical Systems, Inc., Ann Arbor, MI), a spectrograph (Holospec, Kaiser Optical Systems), and a back-illuminated deep-depletion CCD detector (iDus, Andor Technology, Belfast, UK). Optical components, listed in Figure 2.2, include beam-shaping optics (L1, L2, and L3) for line illumination, and a 200 mm focal length collection optic (L4), which is the standard tube lens focal length for Nikon infinity-corrected objectives. The laser line could be focused onto live tissue with any of several Nikon NIR-corrected objectives: 1x/0.04NA, 4x/0.14NA, 10x/0.5NA, 20x/0.45NA, 20x/0.75NA.

The fluorescence channel consisted of a mercury lamp excitation source, an EMCCD detector (iXon, Andor Technology, Belfast, UK) fitted with a 0.5x relay optic to maximize the amount of light per pixel, and a variety of filter cubes. Filter-cube optics are listed in Table 2.1. Bioluminescence imaging was performed with a hot-mirror to

separate the 830 nm light from the 565 nm peak emission of the *firefly luciferase* reporter. Further elimination of light was achieved with a 694 nm short pass filter (OD7 at 830nm). An external shutter S1 and beam block was placed in front of the laser for maximum separation of channels.

Tissue was maintained in a stage incubation chamber (LiveCell, Pathology Devices, Inc. Westminster, MD) at 5% CO_2, 100% humidity, and 37°C. Several tissue samples could be measured by using a digital stage (ProScan II, Prior Scientific, Rockland, MA) for precise movement of specimens. The microscope was automated in Labview using a com-port to communicate with the stage, a PCI card to communicate with the EMCCD camera, and USB to communicate with the CCD camera and external shutter. Outputs were image files saved in ASCII format. A more detailed description of the graphical user interface can be found in Appendix II.

Images were processed using custom Matlab scripts. Raman spectra were images having a spatial dimension (128 pixels) and a spectral dimension (1024 pixels). All spectra were corrected for optical aberations using IMTRANSFORM from the Image Processing toolbox. Input coordinates were based on the superposition of a neon spectrum and a bar target image. The spectral axis was calibrated in wavelength using a neon lamp with known atomic emission lines (NIST). Wavelength was converted to wavenumber by determining the excitation wavelength using the 732 cm^{-1} band in a spectrum of Teflon. Dark spectra were subtracted from all data spectra. A white-light spectrum was used to correct for the wavelength-dependent quantum efficiency of the CCD detector. Backgrounds were estimated using an iterative algorithm documented in Ref [15]. A script for calibrating and processing data can be found in Appendix III.

Spectral bands were fit to multiple pseudo-Voigt functions using a custom matlab script based on the Levenberg-Marquardt method described in Ref. [16].

Table 2.1 List of cube components: filters and dichroic mirrors.

Application	F3	M5	F4
Raman/luminescence	none	700nm hot mirror	694nm short pass
Alizarin Stain	FF01-543/22	FF562-Di03	FF01-593/40
White Light Imaging	none	50/50 mirror	none

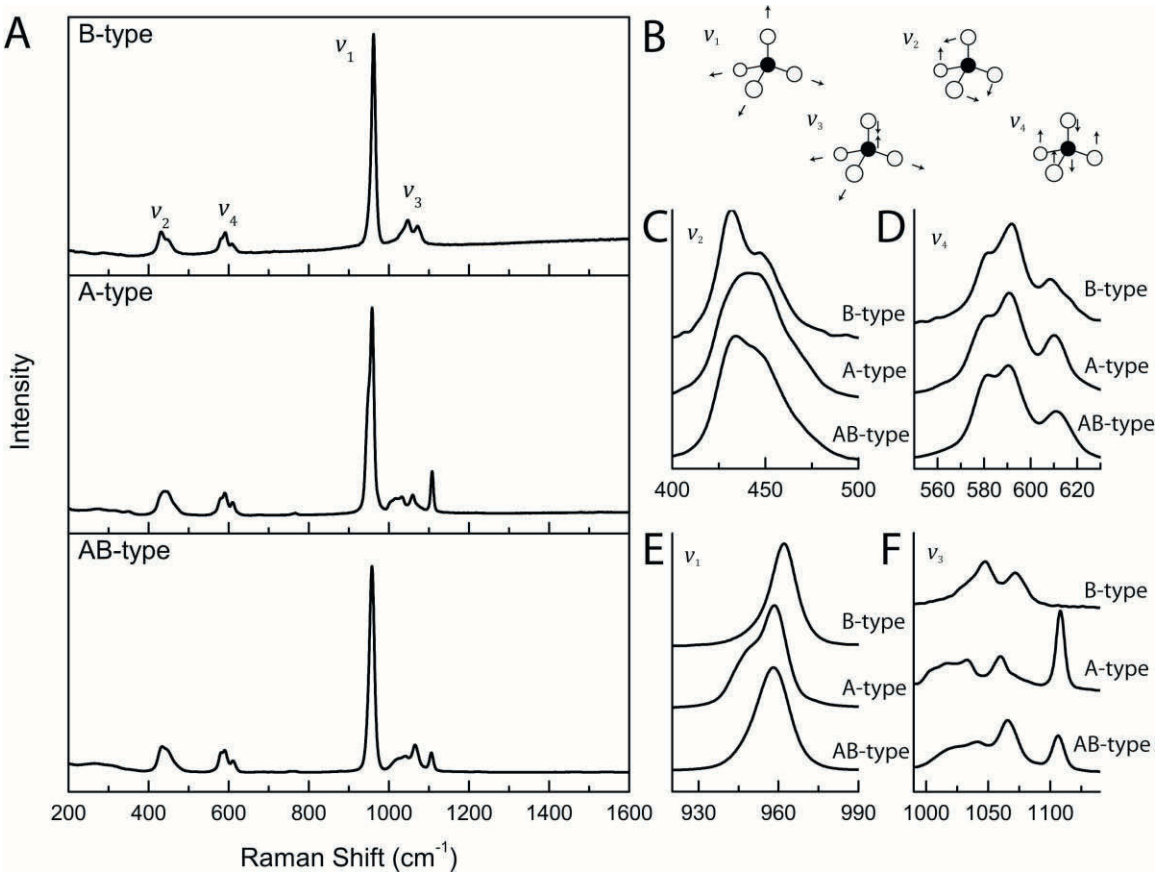

Figure 2.1 Interpretation of bands in Raman spectra of carbonated apatites. A) Spectra of apatites with different types of carbonate substitution, B) vibrational modes for tetrahedral molecule (i.e. PO_4^{3-}), C) v_2 region, D) v_4 region, E) v_1 region, F) v_3 region. Band assignments are from Ref [17].

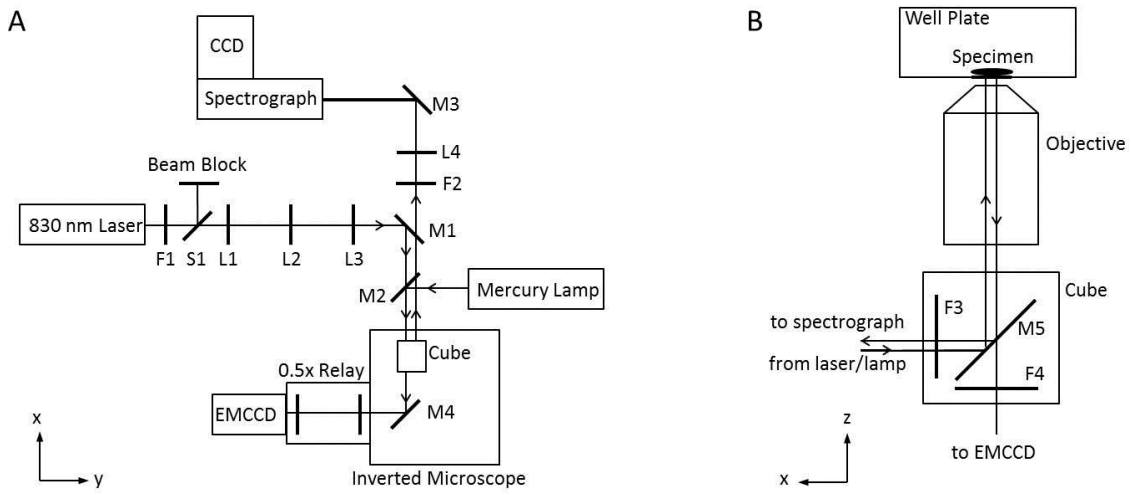

Figure 2.2 Schematic of custom microscope with Raman, fluorescence and bioluminescence channels. A) X-Y view of optical components. F1 is an 830nm laser clean-up filter, S1 is an external shutter, L1 is a fl=30mm achromat, L2 is a fl=50mm cylindrical singlet, L3 is a fl=100mm achromat, M1 is an 830 nm dichroic beam splitter, M2 is a 50/50 mirror, cube is a filter cube set, F2 is an 830nm long-bandpass filter, L4 is a 200mm tube lens, and M3 is an AR-coated mirror. B) X-Z view of the filter cube and objective. F3 is an excitation filter, M5 is a fluorescence dichroic beamsplitter, and F4 is an emission filter. Other components are as labeled.

References

1. Fowler BO, Moreno EC, Brown WE (1966) Infra-red spectra of hydroxyapatite, octacalcium phosphate and pyrolysed octacalcium phosphate. Arch Oral Biol 11:477-492

2. Brown WE, Chow LC (1976) Chemical properties of bone mineral. Annu. Rev. Mater. Sci. 6:213

3. Posner AS, Blumenthal NC, Boskey AL, Betts F (1975) Synthetic analogue of bone mineral formation. J Dent Res 54 Spec No B:B88-93

4. Roufosse AH, Aue WP, Roberts JE, Glimcher MJ, Griffin RG (1984) Investigation of the mineral phases of bone by solid-state phosphorus-31 magic angle sample spinning nuclear magnetic resonance. Biochemistry 23:6115-6120

5. Aue WP, Roufosse AH, Glimcher MJ, Griffin RG (1984) Solid-state phosphorus-31 nuclear magnetic resonance studies of synthetic solid phases of calcium phosphate: potential models of bone mineral. Biochemistry 23:6110-6114

6. Jaeger C, Groom NS, Bowe EA, Horner A, Davies ME, Murray RC, Duer MJ (2005) Investigation of the nature of the protein-mineral interface in bone by solid-state NMR. Chem. Mater. 17:3059-3061

7. Duer MJ, Friscic T, Proudfoot D, Reid DG, Schoppet M, Shanahan CM, Skepper JN, Wise ER (2008) Mineral surface in calcified plaque is like that of bone: further evidence for regulated mineralization. Arterioscler Thromb Vasc Biol 28:2030-2034

8. Duer MJ (2010) The molecular glue binding organic matrix and mineral crystals in biominerals: Basic amino acids may be as important as acidic ones A perspective on the role of basic amino acids in the molecular recognition of hydroxyapatite by statherin using solid state NMR, by M. Ndao, J.T. Ash, P. Stayton, G. Drobny. Surface Science 604:1237-1238

9. Schulmerich MV, Cole JH, Dooley KA, Morris MD, Kreider JM, Goldstein SA, Srinivasan S, Pogue BW (2008) Noninvasive Raman tomographic imaging of canine bone tissue. J Biomed Opt 13:020506

10. Svanberg S (ed) (2004) Atomic and Molecular Spectroscopy: Basic Aspects and Practical Applications. Springer-Verlag, Berlin

11. Levine IN (2000) Quantum Chemistry. Prentice-Hall, Inc., Upper Saddle River, NJ

12. Mukamel S (1995) Nonlinear optical Spectroscopy. Oxford University Press, New York

13. Coelho JM, Moreira JA, Almeida A, Monteiro FJ (2010) Synthesis and characterization of HAp nanorods from a cationic surfactant template method. J Mater Sci Mater Med 21:2543-2549

14. Kohn DH, Sahar ND, Wallace JM, Golcuk K, Morris MD (2009) Exercise alters mineral and matrix composition in the absence of adding new bone. Cells Tissues Organs 189:33-37

15. Lieber CA, Mahadevan-Jansen A (2003) Automated method for subtraction of fluorescence from biological Raman spectra. Appl Spectrosc 57:1363-1367

16. Press WH, Teukolsky SA, Vetterling WT, Flannery BP (1992) Numerical Recipes in C. Cambridge University Press, New York

17. Penel G, Leroy G, Rey C, Bres E (1998) MicroRaman Spectral Study of the PO4 and CO3 Vibrational Modes in Synthetic and Biological Apatites. Calcified Tissue International V63:475-481

CHAPTER III
TRACKING CIRCADIAN RHYTHMS OF BONE MINERAL DEPOSITION IN MURINE CALVARIAL TISSUE CULTURES

1 Introduction

Mammalian circadian rhythms are physiological phenomena occurring with daily periodicity, which are the result of negative feedback mechanisms. A circadian system functions in three parts, i) a timing cue, ii) a circadian oscillator, and iii) a rhythmic physiological response [1]. The master regulator for presumably all circadian rhythms in the body has been identified as the suprachiasmatic nucleus (SCN) located in the hypothalamus [2]. The SCN receives timing cues from retinal nerves sensitive to day/night light-level fluctuations and responds with rhythmic neural and humoral signaling to the body [3-5]. Circadian oscillators also reside in peripheral tissues that receive their timing cue from the SCN and respond by directing the rhythmic expression of genes. Mammalian circadian oscillators consist of a nuclear complex which is composed of three *Period* (*Per1*, *Per2* & *Per3*) and two *Cryptochrome* (*Cry1*, & *Cry2*) proteins whose expression is activated by the *Clock:Bmal* heterodimeric transcription factor [6]. The *Per*/*Cry* complex deactivates *Clock*:*Bmal* transcriptional activity halting

the production of *P*er and *Cry* proteins [7]. With the turnover of *Per*/*Cry*, the *Clock*:*Bmal* complex is reactivated and a new cycle starts [8].

Most peripheral tissues have been observed to exhibit circadian expression of *Per* and *Cry* genes including osteoblast cells [9], vertebral bone [10], craniofacial bone [11, 12] and skeletal muscle [13]. While the response to peripheral circadian oscillators has been implicated in several physiological functions of various tissues [14-18], the vastness of their influence is unknown. In peripheral tissues the *Clock*:*Bmal* transcribes a variety of downstream targets collectively termed clock-controlled genes (CCGs). CCGs that encode other transcription factors amplify the number of cycling genes and are able to influence other cells, tissues and extracellular processes [19]. Secondary negative feedback loops created by CCGs are capable of modifying the downstream circadian effect in phase and amplitude. Therefore, the circadian network has the potential to influence a physiological pathway at several points [20]. In bone tissue, the role of circadian oscillators has been implicated in bone turnover, cell functioning and fracture healing [21-23], but otherwise is a relatively new and little explored research topic. Making the connection to the circadian network may be integral to understanding the physiological process of ossification.

Bone mineralization is a protein-mediated process within tissue ossification where the mechanistic steps of calcium phosphate mineral formation are regulated by gene expression. Several proteins such as bone sialoprotein (BSP), dentin matrix protein 1 (DMP1), osteocalcin (OC) and osteonectin (ON) have been proposed to interact with the mineral directly through domains containing repeated acidic residues. Mechanistic function of these proteins has been described as either a nucleator or an inhibitor to

mineralization [24]. However, the mechanisms of bone mineralization are currently a hotly-debated topic [25], and as the intricacies of the mineralization process are coming forth a clearer understanding of protein function is being formed [26].

Modern analytical techniques for studying mineralization *in situ* are revealing more specific roles that these proteins may have. Nudelman et al. proposed that uptake of calcium phosphate clusters into the collagen fibril is regulated by tuning the electrostatics of the clusters with negatively charged protein segments [27]. These protein segments are then directed to binding sites within the gap regions where the calcium phosphate clusters nucleate into apatitic mineral. Furthermore, mineral formation has been argued to not deposit directly into the apatitic phase, but to pass through an intermediate solid phase stabilized by nucleating proteins before transitioning into apatitic mineral. Evidence for this intermediate phase suggests that it is either amorphous calcium phosphate [27] or octacalcium phosphate [28, 29]. Connecting these observed mineral phenomena to the expression of specific proteins remains an ongoing work.

We have hypothesized that bone mineralization may be linked in part to regulated protein expression by peripheral oscillators within the circadian network. Identifying a link between the two physiological processes may have clinical relevance as the search for more effective bone-forming pharmaceutical agents relies heavily on known mechanisms of ossification. The present study was designed to determine the time dependence of mineral activity by continuously monitoring mineral deposition in immortalized neonatal murine calvarial tissue using non-invasive Raman microscopy. Here we report evidence that supports the hypothesis that circadian rhythms are involved

in the mechanism of bone formation and are overt in mineral deposition in collagenous tissue.

2 Materials and Methods

2.1 Specimens

All procedures involving mice conformed to an Institutional Animal Care and Use Committee-approved protocol. Colonies of C57/Bl6 mice (Charles River, Wilmington, MA) and B6.BTBR-Tg(Per1-luc,Per1)1Jt/J mice (The Jackson Laboratory, Bar Harbor, Maine) were housed in University of Michigan animal facilities. Mice were subjected to a 12/12-hour light/dark cycle throughout gestation. Within 24 hours of birth, neonatal mice were collected and sacrificed. Calvaria including frontal, parietal and interparietal plates were harvested with brain and soft tissue removed. The fontanel region remained intact.

2.2 *Ex Vivo* Tissue Culture

During tissue preparation, calvaria were cultured with Dulbecco's Modified Eagle's Medium (DMEM) under standard growth conditions (5% CO_2, 37°C, 100% humidity). 6-well plates (In Vitro Scientific, Sunnyvale, CA) fitted with #1 glass windows in the bottom of each well were used throughout the experiment. Sapphire rounds (12 mm dia. 1 mm Th., Esco Products, Inc. Oak Ridge, NJ) were placed on top of the glass windows and calvaria were placed on the sapphire, brain-side up, with cuts made radially with a scalpel to allow the tissue to lose its dome shape. A 316 stainless-steel mesh screen and washer (Small Parts Inc., Seattle, WA) were placed on top of the calvaria for 4 hours until tissue remained flat, and then removed. Tissue was then stained with alizarin red (1 μg/ml) for 30 min and then washed in growth medium. A custom

tissue immobilizer device made with 316-stainless steel was used to anchor the calvaria at a single point inside a closed well plate (Figure 3.1). The growth medium was removed and differentiation medium containing DMEM, 100 μg/ml ascorbic acid phosphate, 10 mM β-glycerol phosphate, and 3 mM phosphate was used throughout the rest of the experiment. [30] The addition of differentiation medium marked time-zero for time-series experiments. Medium for Per1-luc/Per1 mouse calvaria was supplemented with 50 μg/ml luciferin for bioluminescence experiments.

The real-time polymerized chain reaction (RT-PCR) method was used to quantitate gene transcription in calvarial tissue. Calvaria were dissected and cultured ex vivo in osteogenic medium for 6 or 24 hours, then lysed in TriZol reagent to extract RNA. cDNA synthesis from the isolated RNA was performed with TaqMan Reverse Transcription Systems according to the manufacturer's instructions. Tissue mRNA levels of circadian clock genes were quantitated from six calvaria with the following TaqMan Gene Expression Assays (Applied Biosystems): Period1 (Mm00501813_m1), Period2 (Mm00478113_m1), Clock1 (Mm00455950), and Dbp (Mm01194021_m1). Expression of each gene was normalized to the endogenous control gene Gapdh (Mm99999915_g1) for each sample. Assays were performed on an ABI Prism 7700 sequence detector.

2.3 Raman Instrumentation

Mineral deposition in calvarial tissue was observed using a custom-built Raman inverted microscope. The Raman microscope consisted of a Nikon Ti inverted microscope with the tube lenses removed from the rear port. Collimated 830 nm laser light was directed through the rear port and focused on the specimen through an infinity-corrected 20x/0.45NA objective (Nikon). Raman scattered light was collected through the

rear port and focused through a 50 μm slit into a spectrograph (Holospec, Kaiser Optical Systems, Inc., Ann Arbor, MI) using a 200 mm achromatic tube lens and ultimately imaged using a back-illuminated deep-depletion CCD (Classic CCD, Andor Technologies, South Windsor, CT). Spectral resolution was 4–8 cm^{-1}. By digitally resolving spectral bands, differences in wavenumber shift of <1 cm^{-1} could be detected. Digital resolution of spectral bands in the 900–1010 cm^{-1} region was performed by band fitting the spectra to Gaussian + Lorentzian functions using the non-linear least-squares technique described in Ref [31] and implemented in Ref [32].

Well-plates containing calvaria and medium were maintained under standard culture conditions throughout the experiment using a stage incubation chamber (LiveCell, Pathology Devices, Inc. Westminster, MD). The microscope was fitted with a digital x-y-z stage with <1 μm spatial resolution capable of receiving digital motion commands and patterns. Raman spectra were taken simultaneously on no more than 4 calvaria for 120–140 hours by moving between the calvaria with a 1 hour duty cycle.

Calvaria were positioned such that the laser line illuminated the interparietal bone/fontanel interface perpendicular to the sagittal plane. Mineral deposition amount in bone collagen was measured using the phosphate ν_1 Raman band height at 957 cm^{-1} while using the phenylalanine band height at 1001 cm^{-1} as an internal measure of matrix components. Mineralization rates were determined by taking the Savitzky-Golay time derivative, of the mineral-to-matrix data. The crystalline phase of the mineral was measured using the phosphate ν_1 band position. Mineral having a band centered at 957–960 cm^{-1} was considered to be apatitic. Crystallinity, a combined measure of crystal size and perfection, was measured using the inverse of the phosphate ν_1 band width.

Crystallinity is measured with units of “nm” corresponding to crystal domain size; however, because of lattice substitutions distorting the structure, this measure is best interpreted as a lower limit to domain size and actual crystal size may be much larger.

2.4 Bioluminescence Imaging

Imaging of *Luc* gene coexpression was achieved using a 512x512 pixel EMCCD (iXon, Andor Technologies, Windsor, CT) binned with a 16x16 pixel region and fitted with a 0.5 magnification relay optic (Optec) attached to the side port on the inverted microscope. For single-channel detection, tissue was imaged using a 1x0.04NA objective (Nikon) with 60s acquisition times. Dual-channel detection was also employed using Raman as previously described, and EMCCD low-light imaging. In this configuration a 20x0.75NA objective (SuperFluor, Nikon) was used for all light collection. Bioluminescence images with 5 min acquisition times were taken immediately following Raman acquisitions at each time point. The laser was shuttered during light-sensitive measurements to ensure minimal interference. Fluorescence images of alizarin-stained calvaria were also performed with the same EMCCD channel with the addition of a mercury lamp excitation source and a filter cube (Semrock). Images were registered using a USAF bar target and the Raman illumination region was determined by imaging the laser spot on the tissue.

2.5 Change Point Analysis

Change point analysis (CPA) is a *post hoc* statistical technique used to segment sequential data into neighborhoods of contiguous data with similar features by estimating a change in distribution. This technique has been used extensively for industrial process monitoring [33], finance modeling [34], and genome sequencing applications. [35] Two

forms of CPA were applied to the data using the R programming language and website (cran.r-project.org). The cpt.mean algorithm from the CHANGEPOINT package is a non-parametric method that was used to calculate the optimal positioning and number of change-points based on maximum likelihood.[36] Change-points identified by this method are designated in figures by step-functions representing the mean of the data within each neighborhood. A second change point method was implemented using the BCP package, which uses a Markov Chain Monte Carlo method to estimate the probability of change at every time point.[37] Regions of time points with probability $p>50$ are designated with horizontal error-bars in figures.

3 Results

Per1 circadian gene expression in tissue culture was followed by measuring luminescence (in counts) from the *Luc* reporter protein. Images of the *Per1*:*Luc*/*Per1* calvarial tissue showed non-uniform distributions of *Per1* expression with heightened expression occurring in the anterior and posterior fontanel regions and along the posterior edge of the interparietal bone. Time series data of the integrated signal, seen in Figure 3.2G, showed periodic expression of *Per1* in both calvaria and brain. Oscillatory expressions in calvaria were characterized as having a period of 28.3±3.6 hours with initial peak expression at 13:48. *Per1* expression in brain tissue had a period of 27.0±9.0 hours with initial peak expression at 07:12. Based on the initial time-points, *Per1* peak expression levels in calvaria lagged behind those in brain by 6 hours in the cycle. Real-time PCR measurements of mRNA content for clock genes *Per1*, *Per2*, *Clock*, and *D-site*

binding protein (DBP) also fluctuated significantly over the first 24 hours of culture (Figure 3.3).

Bone mineralization was reproduced in an *ex vivo* tissue culture set-up which allowed for observation of active mineralization in calvaria through the course of a week. Mineralization activity in the tissue was initially verified by culturing calvaria for 0, 2, 4, 6, and 8 days followed by staining with alizarin red and imaging the fontanel region. Analysis of the calvarial images in Figure 3.2A–E showed that the integrated area of the posterior fontanel decreased continually over eight days (summarized in Figure 3.2F). There was no mineral detected within the fontanel region to suggest general deposition in the tissue. However, mineral deposition appeared to be confined to the fontanel perimeter, which was observed as an inward moving bone edge in time. Therefore, a progressive mineral front along the interparietal and parietal bone edges was responsible for the diminishing fontanel region.

Active mineral deposition in neonatal murine calvarial tissue culture was successfully observed non-destructively by Raman microscopy. The Raman probe was positioned near the interparietal bone/fontanel boundary on the unmineralized fontanel side and repeated measurements were taken at 1-hour intervals for up to 6 days. In a sample size of ten neonatal murine calvaria, six displayed Raman characteristics consistent with tissue mineralization showing a significant increase in mineral phosphate Raman signal (957 cm^{-1}) through the course of the experiment. The amino acid residues phenylalanine (Phe, 1001 cm^{-1}), proline (Pro, 850 & 925 cm^{-1}) and hydroxyproline (Hyp, 875 & 940 cm^{-1}), which are associated with the organic matrix, showed little variation and no significant change in intensity throughout the experiment. The ratio of mineral

phosphate intensity to Phe intensity, referred to here as the mineral-to-matrix ratio, showed dramatic increases signifying active deposition of mineral into the tissue.

The influence of circadian timing was evident in mineral formation rate kinetics. Mineral acquisition in the calvarial tissue proceeded in bursts of rapid deposition followed by intervals of low deposition or no deposition, which were observed in each of the actively mineralizing calvaria. This appeared as a stair-step increase of the mineral-to-matrix ratio in time (Figure 3.4C). Mineralization rate, presumed to be a function of nucleating protein expression, was determined by taking the time-derivative (see Figure 3.4A). Fluctuating mineralization can be seen in Figure 3.4C as peaks and troughs. Calvaria displayed a number of peaks ranging from two to six peaks within the 6-day period. The mineralization event initially peaked at 18:00, which was the lights-off time during gestation (Figure 3.4B). Peak-to-peak time intervals averaged from all mineralizing calvaria (n=6) gave a period of 26.8 hours with a standard deviation of 9.6 hours.

Statistical analysis of the raw kinetic data was necessary to establish an unbiased measure of periodicity in the mineralization process. CPA was used to identify time points at which the mineral content was most likely to have changed in the tissue. Change points are indicated in the mineral-to-matrix kinetic data shown in Figure 3.4C as downward arrows with horizontal bars indicating probabilities $p>0.5$. For a more complete depiction of mineral kinetics across all mineralizing calvaria see Figure 3.7A–F. CPA results gave an average period of 29.0 hours with a standard deviation of 10.4 hours. Although this analysis estimated a longer period to mineralization than that

predicted by peak-to-peak rates, the two methods do not provide statistically disparate results by a two-tailed T-test ($p=0.34$).

Dual-channel detection of Raman and bioluminescence facilitated the simultaneous detection of mineral deposition and *Per1* expression dynamics for a direct comparison of phase. Figure 3.5, shows a combined plot of the two channels measured on the same calvarium. The mineral showed periodic behavior with maximum mineral deposition occurring every 27.2 hours with the first pronounced mineralization peak occurring at 21:21. *Per1* expression had a periodicity of 24.1 hours with the first peak at 11:45. Mineral appears to be almost 10 hours behind local *Per1* expression in the circadian cycle.

The first mineral detected along the interparietal bone edge was characterized as small apatitic crystallites. In the first hours of observation the mineral phosphate was measured as having a Raman band centered at 957 cm^{-1} (see Figure 3.6A) which is consistent with previous Raman studies on young bone but contrasts more mature bone mineral which typically has a band centered at 959 cm^{-1}. The band center remained constant as mineral accumulated in the tissue. Crystallinity of deposited apatite had an initial measure of 14±2.5 nm averaged across calvaria. Linear growth of the mineral occurred in each of the tissues at an average rate of 0.068±0.021 nm/h. However, in some of the faster growing tissue a maximum crystallinity threshold was achieved after which no more growth was observed. Figure 3.6B shows mineral growth in a calvarium where linear growth was experienced only in the first 2.5 days after which the maximum crystallinity of 23 nm was reached but never exceeded. Similar size thresholds were repeatedly observed across calvaria (see Figure 3.8A–F). Average crystallinity of calvaria

in their most advanced mineralization state was 21.7±2.6 nm. These results seem to suggest that there is a limit to crystallinity achievable by this tissue system.

4 Discussion

We report direct evidence for circadian oscillator involvement in mammalian bone mineralization. Neonatal murine calvarial *ex vivo* tissue cultures provided an adequate model for *in situ* mineralization and facilitated the tracking of mineralization kinetics. Cyclic events were observed as pulses of heightened mineralization lasting about 5 hours occurring periodically with an average interval of 29.0 hours. Mineral acquisition in the tissue proceeds in a stair-step fashion with periodic increases in mineral content. Furthermore, mineralization appears to be mediated by an oscillatory mechanism generated locally in the calvarial tissue. Functioning circadian mechanisms in *ex vivo* tissue cultures have been sustained previously up to 30 days in SCN tissue and up to 7 days in lung, liver and skeletal muscle tissues.[13] In this study, cultured calvarial tissue displayed continued rhythmicity for up to 6 cycles. Although circadian rhythms have been implicated in the bone formation pathway through fluctuating biomarkers and byproducts, periodic behavior in the biosynthesis of bone structural components has not been measured. This is the first direct evidence for circadian rhythms in bone acquisition.

Timed expression of *Per1* in the calvarial tissue was consistent with the molecular clock model proposed by Relogio *et al.* who predicted maximum *Per1* expression at circadian time 12:30.[38] According to this model, *Cry* is expressed jointly with the *Per* genes having maximum expression at 12:00. The *Bmal:Clock* transcription complex is inhibited by *Per/Cry* expression and therefore reaches a maximum at 21:00 when *Per/Cry*

levels are low. Maximum mineral deposition observed in this study occurred near 21:00, which suggests that the expression of mineralizing proteins is closely associated with, if not directly transcribed by the *Bmal:Clock* transcriptional factor.

First signs of mineral in the fontanel at the interparietal bone edge were that of small apatitic crystals which increased in crystallinity over several days. Mineral growth proceeded in a linear fashion unperturbed by periodic acquisition of new mineral. Intermediate crystal phases such as amorphous calcium phosphate or octacalcium phosphate which have been observed in more controlled systems [27, 39] were not observed. However, detection limits prohibited characterization of the mineral in its earliest form. Gorski described the mineralization process as having two parts: 1) the nucleation phase where crystallites of 15–20 nm sizes are deposited into the ECM and 2) the growth phase where individual crystals propagate in size [26, 40]. The first detected mineral in this study had a crystallinity of 14 nm; however, after several days the mineral increased in size to a crystallinity of 21.7 nm. The propagation stage was observed as a linear increase in crystallinity with no appearance of periodic behavior. Within the scope of these experiments it appears that the nucleation process is linked to circadian oscillatory signaling, but the propagation of crystal size is not. Furthermore, no specimen achieved a crystallinity value above 23 nm during the week-long measurement time. Calvaria which displayed immediate mineralization reached this size within 3 days; however, crystal propagation stopped at this point (Figure 3.6B).

Bone mineral has a high uniformity of crystallinity within a given tissue type [41], although it is currently not clear what constrains crystallinity in bone formation. There is no agreed mechanism for stopping crystal growth at a certain size, although possibilities

include the timed expression of crystal growth inhibitors [24] or the limited space in type I collagen gap regions [42]. The authors propose a third possibility that crystal growth is inhibited by internal crystal composition. Carbonate substitution in the apatitic crystal has a destabilizing effect that prohibits crystals above a certain size (see Chapter 6). Therefore, regulation of mineral crystallinity might occur by influencing carbonate ion levels in mineralizing tissues.

Although these results imply that any osteoblast-directed ossification can be influenced by circadian rhythms, we have no evidence about whether circadian rhythms in mineralization are preserved in endochondral ossification of long bones or in fracture healing. Genetic defects which perturb the amount and quality of the mineral, such as in osteogenesis imperfecta [43] and osteopetrosis [44], may also cause deviations in circadian mineralization. Furthermore, therapeutic interventions for bone formation may disrupt the circadian action of mineralization. Catabolic treatment with bisphosphonates reduces the daily resorption of bone, but shows no sign of perturbing the circadian pattern and has no effect on bone formation markers in either magnitude or frequency.[45] However, anabolic treatments which target osteoblast activity are more likely to disrupt circadian rhythms in osteogenesis. Recently, Luchavova et al. showed that once-daily injections of the teriparatide PTH(1-34) induced twice-daily peaks in bone-turnover markers.[46] A less frequent dose is required for treatment with sclerostin antibody; however its effect on circadian mineralization has not been determined.

In summary, this study provides further details of the mechanisms of bone formation including evidence for oscillatory behavior of collagen mineralization. Based on the current evidence we see no other explanation for periodic behavior in these

calvarial explants than the intervention of a local circadian mechanism in intramembranous ossification, particularly in the nucleation of apatitic mineral. It is not clear at this point whether circadian signaling also plays a role in mineral propagation and crystallinity, however, the data here suggest no influence.

Acknowledgments

This work was done in collaboration with Guisheng Zhao and Renny Franceschi who oversaw the maintenance of all mouse colonies and tissue cultures used in this study. Guisheng Zhao contributed RT-PCR data for this thesis. Christopher Wilson provided technical assistance and consultation on fluorescence microscopy and handling tissue.

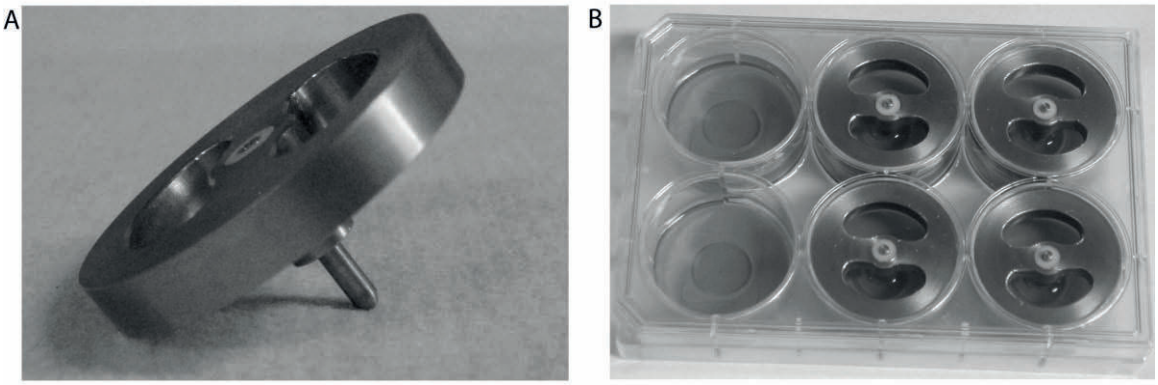

Figure 3.1 Immobilization of calvaria. A) Tissue immobilizing device made with 316 stainless steel used to hold calvaria by a single point in the well plate. B) 6-well plate with glass windows fitted with four immobilizing devices.

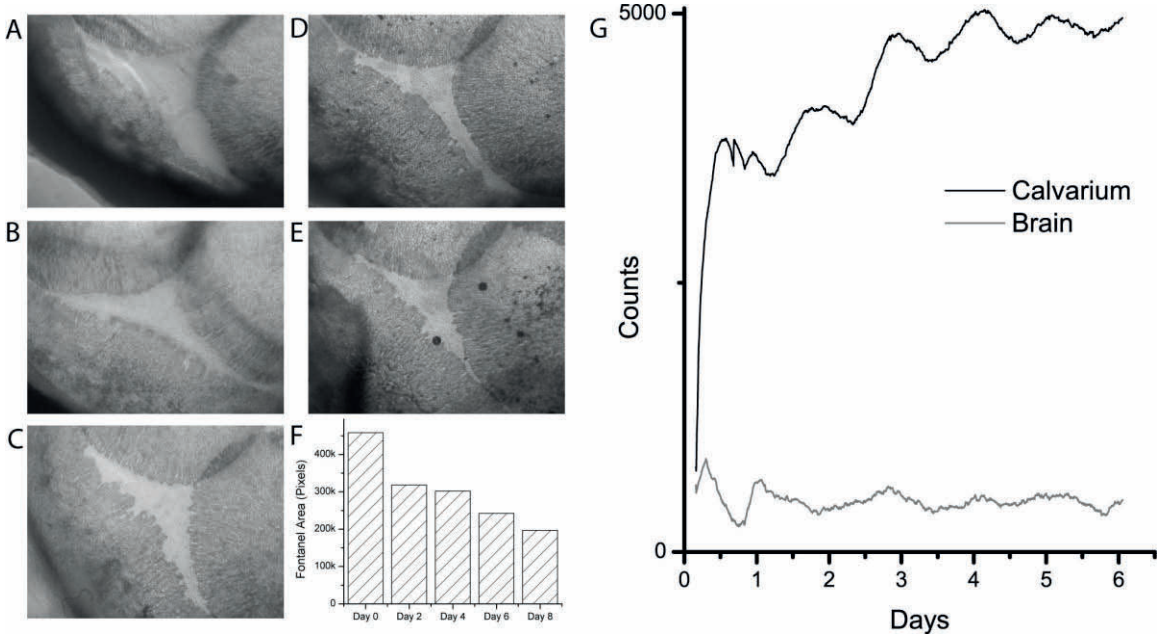

Figure 3.2 Closure of fontanel and *Per1* expression in murine calvaria. Images of neonatal calvarial tissue cultures with alizarin red stain showing interparietal and parietal bones and fontanel after A) 0, B) 2, C) 4, D) 6, and E) 8 days of culture. Bar chart (F) shows quantitative results of fontanel area measured in image pixels over 8 days. G) Plot of *Per1* expression in a calvarium and brain over 6 days.

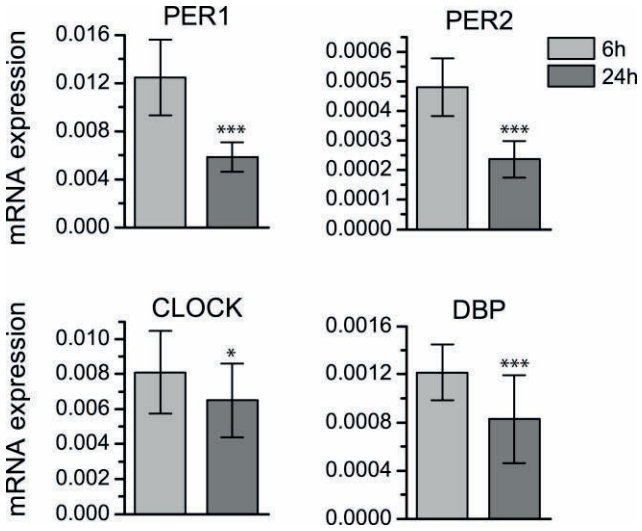

Figure 3.3 Real-time PCR measurements of *Per1*, *Per2*, *Clock* and *D-site binding protein* (DBP). Comparison of 6 and 24 hour circadian oscillator component levels in calvarial tissue cultures. $^{*}p < 0.05, ^{***}p < 0.001$ for comparison of time points. Data was acquired by Guisheng Zhao.

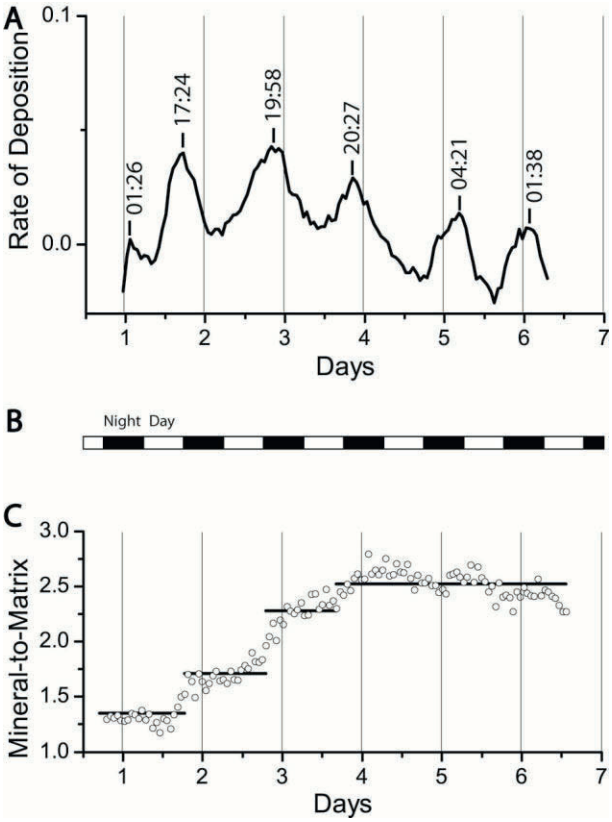

Figure 3.4 Periodic mineral deposition at the interparietal bone/fontanel boundary. Plot of (A) deposition rate as a function of time in cultured calvarial tissue measured by taking the time derivative of mineral content, (B) Lights-on/lights-off schedule defining "Zeitgeiber" time, and (C) mineral deposition in time as measured by the PO_4^{3-} : Phe ratio.

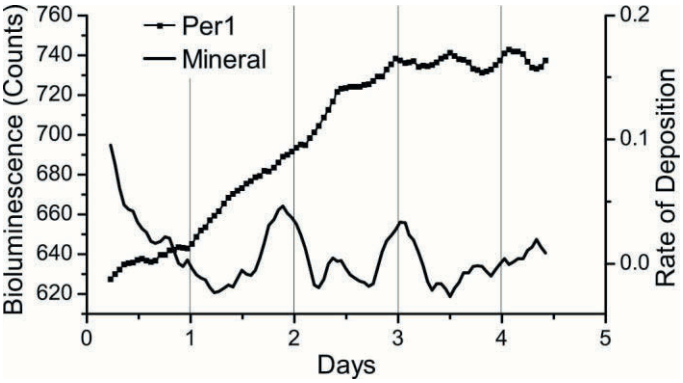

Figure 3.5 Simultaneous detection of *Per1* expression dynamics and mineral deposition in calvarial tissue. Bioluminescence, plotted as squares, is a measure of *Per1* expression. Raman measure of mineral deposition in calvarial tissue plotted as a time derivative (bold line).

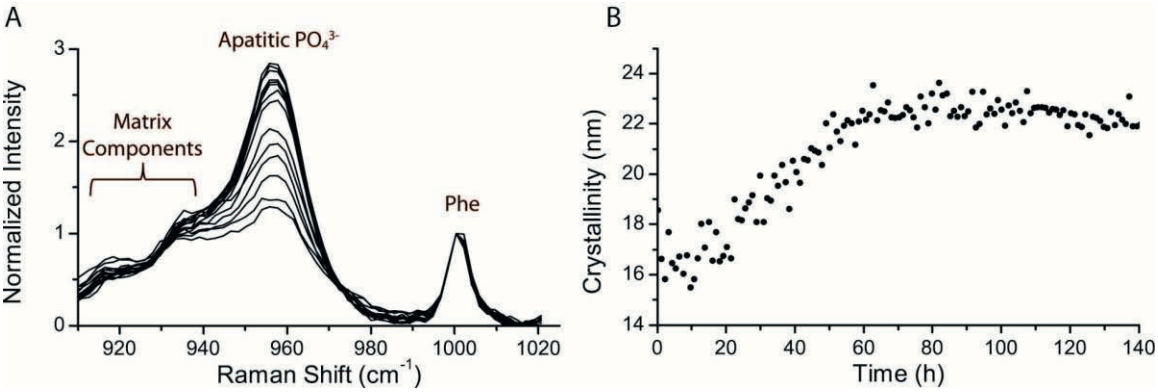

Figure 3.6 Native mineral nucleation and growth kinetics. A) Overlay of Raman spectra of calvarial tissue at the interparietal bone/fontanel boundary. Spectra show evolution of the apatitic PO_4^{3-} band with 10-hour time intervals. B) Plot of mineral crystallinity growth in time in neonatal calvaria with 1-hour time resolution.

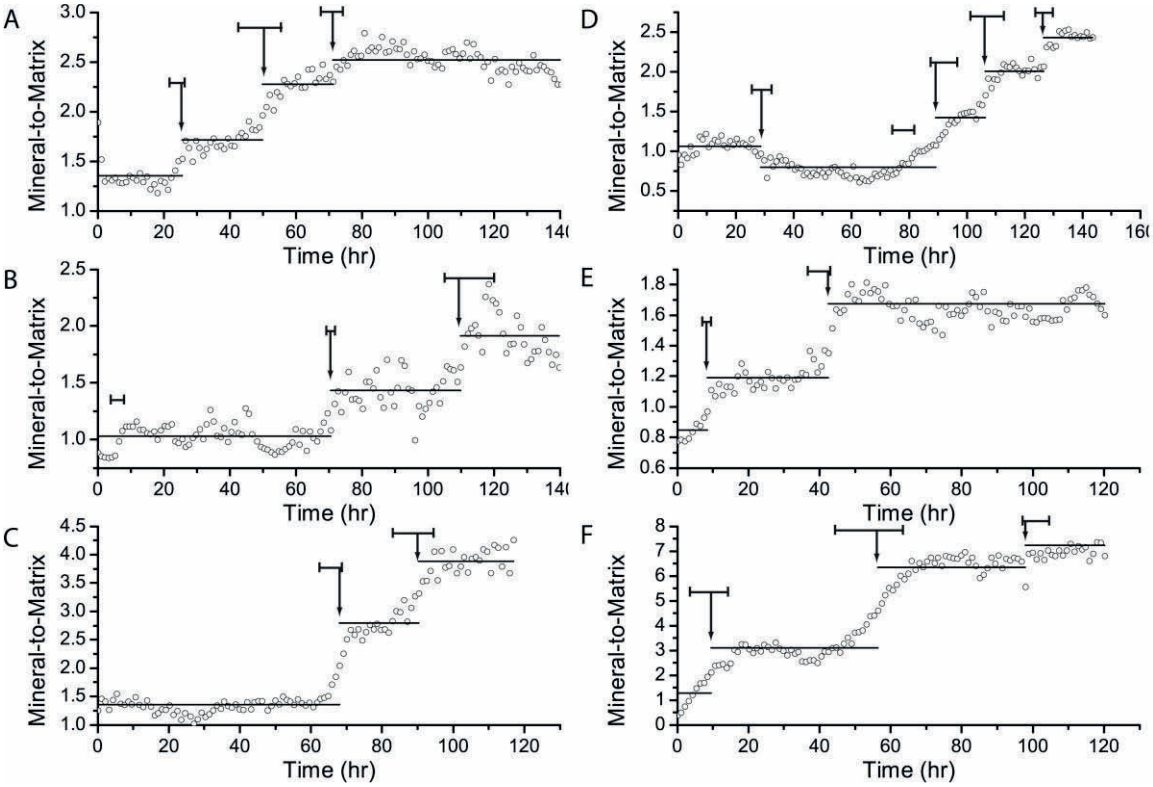

Figure 3.7 Mineralization plots of in six neonatal murine calvaria at the interparietal bone/fontanel boundary. Accumulation of mineral relative to organic matrix in six identically treated neonatal murine calvaria. Results from CPA analysis are indicated as arrows for change points, and horizontal bars for confidence intervals. Horizontal lines indicate average value between change points.

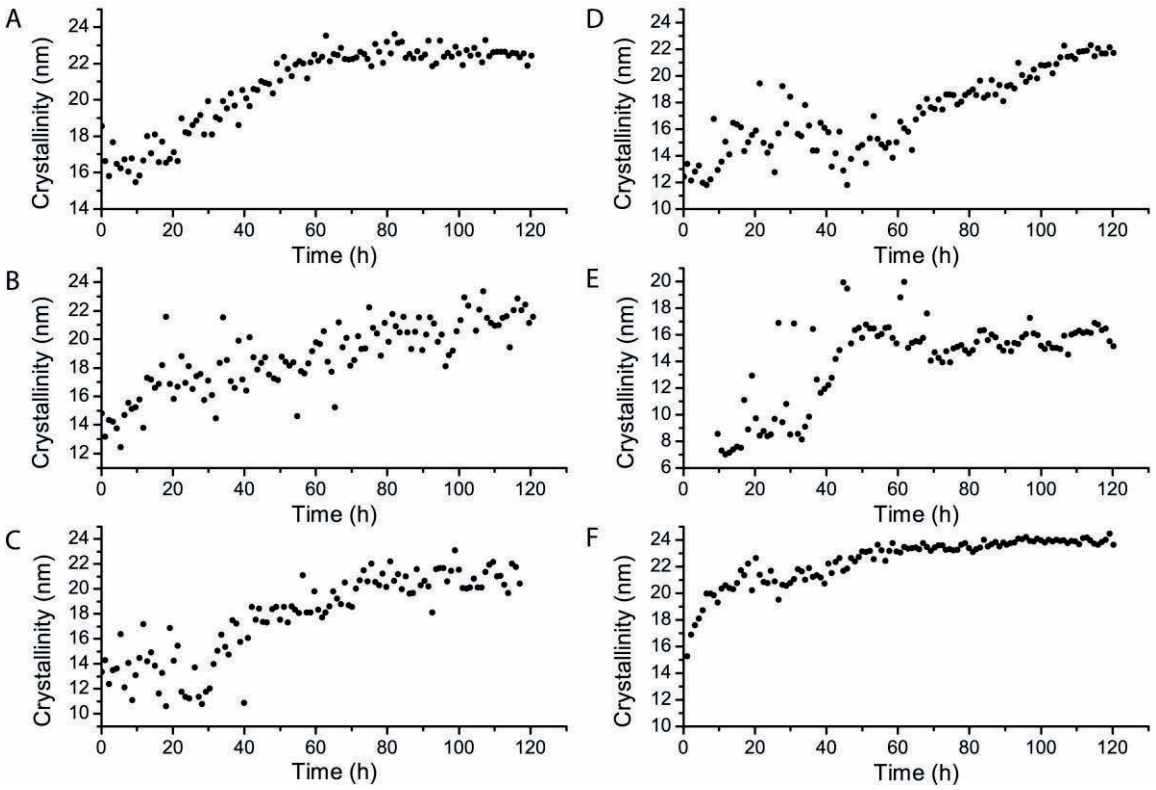

Figure 3.8 Crystallinity values of mineral deposited in time in six neonatal murine calvaria at the interparietal bone/fontanel boundary.

References

1. Kwon I, Choe HK, Son GH, Kim K (2011) Mammalian molecular clocks. Exp Neurobiol 20:18-28

2. Reppert SM, Weaver DR (2002) Coordination of circadian timing in mammals. Nature 418:935-941

3. Balsalobre A, Brown SA, Marcacci L, Tronche F, Kellendonk C, Reichardt HM, Schutz G, Schibler U (2000) Resetting of circadian time in peripheral tissues by glucocorticoid signaling. Science 289:2344-2347

4. Maywood ES, O'Neill JS, Chesham JE, Hastings MH (2007) Minireview: The circadian clockwork of the suprachiasmatic nuclei--analysis of a cellular oscillator that drives endocrine rhythms. Endocrinology 148:5624-5634

5. Schibler U, Sassone-Corsi P (2002) A web of circadian pacemakers. Cell 111:919-922

6. Lee C, Etchegaray JP, Cagampang FR, Loudon AS, Reppert SM (2001) Posttranslational mechanisms regulate the mammalian circadian clock. Cell 107:855-867

7. Kume K, Zylka MJ, Sriram S, Shearman LP, Weaver DR, Jin X, Maywood ES, Hastings MH, Reppert SM (1999) mCRY1 and mCRY2 are essential components of the negative limb of the circadian clock feedback loop. Cell 98:193-205

8. Duong HA, Robles MS, Knutti D, Weitz CJ (2011) A molecular mechanism for circadian clock negative feedback. Science 332:1436-1439

9. Fu L, Patel MS, Bradley A, Wagner EF, Karsenty G (2005) The molecular clock mediates leptin-regulated bone formation. Cell 122:803-815

10. Maronde E, Schilling AF, Seitz S, Schinke T, Schmutz I, van der Horst G, Amling M, Albrecht U (2010) The clock genes Period 2 and Cryptochrome 2 differentially balance bone formation. PLOS One 5:e11527

11. Zvonic S, Ptitsyn AA, Kilroy G, Wu X, Conrad SA, Scott LK, Guilak F, Pelled G, Gazit D, Gimble JM (2007) Circadian oscillation of gene expression in murine calvarial bone. J Bone Miner Res 22:357-365

12. Gafni Y, Ptitsyn AA, Zilberman Y, Pelled G, Gimble JM, Gazit D (2009) Circadian rhythm of osteocalcin in the maxillomandibular complex. J Dent Res 88:45-50

13. Yamazaki S, Numano R, Abe M, Hida A, Takahashi R, Ueda M, Block GD, Sakaki Y, Menaker M, Tei H (2000) Resetting central and peripheral circadian oscillators in transgenic rats. Science 288:682-685

14. Lamia KA, Storch KF, Weitz CJ (2008) Physiological significance of a peripheral tissue circadian clock. Proc Natl Acad Sci U S A 105:15172-15177

15. Storch KF, Paz C, Signorovitch J, Raviola E, Pawlyk B, Li T, Weitz CJ (2007) Intrinsic circadian clock of the mammalian retina: importance for retinal processing of visual information. Cell 130:730-741

16. Zvonic S, Ptitsyn AA, Conrad SA, Scott LK, Floyd ZE, Kilroy G, Wu X, Goh BC, Mynatt RL, Gimble JM (2006) Characterization of peripheral circadian clocks in adipose tissues. Diabetes 55:962-970

17. Duffield GE, Best JD, Meurers BH, Bittner A, Loros JJ, Dunlap JC (2002) Circadian programs of transcriptional activation, signaling, and protein turnover revealed by microarray analysis of mammalian cells. Curr Biol 12:551-557

18. Balsalobre A, Damiola F, Schibler U (1998) A serum shock induces circadian gene expression in mammalian tissue culture cells. Cell 93:929-937

19. Edery I (2011) A master CLOCK hard at work brings rhythm to the transcriptome. Genes Dev 25:2321-2326

20. Zhang EE, Kay SA (2010) Clocks not winding down: unravelling circadian networks. Nat Rev Mol Cell Biol 11:764-776

21. Mengatto CM, Mussano F, Honda Y, Colwell CS, Nishimura I (2011) Circadian rhythm and cartilage extracellular matrix genes in osseointegration: a genome-wide screening of implant failure by vitamin D deficiency. PLOS One 6:e15848

22. Hanyu R, Hayata T, Nagao M, Saita Y, Hemmi H, Notomi T, Nakamoto T, Schipani E, Knonenbery H, Kaneko K, Kurosawa H, Ezura Y, Noda M (2011) Per-1 is a specific clock gene regulated by parathyroid hormone (PTH) signaling in osteoblasts and is functional for the transcriptional events induced by PTH. J Cell Biochem 112:433-438

23. Gundberg CM, Markowitz ME, Mizruchi M, Rosen JF (1985) Osteocalcin in human serum: a circadian rhythm. J Clin Endocrinol Metab 60:736-739

24. Hunter GK, Hauschka PV, Poole AR, Rosenberg LC, Goldberg HA (1996) Nucleation and inhibition of hydroxyapatite formation by mineralized tissue proteins. Biochem J 317 (Pt 1):59-64

25. Colfen H (2010) Biomineralization: A crystal-clear view. Nat Mater 9:960-961

26. Gorski JP (2012) Biomineralization of bone: a fresh view of the roles of non-collagenous proteins. Front Biosci 17:2598-2621

27. Nudelman F, Pieterse K, George A, Bomans PHH, Friedrich H, Brylka LJ, Hilbers PAJ, With Gd, Sommerdijk NAJM (2010) The role of collagen in bone apatite

formation in the presence of hydroxyapatite nucleation inhibitors. Nature Materials 9:1004-1009

28. Crane NJ, Popescu V, Morris MD, Steenhuis P, Ignelzi JMA (2006) Raman spectroscopic evidence for octacalcium phosphate and other transient mineral species deposited during intramembranous mineralization. Bone 39:434-442

29. Weiner S (2006) Transient precursor strategy in mineral formation of bone. Bone 39:431-433

30. Wang D, Christensen K, Chawla K, Xiao G, Krebsbach PH, Franceschi RT (1999) Isolation and characterization of MC3T3-E1 preosteoblast subclones with distinct in vitro and in vivo differentiation/mineralization potential. J Bone Miner Res 14:893-903

31. Press WH, Teukolsky SA, Vetterling WT, Flannery BP (1992) Numerical Recipes in C. Cambridge University Press, New York

32. McElderry J-DP, Kole MR, Morris MD (2011) Repeated freeze-thawing of bone tissue affects Raman bone quality measurements. J Biomed Optics 16:071407

33. Lai TL (1995) Sequential changepoint detection in quality control and dynamical systems. J Roy Stat Soc B Met 57:613-658

34. Bai J, Perron P (2003) Computation and analysis of multiple structural change models. J Appl Econ 18:1-22

35. Snijders AM, Nowak N, Segraves R, Blackwood S, Brown N, Conroy J, Hamilton G, Hindle AK, Huey B, Kimura K, Law S, Myambo K, Palmer J, Ylstra B, yue JP, Gray JW, Jain AN, Pinkel D, Albertson DG (2001) Assembly of microarrays for genome-wide measurement of DNA copy number. Nat Genet 29:263-264

36. Auger IE, Lawrence CE (1989) Algorithms for the optimal identification of segment neighborhoods. B Math Stat 51:39-54

37. Erdman C, Emerson JW (2007) An R package for performing a Bayesian analysis of change point problems. J Stat Softw 23

38. Relogio A, Westermark PO, Wallach T, Schellenberg K, Kramer A, Herzel H (2011) Tuning the mammalian circadian clock: robust synergy of two loops. PLoS Comput Biol 7:e1002309

39. Kazanci M, Fratzl P, Klaushofer K, Paschalis EP (2006) Complementary Information on In Vitro Conversion of Amorphous (Precursor) Calcium Phosphate to Hydroxyapatite from Raman Microspectroscopy and Wide-Angle X-Ray Scattering. Calcified Tissue International V79:354-359

40. Gorski JP (1998) Is all bone the same? Distinctive distributions and properties of non-collagenous matrix proteins in lamellar vs. woven bone imply the existence of different underlying osteogenic mechanisms. Crit Rev Oral Biol Med 9:201-223

41. Donnelly E, Meredith DS, Nguyen JT, Boskey AL (2011) Bone tissue composition varies across anatomic sites in the proximal femur and the iliac crest. J Orthop Res

42. Bonucci E (2012) Bone mineralization. Front Biosci 17:100-128

43. Camacho NP, Hou L, Toledano TR, Ilg WA, Brayton CF, Raggio CL, Root L, Boskey AL (1999) The material basis for reduced mechanical properties in oim mice bones. J Bone Miner Res 14:264-272

44. Wojtowicz A, Dziedzic-Goclawska A, Kaminski A, Stachowicz W, Wojtowicz K, Marks SC, Jr., Yamauchi M (1997) Alteration of mineral crystallinity and collagen cross-linking of bones in osteopetrotic toothless (tl/tl) rats and their improvement after treatment with colony stimulating factor-1. Bone 20:127-132

45. Shao P, Ohtsuka-Isoya M, Shinoda H (2003) Circadian rhythms in serum bone markers and their relation to the effect of etidronate in rats. Chronobiol Int 20:325-336

46. Luchavova M, Zikan V, Michalska D, Raska I, Jr., Kubena AA, Stepan JJ (2011) The effect of timing of teriparatide treatment on the circadian rhythm of bone turnover in postmenopausal osteoporosis. Eur J Endocrinol 164:643-648

CHAPTER IV
BONE SIALOPROTEIN MEDIATION OF APATITE NUCLEATION IN MURINE CALVARIAL TISSUE CULTURE

1 Introduction

The importance of the phosphoprotein, bone sialoprotein (BSP), to the mineralization process in bone formation is not disputed. BSP is expressed almost exclusively in bone by preosteoblasts, osteoblasts, and osteocytes.[1, 2] During embryonic development, maximal expression of BSP mRNA coincides with the first signs of mineralization in connective tissue. [3] Bones from BSP null mice are significantly undermineralized during fetal development and young adulthood, but develop fully mineralized bones in adulthood.[4] Hunter and Goldberg identified BSP as a nucleator of hydroxyapatite showing that the mineral formed in a steady-state agarose gel system.[5] Nucleative properties have been attributed to two domains of repeated glutamic acid residues and several phosphorylated serine residues in the primary protein sequence.[6, 7] These residues are capable of forming a template for Ca^{2+} binding. Bound Ca^{2+} attracts PO_4^{3-} in solution forming Ca-PO_4 networks that are able to overcome the nucleation energy barrier.

Reports of BSP-mediated mineralization *in vitro* have shown that the precipitate is apatitic, consistent with bone mineral, [8] suggesting that the BSP template nucleates apatite directly. However, *in vivo* mineralization may form alternate mineral phases in addition to apatite. Molecular dynamic simulations show that BSP is capable of stabilizing either apatite or amorphous Ca-PO_4. Yang et al. showed that the acidic domain has two stable conformations. In the presence of apatite, the domain forms an alpha-helix that has regularly spaced acidic binding sites that can adhere to the crystal face. In calcium phosphate solution, the acidic domain preferentially forms a random coil with variably spaced binding sites that template an irregular Ca-PO_4 network.[9, 10] Biological factors may also affect the function of BSP. It has been shown that (Hunter and Goldberg Matrix Biology 2008) the nucleative properties of BSP are enhanced upon binding to collagen. [11] The binding site appears to be at the N-terminus of the collagen molecule within the gap-region. [12] Nudelman et al. proposed that acidic proteins change the electrostatic charge of Ca-PO_4 clusters facilitating entry into the collagen fibril where apatite is ultimately formed. [13] *In situ* mineralization studies have confirmed alternate forms of Ca-PO_4 mineral formation. Crane et al. showed that amorphous calcium phosphate and octacalcium phosphate are present in developing calvaria which were proposed to be nucleate precursors to apatite. [14] An amorphous $CaPO_4$ precursor phase to apatite formation has been shown previously in other organisms [15] and has been argued to be the mechanism of mammalian bone formation. [16, 17] However, this mineralization model is not widely accepted [18] and has been a "hotly debated" topic. [19] No mineralization mechanism has been agreed upon mainly because apatite precursors are difficult to measure and characterize due to their transient

nature. Kinetic measurements of *in situ* mineralization with sufficient time resolution are lacking on this issue.

The purpose of this chapter is to characterize mineral precipitates in connective tissue with sufficient temporal resolution to track the formation and dynamics of non-apatitic mineral species in time. We hypothesize that BSP nucleates according to a two-step mechanism where apatite is not nucleated directly. In this study we tracked mineral formation in cultured neonatal murine calvaria using Raman spectroscopy to characterize the mineral phase. An adenovirus transfection scheme was used to overexpress the BSP protein in calvaria, which effectively dominated mineral nucleation. We observed the formation of intermediate species in BSP-overexpressed calvaria that were not present in controls.

2 Materials and Methods

2.1 Tissue handling

All mice were handled in a similar fashion to the procedures described in Chapter 3. Pregnant mice were kept two weeks before full term in an IACUC approved facility with a 12/12-hour light/dark cycle. Twenty-four neonatal C57Bl6 mice were sacrificed within 24 hours of birth and immediately cultured in Dulbecco's Modified Eagle's Medium (DMEM) under standard growth conditions (5% CO_2, 37°C, 100% humidity). Glass-bottom 6-well plates fitted with 12 mm dia. 1 mm th. Sapphire round inserts were used to encase the culture system throughout the experiment. To keep calvaria flat and open a stainless steel washer and a wire mesh screen were placed on top of the tissue for 4 hours then removed. The tissue was then stained with (1 μg/ml) of alizarin red for 30

min and washed in growth medium. At this point calvaria were separated into three treatment groups: 1) No infection (control, n=7), 2) Adenovirus-LacZ (Ad-LacZ) infection (vehicle, n=8), Adenovirus-BSP (Ad-BSP) infection (n=9).

Infection parameters were determined in a separate set of calvaria by measuring BSP expression levels in tissue and medium by Western blot. Calvaria were minced and lysed in RIPA buffer (500mM NaCl, 20mM Tris, 1 mM EGTA, 0.25% NP40, pH 7.4 with Roche miniComplete protease inhibitor cocktail) and then homogenized by briefly sonicating on ice. Equal quantities of protein were separated on 4-20% Tris-Glycine polyacrylamide gels and electrophoretically transferred to nitrocellulose membranes. The membranes were blocked with 1% nonfat drymilk in Tris-Buffered Saline with Tween 20 (TBS-T) and BSP was detected using rabbit polyclonal primary antibody LF-6 (a generous gift from Dr. Larry Fisher, NIDCR) and a goat anti-rabbit HRP-conjugated secondary antibody (Amersham). An enhanced chemiluminescent substrate was used to detect reactivity on the membrane.

Infection was performed by introducing $3x10^9$ particles per mililiter of the adenovirus into the culture system for 48 hours. Afterward, the calvaria were washed and the infection medium was replaced by DMEM, ascorbic acid phosphate, β-glycerol phosphate, and 1 μM phosphate, which was used for the remainder of the experiment.

2.2 Raman Instrumentation and Analysis

Mineralization in tissue cultures was observed using a custom-build built Raman microscope. The microscope consisted of a Nikon Eclipse Ti inverted microscope with a collimated 830 nm laser that was directed through the rear port and focused on the specimen in the fontanel region through a 20x/0.45NA objective (Nikon). Raman-

scattered light was collected in backscatter mode into a spectrograph and projected onto a CCD. Spectra were acquired with 5-minute integration once every hour to allow for simultaneous measurement of several calvaria. The Raman probe interrogated a portion of the interparietal bone/fontanel interface in the middle of the bone front. Mineral deposition amount in the tissue was measured using the PO_4^{3-} v_1 band height (957–967 cm^{-1} region) to phenylalanine (Phe) band height (1001 cm^{-1}) ratio. This measurement assumed that the amount of phenylalanine remained constant throughout an experiment.

To resolve the components of the 956–967 cm^{-1} band envelope in the Ad-BSP treated calvaria, Raman spectra were fit to five pseudo-Voight functions in the 900–1020 cm^{-1} region corresponding to two collagen bands at 925 and 940 cm^{-1} two mineral bands at 956 and 967 cm^{-1}, and a phenylalanine band at 1001 cm^{-1}. The pseudo-Voight function, being the weighted sum of a Gaussian and Lorentzian function, is a standard line shape for spectral fitting.(Dasgupta Fizika-A Zagreb 2000:9:61, Sundius J Raman Spec 1973:1:471) The parameters band position, height, width and percent-Lorentzian, were optimized using the Matlab algorithm LSQCURVEFIT. Band positions were constrained to a 2 cm^{-1} optimization window to keep functions representing minor spectral components from drifting.

To identify potential sources of mineralization, kinetic data were fit to functions hypothesized to represent native and BSP-mediated mineralization. A linear combination of a log-function and an integrated sine function represented as

$$g(t) = b_1 \ln(t - b_2) + b_3 \int_0^t d\tau \left(\sin\left(2\pi b_4 (t - b_5)\right) + 1\right)$$

was fit to the time-series data by optimizing b_n using the LSQCURVEFIT algorithm as before.

3 Results

Overexpression in calvaria was verified by measuring BSP levels after 24 or 48 hours in medium loaded with the BSP-adenovirus. Western blot (Figure 4.1A) showed that expression levels were much greater after 48 hours exposure to the adenovirus. Thereafter, elevated BSP levels persisted in both the tissue and medium for 7 days compared to GAPDH controls (Figure 4.1B). Time-zero for mineralization was defined by introducing an inorganic phosphate medium immediately after infection.

Mineral deposition in the calvarial tissue was followed by Raman spectroscopy over 5 days. Analysis of mineral-to-matrix in time showed highly variable amounts of mineral deposited in the tissue across all three groups. This prevented a meaningful analysis based on pooled values for tissue mineral content. Individual mineral-to-matrix profiles contained several features that were unique to the Ad-BSP treatment group. Ad-LacZ and control groups exhibited mineral that underwent several periods of mineralization as measured by mineral-to-matrix ratio. Spectra revealed that mineral initially deposited into the tissue with a band centered at 957 cm^{-1}, which remained throughout the duration of the 5-day culture. Mineralization in the Ad-BSP group proceeded in a logarithmic fashion characterized by rapid initial deposition followed by a decaying deposition rate (Figure 4.2). Those calvaria that did not show definite logarithmic growth still displayed periodic mineralization behavior similar to those in control groups. In one calvarium, both periodic and logarithmic mineralization components were evident (Figure 4.3). Periodic mineralization was modeled with an integrated sine function representing circadian-mediated mineralization hypothesized in Chapter 3. This shows that the native mechanism of periodic deposition continues to function after treatment with Ad-BSP, although it is masked to varying degrees.

Raman spectra revealed time dependent changes to the mineral structure in the highly mineralizing Ad-BSP treated calvaria, seen in Figure 4.3A, that were not seen in other groups. Initial mineral had a wide symmetric phosphate v_1 band position at 956 cm^{-1}, which remained until after the period of rapid deposition. Starting at T=43 hours the mineral transitioned into a second phase characterized by a PO_4^{3-} v_1 band centered at 965 cm^{-1}. The transition between phases seemed to occur mainly inside a 30-hour window where the band maximum shifted significantly (Figure 4.3B). The final shape of the band at 120 hours was highly asymmetric. The band could be fit to two Gaussian/Lorentzian functions centered at 956 and 967 cm^{-1}, referred to in Figure 4.3C as components I and II respectively. No band was observed at 1010 cm^{-1}, which has been assigned to HPO_4^{2-}. By applying this model to the entire time-series data set the dynamics of components I and II were measured. Initial mineral was deposited in the form of component I which increased to a maximum at 35 hours, after which it declined gradually. Band width for component I during this period of growth was stable at 31 cm^{-1} after which it gradually narrowed to 25 cm^{-1} at T=120 hours. The amount of component II in the system was initially small and gradually increased in time to eventually exceed component I at 80 hours. Initial band widths of Component II were not stable due to its relatively small contribution to the overall band envelope. At T=60 hours, component II had a stable bandwidth at 25 cm^{-1} which decreased to 20 cm^{-1} at T=120. The sum of component I and II resembled the logarithmic profile seen by measuring band height directly.

4 Discussion

The kinetics of calvarial mineralization in the presence of excessive amounts of the nucleator protein, BSP, resulted in a varied mineral response, ranging from several periodic depositions to a single logarithmic deposition. The varied response in mineralization was due to two competing mechanisms for nucleation: first, native tissue mineralization mediated by an NCP ensemble of nucleator and inhibitor proteins, and second, predominant BSP-mediated nucleation. BSP-mediated mineralization appears to proceed by initially precipitating into a transient form of $Ca_x(PO_4)_y$ that can be characterized as amorphous calcium phosphate having an initial bandwidth ~10 cm^{-1} wider than typical apatites (16–22 cm^{-1}). Formation of amorphous Ca-PO_4 *in vitro* has been characterized as having a band centered in the 945–952 cm^{-1} and widths three to four times that of crystalline apatite. [14, 20, 21] The initial phase reported here is narrower and shifted higher than reported values. This is likely due to the stabilizing role of the BSP acidic domains. Following the initial formation, the mineral undergoes a transformation to where two phosphate components exist, evidenced by a poorly resolved doublet at 956 cm^{-1} and 967 cm^{-1}. During this period both band components narrow, indicative of crystallization. Apatite typically has a PO_4^{3-} v_1 band in the 956–961 cm^{-1} range, but mineral bands as high as 967 cm^{-1} typically have not been attributed to apatite. Hydrated forms of Ca-PO_4 are capable of producing a PO_4^{3-} v_1 at 967 cm^{-1}. For example, octacalcium phosphate, seen in Figure 4.5, is characterized by a PO_4^{3-} v_1 doublet band at 956 cm^{-1} and 967 cm^{-1}. Fowler et al. described the structure of OCP as having two layers: an apatite-like layer, having the same Ca-PO_4 arrangement as half a unit cell of apatite, and a hydrated layer containing HPO_4^{2-} and H_2O.[22] Interestingly, HPO_4^{2-} bands at 1004 cm^{-1} and 1010 cm^{-1} were not observed in the time-series data, but their presence cannot

be ruled out. Jager et al. observed by solid-state nuclear magnetic resonance that the surface of synthetic apatite nanocrystals resembles that of an OCP-like hydrated layer where ordered H_2O is bound on the inside of the layer and disordered HPO_4^{2-} is on the outside.[23] The splitting of the ν_1 band is likely due to the formation of hydrated layers where the 956 cm^{-1} band corresponds to PO_4^{3-} in the middle of an apatite-like layer and the 967 cm^{-1} band corresponds to PO_4^{3-} near the hydrated layer (shown in the insert to Figure 4.5). This would suggest that component II is an indirect measure of structural water that has infiltrated amorphous Ca-PO_4 clusters as part of a general crystallization process. The authors would like to point out that although BSP-mediated mineralization appears to eventually form a hydrated crystal phase, this is likely due to the underrepresentation of other non-collagenous proteins that are also known to attach to apatite surfaces, such as osteopontin, osteocalcin, and dentin matrix protein 1. These proteins may prevent extensive OCP formation, facilitating direct apatite formation from amorphous Ca-PO_4.

It is proposed that the split PO_4^{3-} ν_1 components observed in BSP-mediated mineralization stem from the initial formation of an amorphous phase, followed by the formation of hydrated layers within the amorphous phase resulting in a hydrated crystal resembling OCP. Thereby, both ACP and OCP may be important precursors to bone apatite.

Acknowledgments

This work was done in collaboration with Guisheng Zhao and Renny Franceschi who oversaw the maintenance of all mouse colonies and tissue cultures used in this study.

Guisheng Zhao performed the adenovirus transfection of calvaria used in this chapter. Christopher Wilson provided technical assistance and consultation on fluorescence microscopy and handling tissue.

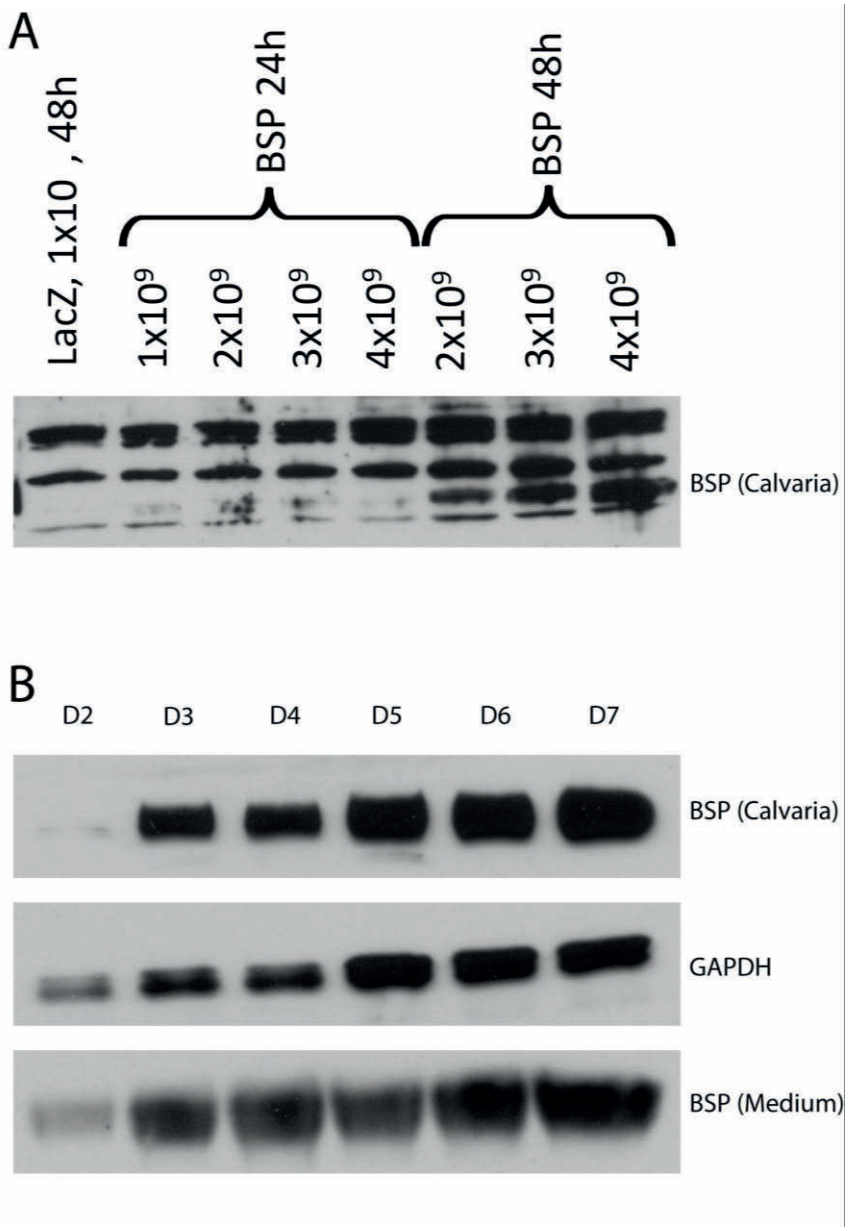

Figure 4.1 Western blot of bone sialoprotein expression in calvarial tissue cultures. Images of electrophoresis gels containing A) BSP expression levels after treatment with BSP-adenovirus for 24 or 48 hours with $1x10^9$–$4x10^9$ particles of the adenovirus, and B) BSP expression levels in time (Day 2 to Day 7) in the calvarial tissue and medium. GAPDH was used as an internal standard.

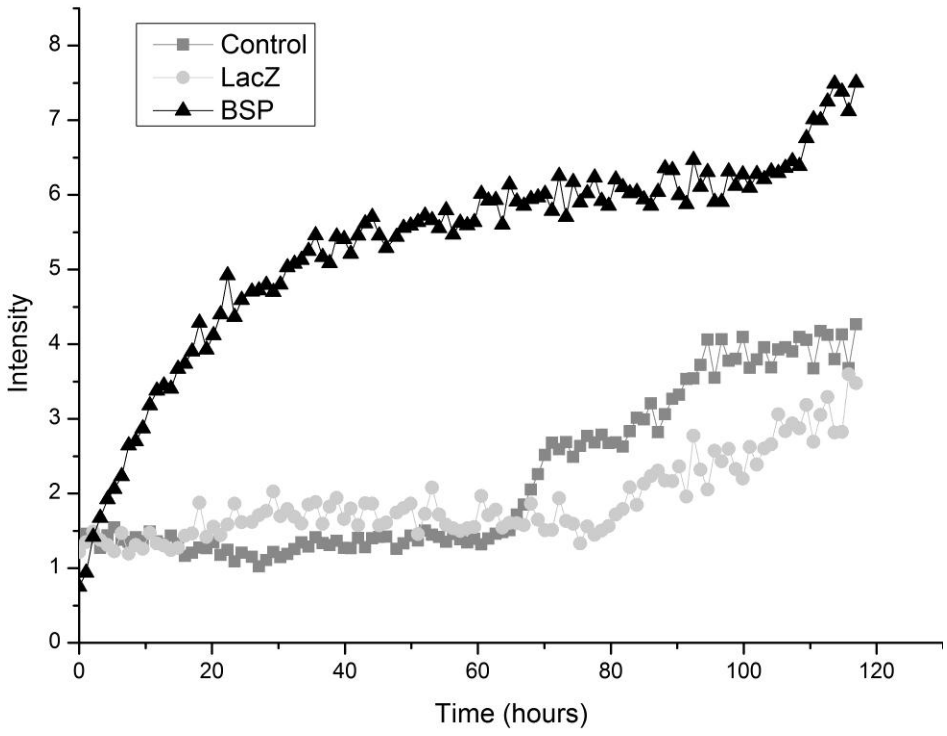

Figure 4.2 Mineral deposition profiles for calvaria in Ad-BSP treated, Ad-LacZ treated, and control groups. Time-course data are representative measurements from single calvaria in each treatment group over 120 hours of culture.

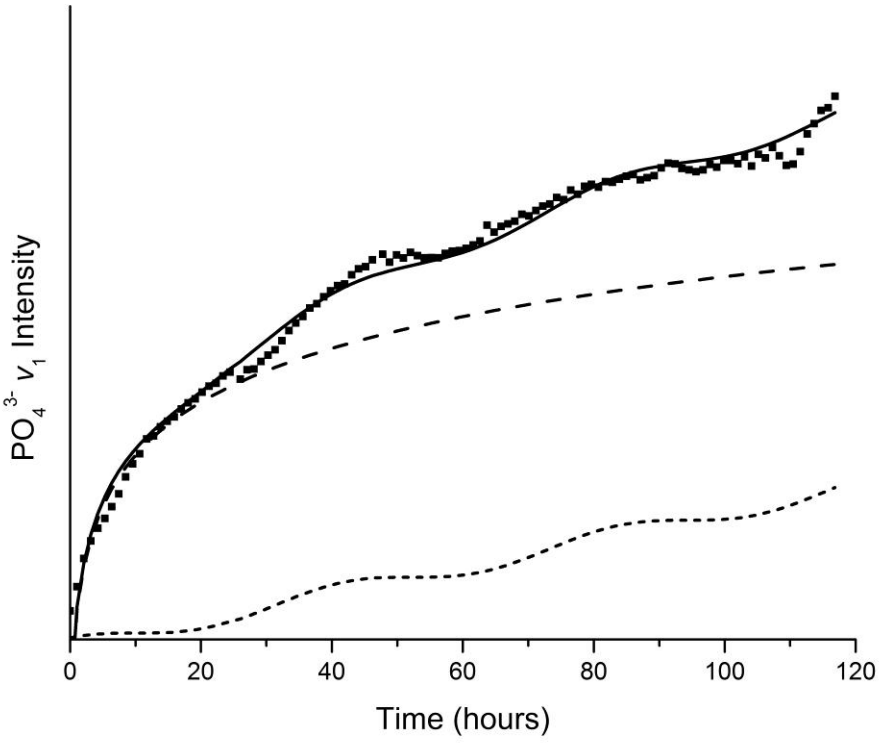

Figure 4.3 Plot showing partial masking of native mineralization by BSP-mediated mineralization. Data show the evolution of the Raman PO_4^{3-} band height in a BSP-overexpressed calvarium. Lines indicate least-squares fit functions: long dashes represent a log function, short dashes represent a periodic function, and the solid line represents the combination of the two.

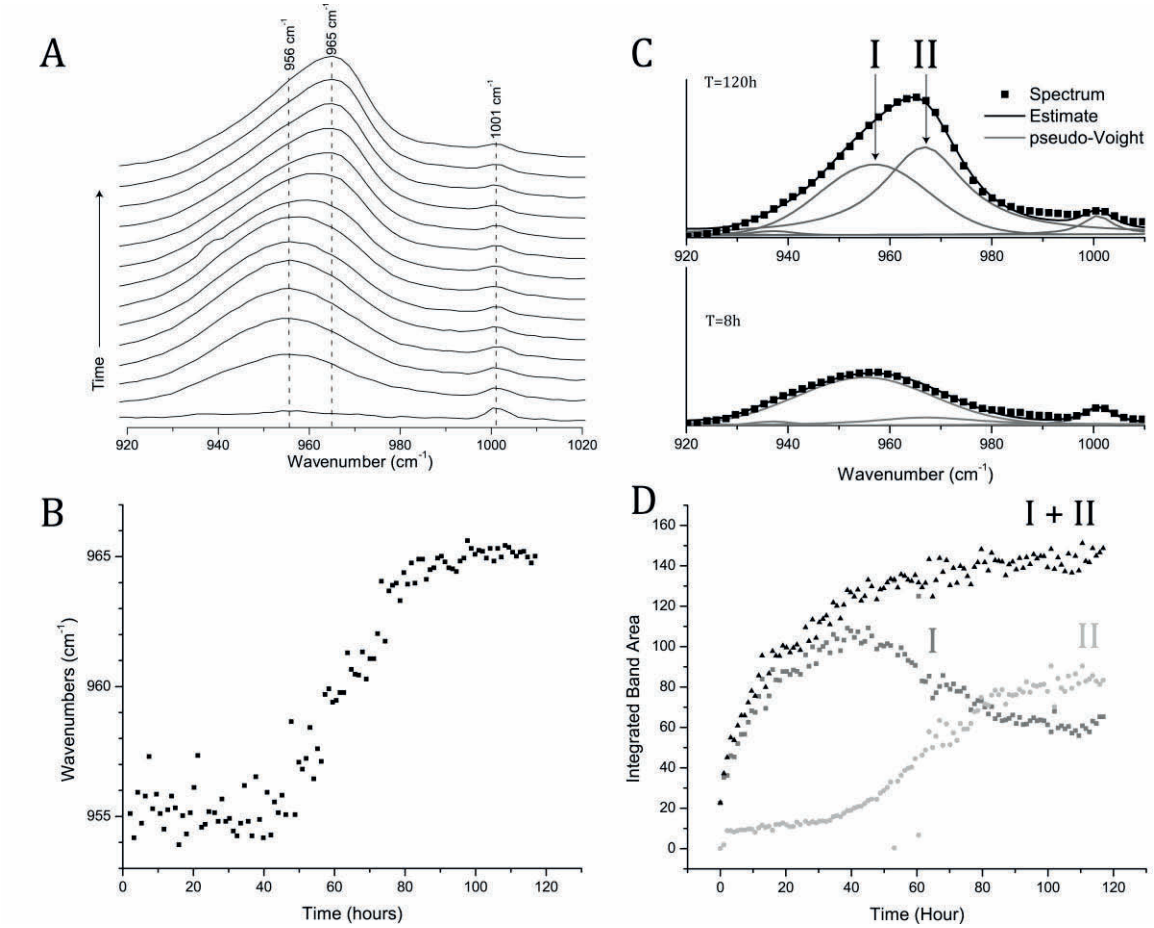

Figure 4.4 Raman view of the phase transition during BSP-nucleated mineralization. Figures of Raman spectral analysis of deposited mineral in a BSP overexpressed calvarium: A) waterfall plot of spectra with 8-hour intervals, B) plot of spectral shift of the entire band envelope, C) least-squares band fitting for resolution of two bands centered at 956 cm^{-1} (I) and 967 cm^{-1} (II), D) Dynamic variations in integrated band areas for components I and II in time.

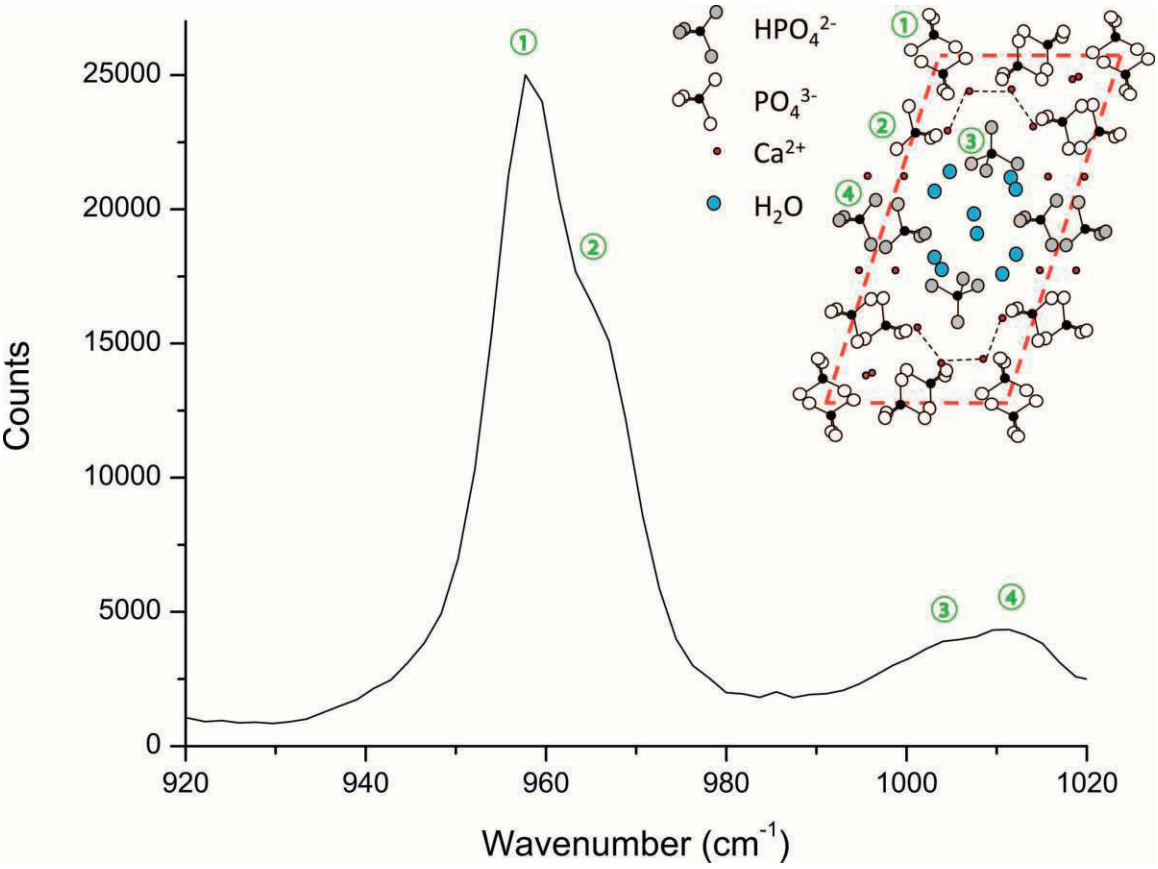

Figure 4.5 Raman spectrum of the v_1 region of octacalcium phosphate. Partially overlapping v_1 bands correspond to two environments of PO_4^{3-} in the apatite layer, (956 & 967 cm^{-1}), and two environments of HPO_4^{2-} in the hydrated layer (1004 & 1011 cm^{-1}). Band assignments are based on Ref (Fowler, Brown Chem. Mater 1993).

References

1. Oldberg A, Franzen A, Heinegard D (1988) The primary structure of a cell-binding bone sialoprotein. J Biol Chem 263:19430-19432

2. Aubin JE (2008) Mesenchymal Stem Cells and Osteoblast Differentiation. In: Bilezikian JP, Raisz LG, Martin TJ (eds) Principles of Bone Biology. Academic Press, Burlington, p 85-108

3. Chen J, Shapiro HS, Sodek J (1992) Development expression of bone sialoprotein mRNA in rat mineralized connective tissues. J Bone Miner Res 7:987-997

4. Malaval L, Wade-Gueye NM, Boudiffa M, Fei J, Zirngibl R, Chen F, Laroche N, Roux JP, Burt-Pichat B, Duboeuf F, Boivin G, Jurdic P, Lafage-Proust MH, Amedee J, Vico L, Rossant J, Aubin JE (2008) Bone sialoprotein plays a functional role in bone formation and osteoclastogenesis. J Exp Med 205:1145-1153

5. Hunter GK, Goldberg HA (1993) Nucleation of hydroxyapatite by bone sialoprotein. Proc Natl Acad Sci U S A 90:8562-8565

6. Hunter GK, Goldberg HA (1994) Modulation of crystal formation by bone phosphoproteins: role of glutamic acid-rich sequences in the nucleation of hydroxyapatite by bone sialoprotein. Biochem J 302 (Pt 1):175-179

7. Hunter GK, Hauschka PV, Poole AR, Rosenberg LC, Goldberg HA (1996) Nucleation and inhibition of hydroxyapatite formation by mineralized tissue proteins. Biochem J 317 (Pt 1):59-64

8. Fujisawa R, Tamura M (2012) Acidic bone matrix proteins and their roles in calcification. Front Biosci 17:1891-1903

9. Yang Y, Mkhonto D, Cui Q, Sahai N (2011) Theoretical study of bone sialoprotein in bone biomineralization. Cells Tissues Organs 194:182-187

10. Yang Y, Cui Q, Sahai N (2010) How does bone sialoprotein promote the nucleation of hydroxyapatite? A molecular dynamics study using model peptides of different conformations. Langmuir 26:9848-9859

11. Baht GS, Hunter GK, Goldberg HA (2008) Bone sialoprotein-collagen interaction promotes hydroxyapatite nucleation. Matrix Biol 27:600-608

12. Tye CE, Hunter GK, Goldberg HA (2005) Identification of the type I collagen-binding domain of bone sialoprotein and characterization of the mechanism of interaction. J Biol Chem 280:13487-13492

13. Nudelman F, Pieterse K, George A, Bomans PHH, Friedrich H, Brylka LJ, Hilbers PAJ, With Gd, Sommerdijk NAJM (2010) The role of collagen in bone apatite

formation in the presence of hydroxyapatite nucleation inhibitors. Nature Materials 9:1004-1009

14. Crane NJ, Popescu V, Morris MD, Steenhuis P, Ignelzi JMA (2006) Raman spectroscopic evidence for octacalcium phosphate and other transient mineral species deposited during intramembranous mineralization. Bone 39:434-442

15. Lowenstam HA, Weiner S (1985) Transformation of amorphous calcium phosphate to crystalline dahillite in the radular teeth of chitons. Science 227:51-53

16. Lowenstam HA, Weiner S (1989) On Biomineralization. Oxford University Press, Inc., New York

17. Weiner S (2006) Transient precursor strategy in mineral formation of bone. Bone 39:431-433

18. Grynpas MD, Omelon S (2007) Transient precursor strategy or very small biological apatite crystals? Bone 41:162-164

19. Colfen H (2010) Biomineralization: A crystal-clear view. Nat Mater 9:960-961

20. Seah RK, Garland M, Loo JS, Widjaja E (2009) Use of Raman microscopy and multivariate data analysis to observe the biomimetic growth of carbonated hydroxyapatite on bioactive glass. Anal Chem 81:1442-1449

21. Sauer GR, Zunic WB, Durig JR, Wuthier RE (1994) Fourier transform Raman spectroscopy of synthetic and biological calcium phosphates. Calcif Tissue Int 54:414-420

22. Fowler BO, Markovic M, Brown WE (1993) Octacalcium phosphate. 3. Infrared and Raman vibrational spectra. Chemistry of Materials 5:1417-1423

23. Jager C, Welzel T, Meyer-Zaika W, Epple M (2006) A solid-state NMR investigation of the structure of nanocrystalline hydroxyapatite. Magn Reson Chem 44:573-580

CHAPTER V

MINERALIZATION IN FRACTURE HEALING WITH ALENDRONATE TREATMENT IN THE BRTL/+ MOUSE MODEL OF OSTEOGENESIS IMPERFECTA

1 Introduction

Osteogenesis imperfecta (OI) is a debilitating bone disease that affects preadolescent children and is characterized by bone fragility and recurrence of fracture. OI stem from inherited glycine (Gly) mutations in the primary structure of the Type I collagen molecule. Gly has a small side-chain allowing for tight turns in the secondary structure, which is essential for collagen helix formation. Gly substitution results in disruption of the helical structure and therefore compromised fibril strength. There are several forms of OI which are classified by severity of deformation.[1] N-terminus defects cause the most extreme cases of OI (Type II) and usually result in infantile death within the first week due to underdevelopment of the thoracic cavity. However, mid-chain substitutions result in mildly severe OI (Type IV). Children with OI Type IV typically appear normal until walking age when rods or braces become required for mobility. At this point bone density by radiology shows severe osteoporosis, and fractures are likely to occur.

Fracture healing is a dynamic process that involves both osteoblasts and osteoclasts. A histomorphometric study of biopsies from OI patients showed an increase in the bone formation rate and, for moderate to severe forms of OI, an increase in bone resorption parameters, decreased cortical width and decreased trabecular bone volume fraction.[2] The underlying osteoblastic and osteoclastic mechanisms that affect these histomorphometric outcomes may both be affected by bisphosphonates,[3] and bisphosphonate treatment can potentially increase cortical width in OI patients due to a disruption in bone resorption[4]. Therefore, several controlled clinical studies have utilized bisphosphonates in an effort to prevent or reduce the number of fractures in OI patients.[5-8] These studies all show improvements in DXA based outcomes in the vertebral column, although fractures still occurred in some patients receiving treatment.[6-8]

Bisphosphonates have a high affinity for bone mineral and, in an early assessment of alendronate, were predicted to have a half-life of over 10 years.[9] Bisphosphonate retention depends on the mechanism of delivery,[10] and the rate of bone turnover. In pediatric patients, pamidronate has been detected in urine up to 8 years after cessation of treatment.[11] In one extreme pediatric case with a high bisphosphonate dose, there were still noticeable radiographic abnormalities 6 ½ years after the cessation of pamidronate and a subsequent fracture did not heal after 2 years.[12] Furthermore, bisphosphonate treatment leads to radiographic sclerosis in metaphyses, has been associated with an increased risk of osteonecrosis of the jaw, and subsequent microdamage may not heal, These concerns have led to caution in treating growing OI patients with bisphosphonates.[13] These risks, and the underlying cellular activity that contributes to

bone formation and resorption during fracture healing, have all led to a number of fracture healing studies with anti-resorptive agents.

Fracture healing with antiresorptives has been investigated in both clinical and preclinical studies. One randomized, double-blind, placebo-controlled trial with zoledronic acid infusions following a hip fracture did not show an increased risk for delayed union.[14] Similarly, in pediatric OI patients, bisphosphonate treatment is not usually associated with altered fracture healing although intravenous pamidronate treatments may lead to delayed osteotomy healing.[15, 16] These important clinical studies are limited in their ability to pinpoint the ultrastructural, morphological and biomechanical changes so animal models have been used to investigate bisphosphonate treatment during fracture healing.[17-29] Early studies with non-nitrogen containing bisphosphonates indicate that high doses can lead to non-union,[24] and, in cases where there was a bony union, there may not be any effect on the callus biomechanical properties.[23, 27] The effects are quite different with the nitrogenous bisphosphonates such as alendronate, zoledronic acid, incandronate and pamidronate. Zoledronic acid may not affect the rate or pattern of endochondral ossification in the early stages of healing.[28] Later in the healing process when there is normally active remodeling, the results generally indicate an increase in callus size and structural biomechanical changes, although the specifics depend on the particular bisphosphonate chosen, dose, delivery method, and timepoint of healing.[17, 18, 20-22, 26, 28, 29] However, halting alendronate treatment at fracture results in calluses with normal radiographic appearance and biomechanical stiffness.[29] With high doses of incadronate, the fracture callus has less drug than the contralateral (intact) bone when treatment is halted at fracture.[26]

However, continuing treatment during healing results in an increased incadronate concentration,[26] and in high doses this corresponds to a larger callus and increased ultimate load (in comparison to the intact bone) later in healing.[30] In light of these data, and the residence time of bisphosphonates, it is important to study similar questions in growing OI scenarios.

To study fracture healing in an OI environment we performed fracture experiments on the Brtl/+ mouse model. The Brtl/+ mouse mimics the collagen defect by genetically inducing a heterozygous Gly→Cys substitution (knock-in) at mid-chain residue 349 in the *col*1*a*1 allele. Brtl/+ mice show deformities in the long bones along with fragility, and exhibit radiographic features consistent with OI Type IV.[31] Much like in human OI, Brtl/+ mice undergo a period of adaptation to the condition between 2 and 6 months after which bone stiffness and strength resemble bones from WT mice.[32] It remains unclear whether treatment of BPs should be halted at the time of fracture or continued during healing in OI, so both scenarios were examined. Alendronate was used in this study because of its high use in pediatric treatment of OI. The main purpose of this study was to investigate how treatment of BPs at various time points impacts regenerating tissue.

2 Materials and Methods

2.1 Study Design & Animal Model

Male Brtl/+ mice, the progeny of Brtl/Brtl and WT parents, and male WT mice were enrolled into the study at 2 weeks (2w) of age. The breeding scheme utilized intercrosses with an occasional backcross. Upon enrollment, the mice were randomly

assigned into one of 12 experimental groups based on two variables (Figure 5.1). The first variable, the alendronate treatment protocol, was either (1) no treatment, (2) treatment only before the fracture or (3) treatment before and after fracture. All mice were weighed once weekly and mice in bisphosphonate treatment groups received a 0.219 μg/g subcutaneous injection of alendronate (Sigma Aldrich).[33] The second variable, time point, was 1, 2, 3 or 5 weeks of healing to capture the phases of fracture repair that encompass the initial callus formation, bone formation, callus bridging and early remodeling. At 8 weeks of age, an intramedullary pin was inserted in one randomly chosen tibia, a fracture was created using a guillotine device, and the limb was stabilized using a tape splint as previously described.[34] Animals received a buprenorphine injection pre-operatively to alleviate pain. A radiograph was taken at the time of fracture to categorize the fractures as simple, wedge, or complex using the Orthopaedic Trauma Association classification system.[35] Following euthanasia, intact and fractured tibiae were dissected free and prepared for analysis as described below. All experiments were performed under approval of the University of Michigan IACUC.

2.2 μCT

Tibiae were scanned using a commercially available μCT system (eXplore Locus SP, GE Healthcare Pre-clinical Imaging) using a source voltage of 80 kVp, a source current of 80 μA, 2x2 detector binning and an exposure time of 1600 ms. A 0.5 mm aluminum filter and beam flattener were used to minimize beam hardening artifacts.[36] The raw data were corrected with bright and dark pixel corrections and a sinogram based filter, and were reconstructed using a Feldkamp cone beam backprojection algorithm to obtain images with an 18 μm isotropic voxel size. The callus volume, bone volume

fraction (BVF) and tissue mineral density (TMD) of bone in the callus and residual cortical bone were measured (MicroView 2.2, GE Healthcare Preclinical Imaging) using a segmentation approach very similar to a previously published technique.[34] Briefly, a spline-based semi-automatic segmentation was used to define the outer callus boundary. A second spline-based segmentation in combination with a threshold-confined region growing procedure was used to select the cortical bone. A Boolean operation was then performed on these two segmentations to create a region which only included bone in the callus. This region also included the intramedullary space because healing bone was present in the marrow cavity as well.

2.3 Raman Spectroscopy

The harvested tibiae were thawed, placed in a Petri dish, and kept moist with PBS while being illuminated through a 20x 0.75NA objective with 150 mW of 785 nm laser light in a 7x100 μm line profile. Ten separate spectra were acquired from the central portion of the callus (for fractured tibiae) or tibial mid-diaphysis (for contralateral intact control limbs) to account for variation in the tissue. Spectra were collected as an image read off a CCD camera with rows containing spectral data and columns representing spatial data.[37] Image curvature due to optical aberrations were corrected using the imtransform algorithm in the Matlab Image Processing toolbox. Wavenumber calibration was performed daily using neon atomic emission bands and the 732 cm^{-1} Raman band of Teflon. Spectra were baselined using a polynomial-based algorithm.[38]

All spectra were normalized to the height of the phenylalanine ring-breathing mode (~1002 cm^{-1}) because it is easily isolated, independent of mineral changes and relatively unperturbed by changes to collagen secondary structure compared to amide

bands. Four separate measurements were made. Crystallinity was measured as the inverse full width at half height (FWHH) of the 960 cm^{-1} peak.[39] The carbonate to phosphate ratio was calculated as the ratio of band areas for the 1070 cm^{-1} to 960 cm^{-1} peak.[40, 41] Mineral-to-matrix ratios were estimated using three different metrics. These were the area of the 960 cm^{-1} band relative to the peak areas representing hydroxyproline and proline (851, 873 and 917 cm^{-1}),[42] the height of the 960 cm^{-1} peak to the height of the CH2 wag peak (1445 cm^{-1}),[40] or the area of the 960 cm^{-1} peak relative to the area under the Amide I band.[43] When peak fitting was required, a custom MATLAB script was implemented using the Levenberg-Marquardt method of curve fitting using pseudo-Voight functions to estimate each peak. This routine included an optimization step to find the best fits for the height, width, wavenumber and %Lorentzian.

To verify that measurements at the periosteal surface correlated with bulk bone measurements, a subset of tibiae from untreated mice (n=4 brtl/+, n=5 wt) were sectioned longitudinally and spectra were obtained through the cross-section. A histogram of the spectra per bone that were closest to the surface was compared with a histogram of the remaining spectra through the cross-section.

2.4 Biomechanical Testing

A randomly assigned subset of the fractured tibiae and their contralateral (intact) controls were tested in torsion as previously described.[34] Briefly, the specimens were potted using a low melting temperature metal alloy that hardens quickly while limiting heat induced damage in the ends of the bone near the potting material. The potted bone was then mounted in a custom torsion tester, wetted with saline, and tested in external rotation at 0.5°/s until failure using LabView to run a custom miniature torsion tester.

Using a MATLAB script, the raw data were filtered and the stiffness, angular displacement at failure, torque at failure and the energy to failure were measured.

2.5 Quantitative Histology

Fractured tibiae were fixed, decalcified, embedded in paraffin, and sectioned at 7 μm. The slides were then stained using (1) Safranin-O, Fast Green and Hematoxylin to assess cartilage, (2) tartrate resistant acid phosphatase (387A, Sigma Aldrich, St. Louis, MO) to assess osteoclasts or (3) picrosirius red for subsequent collagen analyses.

To analyze the Safranin-O stained slides, a custom ImageJ macro based on a color deconvolution technique was used to separate the Safranin-O component from the fast green and hematoxylin components.[44] This macro was implemented to assess both the amount of cartilage within the callus tissue and, because of an earlier report indicating additional cartilage retention in healing bone with zoledronic acid treatment,[45] the amount of cartilage within trabeculated bone of the callus. Slides from mice which healed for 1w, 2w, 3w and 5w were examined.

TRAP analyses were performed to assess osteoclast function on fractured tibiae from mice which healed for 5w. This was done because two and six month old Brtl/+ mice have an increased number of osteoclasts and osteoclast surface per bone surface,[46] alendronate works in part by affecting osteoclasts,[3] and remodeling is actively occurring after 5w of healing. Due to μCT indicating significant remodeling of the outer callus boundary between 3 and 5 weeks (Figure 5.2), osteoclast number per bone surface (OcN/BS) and osteoclast surface per bone surface (OcS/BS) were measured on the periosteal surface of both the anterior and posterior sides of the callus using commercially available software. (BioQuant, Nashville, TN)

To analyze the picrosirius red stained slides, a polarized light method was implemented based on previously published techniques.[47, 48] Briefly, a rotating stage was placed on a standard light microscope (Olympus BX-51). A linear polarizer was placed between the light source and stage and was crossed with a linearly oriented analyzer between the objective and camera. The section was placed on the stage, defining 0 deg. to align with the longitudinal axis of the bone. The stage was then rotated in increments of 5 or 10 deg. and images were captured at each stage rotation. These images were then imported into MATLAB and, using a custom script combined with the ImageJ TurboReg plugin, the images for each orientation were registered. This facilitated analysis of the polarized light images on a pixel by pixel basis. These images were segmented and thresholded to analyze the trabeculated bone of the callus separately from the residual cortical bone. The parallelism index (PI), a measure of collagen alignment, [47] was calculated for residual cortical bone and the trabeculated bone of the healing callus. Polarized light analysis was only performed for mice without alendronate treatment after 5w of healing.

3 Results

3.1 Study Design & Animal Model

Of the mice used in this analysis, 67% had simple fractures, 12% had wedge fractures, 18% had complex fractures, and 3% could not be assessed from the radiographs. There was no significant difference in fracture complexity between the Brtl/+ animals and their WT counterparts. Brtl/+ mice weigh less than their WT counterparts and, consistent with previous data,[33] the weight gain during growth is not

affected by alendronate treatment. This is important because of the breeding scheme used. Although a true filial analysis is only defined for intercrosses,[49] an analysis for all of the mice in this study (assuming the progeny are one generation younger than the youngest parent for backcrosses) indicated that the mice were up to 6 generations from the founders (mean of 3.63 generations for WT mice and 4.35 generations for Brtl/+).

3.2 µCT

µCT scans of non-fratured (left limb) and fractured (right limb) tibiae were taken of Brtl/+ mice sacrificed at 2w, 3w, and 5w post-fracture. Bone was clearly visible in the callus and along the boundary after two weeks of healing. Callus volume and bone volume fraction (BVF) were measured from scans at 2w, 3w, and 5w of healing and were analyzed by ANOVA. Callus volume decreased in time, as expected. Pairwise differences between treatment groups at 5w showed significantly larger calluses in the group continually treated with alendronate with respect to no-treatment and once-before-treatment. BVF consistently increased in time for all treatment groups, which indicates osteoblastic deposition of new bone. Pairwise differences showed significantly more bone in the calluses treated continually with alendronate. This was evident as early as 3w post-fracture. Pooled data showed that tissue mineral density (TMD) increased in time in both the callus and the residual cortical bone, although this increase was much more pronounced in the callus. This shows that both previously-mineralized and unmineralized tissues alike have a net increase of mineral throughout the healing process.

3.3 Raman Spectroscopy

Assessment of tissue by Raman spectroscopy revealed no changes to mineral crystallinity in the fracture callus that could be attributed to alendronate treatment (Figure

5.4A); however, Brtl/+ calluses had consistently low crystallinity values for each treatment group compared to WT ($p = 0.04$, 0.13, and 0.01 for none, before, and before & after groups respectively). Mineral-to-matrix ratio, which measures mineral density similar to TMD, also showed consistently low values in the Brtl/+ mice compared to WT ($p=0.11$, 0.075, and 0.004 for none, before and before & after). Continued treatment of alendronate in WT tibia led to a slight increase in mineral-to-matrix value. Although this was not found to be significant, it nevertheless enhanced the pairwise difference to the Brtl/+ genotype, which remained unchanged in the presence of alendronate. The carbonate-to-phosphate ratio showed increased carbonate content in the Brtl/+ genotype regardless of alendronate treatment ($p=0.025$, 0.42, and 0.03 for none, before and before & after).

Intact tibiae showed differences in the mineral component due to treatment and genotype. Tibiae from untreated WT mice contained mineral that was significantly lower in crystallinity. The deficit in crystallinity lessened with treatment of alendronate such that Brtl/+ tibiae in the continual treatment group resembled a level consistent with untreated WT. Also, Brtl/+ tibiae in the continually treated group showed a trend toward lower mineral content compared to WT. There was no change in mineral carbonate in the intact tibiae.

The collection region for the Raman probe was mostly superficial, which biased the measurement to periosteal surface properties. To assess whether the collection region was representative of the cortical bone, we sectioned the tibiae at the mid-diaphysis and took Raman measurements at various depths. Figure 5.4C shows the distribution of mineral-to-matrix values for the cross-sectioned and superficial bone regions for both

Brtl/+ and WT. Mean value for the Brtl/+ were 8.2±1.1 for surface and 8.6±3.0 for cross-sectional measurements, and mean values for WT were 8.7±3.1 for surface and 8.8±2.6 for cross-sectional measurements. Differences were not significant.

3.4 Biomechanical Testing

Fractured tibiae from mice that healed for 1w were not biomechanically tested due to the lack of a bony callus. The angular displacement to failure decreased from 2w to 3w and the stiffness, energy to failure and torque to failure increased from 2w to 3w and again from 3w to 5w (data not shown), implying that duration of healing is an important factor for mechanical integrity. Therefore, the highest order interaction of the main effects that was meaningful and included time was investigated using post-hoc tests to look for pairwise differences. The interaction term analyzed for the stiffness data included all three main effects. For the torque at failure, angular displacement at failure, and energy to failure, this interaction included either time and treatment or time and genotype.

After 2w of healing there was a decrease in angular displacement at failure in the animals treated with alendronate during healing compared to mice treated with alendronate before the fracture, or left untreated ($p = 0.076$; data not shown). After 3w of healing in WT mice with continued alendronate treatment, there was a decrease in stiffness in comparison to untreated WT counterparts (Figure 5.5A). Brtl/+ mice that did not receive alendronate during healing showed a reduction in callus stiffness compared to WT counterparts from each treatment group. After 3w of healing, the energy to failure and ultimate torque were decreased in Brtl/+ mice when the treatment effects were pooled (Figure 5.5B, C). After 5w of healing, fracture calluses from WT mice showed

greater stiffness with continued alendronate treatment in comparison to their untreated WT counterparts (Figure 5.5D), but this did not occur for Brtl/+ mice. When the genotypes were pooled for fractured tibia after 5w of healing, there was also an increased torque at failure and a trend toward an increased energy to failure when treatment was continued during healing (Figure 5.5E, F).

Intact tibiae also demonstrated differences with respect to treatment protocol. In the intact tibiae of animals that received 13w of alendronate injections, there was an increased torque at failure compared to halted or untreated animals (data not shown). When the effects of time and alendronate treatment were pooled, Brtl/+ tibiae showed reductions in stiffness, angular displacement to failure, torque at failure and energy to failure compared to WT (data not shown). In order to see if the biomechanical deficiencies of intact OI bone were present during fracture healing, the energy to failure for both tibiae were plotted for untreated mice. After 5w of healing, there was no statistically significant change between the fractured and intact tibiae of WT mice but the fractured tibiae of Brtl/+ mice had a significant increase in comparison to the contralateral intact tibiae (Figure 5.6).

3.5 Quantitative Histology

Data from the Safranin-O / fast green slides indicated the presence of cartilage through 2w of healing, but this had dissipated by 3w. Neither the genotype nor the alendronate treatment protocol had an impact on the amount of cartilage present in the callus. There was also no detectable change in the percentage of cartilage that contained trabeculated woven bone with alendronate treatment (data not shown).

The μCT data indicated an effect of alendronate treatment on callus volume after 5w of healing, so TRAP analysis was performed on slides from animals which healed for 5w at the periosteal callus boundary to investigate callus volume changes. A 2-way ANOVA analysis did not indicate an effect of genotype or alendronate treatment on the osteoclast surface per bone surface or in the number of osteoclasts (data not shown).

In order to better understand the increased energy to failure in the fracture callus compared to intact tibiae in Brtl/+ mice after 5w of healing, polarized light analysis was used to study the collagen structure. Plotting the mean intensity versus stage angle indicated a difference in collagen orientation between bone in the callus and the residual cortical bone in both genotypes, implying that bone in the callus is more woven in nature. Quantifying this using the parallelism index (PI) indicated that the PI for callus bone was significantly lower than residual cortical bone, verifying the woven nature of this mineralized tissue (Figure 5.7). A t-test to compare genotype differences in residual cortical bone indicated a trend toward a decreased PI, and thus decreased collagen organization, in Brtl/+ mice ($p=0.072$).

4 Discussion

Patients with OI have been treated with bisphosphonates to decrease fracture risk. This has been successful in the vertebrae, although it remains unclear how to proceed when an OI patient on bisphosphonates presents with a subsequent fracture. This study, using the Brtl/+ knock-in mouse model of OI, was designed to address this question. Continuing alendronate treatment during healing prevented remodeling of the callus, which was observed in untreated animals between 3 and 5 weeks of healing. This larger

callus, in conjunction with the increase in bone volume fraction at this time point, may explain the increase in torque at failure in this group. These results are similar to other studies that found increased callus size and the associated structural biomechanical properties when bisphosphonate is given during fracture repair.[17, 18, 20-22, 26]

When alendronate treatment was halted at the time of fracture, there were only very subtle alterations in healing when compared to the groups where no injections were ever administered. This corroborates previous studies that indicate halting bisphosphonate treatment at the time of fracture does not result in a change in callus size or structural biomechanical properties.[26, 30] When these authors quantified the amount of incandronate in the callus, there was no difference in bisphosphonate concentration between the callus and the cortical bone,[26] suggesting no additional bisphosphonate incorporated into the callus during fracture repair. However, when bisphosphonates are given during fracture repair, drug concentration has been shown to localize highly within the callus,[26, 50] suggesting a direct action within the regenerate tissue. In the present study, similar to previously published results,[33] there were noticeable bands of metaphyseal trabecular bone in mice that received alendronate (Figure 5.3B). These bands correlate with the number, frequency, and spacing of drug cycles,[51] and represent regions of high local bisphosphonate concentration.[52] While alendronate treatment over 12 weeks in Brtl/+ mice results in thicker femoral cortical bone with an increase in the ultimate load,[33] similar changes were not detected in the tibia in this study for mice treated with alendronate once weekly from 2w to 9w of age (data not shown). Because most of the bone fractures were distal to the metaphyseal trabecular bone and because there were no cortical morphological differences that would indicate

increased alendronate retention in this bone, and because alendronate has a high affinity for bone mineral, it is plausible that the local concentration of alendronate in cortical bone at the fracture site may not have been high enough to exert an effect in animals where treatment was stopped at the time of fracture.

To investigate changes in resorption at the cellular level, TRAP staining was performed. Based on the decrease in callus volume between 3 and 5 weeks of healing, this periosteal callus would have been undergoing active resorption after 5 weeks making it a good site to monitor osteoclast dynamics during fracture healing. No differences in the number of osteoclasts or in the osteoclast surface per bone surface were observed between the genotypes nor the treatment groups. This was surprising given the increased number of osteoclasts in Brtl/+ mice,[46] and data indicating an increased osteoclast surface with alendronate treatment after 3 weeks of fracture healing in a mouse model.[21] However, this may be specific to the timepoint of healing. Another study indicates a decrease in osteoclast number with incandronate at after 2w in a rat model that normalizes after 4w of healing.[26] However, these timepoints may not be consistent across studies because other data indicates a decreased osteoclast number after 6w of fracture repair with alendronate that normalizes by 16w in a rat.[20] Further, histomorphometric differences are difficult to compare within timepoints, because this data conflicts with another study that did not find an effect of zoledronic acid after 6w of fracture repair in a rat.[18] While these disparities in previously published data make a true interpretation difficult, it seems plausible that the fracture healing dynamics after 5 weeks of healing in this study supersede any potential treatment and genotype affects. Alternatively, since we only studied the periosteal callus surface, it is possible that

treatment and genotype effects are more pronounced on the interior of the callus. Additional histological assessments that were performed to investigate the endochondral ossification processes did not show any alteration in Brtl/+ animals nor, similarly to previously published results,[18, 28] any noticeable change in the rate of endochondral ossification with alendronate. This reinforces the notion that early fracture healing in Brtl/+ animals is comparable to normal healing.

To investigate this question in more depth, transient changes during healing were assessed. The energy to failure in fracture calluses from untreated Brtl/+ mice is significantly increased in comparison to the contralateral intact tibia after 5 weeks of healing. This can partially be attributed to the callus being larger than the intact tibia. However, in untreated WT mice, the callus extended beyond the location of periosteal cortical bone without resulting in a significant change in energy to failure. Taken together, this implies that an alternative mechanism may contribute to the biomechanical properties in fracture calluses from Brtl/+ mice. We investigated the collagen orientation using polarized light from Brtl/+ mice that did not receive alendronate and quantified the collagen organization in both the fracture callus and the residual cortical bone. Similar to previously published studies,[53] bone in the callus was far less organized than cortical bone (Figure 5.7) indicating that this callus bone is more woven. The magnitude of this change in collagen orientation is far greater than a possible subtle difference between the genotypes and, therefore, may govern the biomechanics during healing. However, fractured bones in *oim/oim* mice did not have increased structural properties in comparison to the contralateral intact bone,[54] so this result may be specific to the Brtl/+ mouse.

Other transient changes were also investigated during healing. No μCT imaging was performed on calluses after only 1 week of healing because, similar to previously published results,[55] these calluses were predominately soft tissue and didn't contain bone. The mineral density of bone in the callus subsequently increased as ossification progressed. Looking at changes between 2w and 3w of healing, the stiffness increased and the angular displacement to failure decreased. This is consistent with the transition from cartilage at the callus center to a bridged bony callus that was seen histologically. Therefore, 3w was the earliest healing timepoint when the calluses were bridged and cartilage was removed.

Raman spectroscopy was performed to investigate changes in healing at this 3w timepoint that may have led to the morphologic and functional changes seen after 5w of healing. The Raman assessments of mineral crystallinity, content (mineral-to-matrix) and composition (carbonate-to-phosphate) in fracture calluses were most affected by the collagen disruption in the Brtl/+ mice, and showed only slight changes due to alendronate treatment, regardless of the regimen. Distorted collagen from the Gly→Cys mid-chain substitution, evident in polarized light measurements (Figure 5.7), appears to perturb mineral formation. We observed mineral from Brtl/+ fracture calluses to have reduced amounts, reduced crystallinity, and increased carbonate substitution. Alendronate treatment recovered a WT mineral phenotype in unfractured tibiae, however, the fracture callus never recovered within the observation time of this study. The causal impact of distorted collagen on mineral malformation cannot be established based on these results alone, yet it is important to note that the role of collagen in the mineralization process is significant.[56] Carbonate content was highly varied in the mineral from the Brtl/+ mice.

In Chapter 6 we show that increased carbonate content was associated with lower crystallinity values, increased internal strain and smaller particle sizes. Each of these characteristics has been linked to reduced bone strength.[57] This would suggest that abnormal mineral content contributes to the Brtl/+ phenotype of fragile bones.

A pooled plot of crystallinity vs. mineral-to-matrix ratio with indicated Brtl/+ and WT genotypes (Figure 5.4B) reveals a positive relationship between the metrics. Maximum crystallinity values were $0.0564/cm^{-1}$ (21.7 nm) and $0.0562/cm^{-1}$ (21.6 nm) for WT and Brtl/+ respectively. These are consistent values with those measured in the developing perinatal murine calvaria of Chapter 3, which increased in crystallinity up to $0.0581/cm^{-1}$ (22.5 nm) and then stopped. It would seem that while the OI phenotype is capable of achieving mature mineral, it suffers from a certain degree of mineral underdevelopment.

BPs adsorb onto the mineral in preexisting bone and are presumed to only modify the mineral surface.[58] BPs are also known to inhibit the precipitation of new mineral,[59, 60] however this effect is 1000 times lower than the inhibition of osteoclastic resorption. (Roelofs, Princ. Bone Biol. Ch 81) Furthermore, the relatively short half-life of unbound bisphosphonates (0.5-2 hours in humans and minutes in small rodents)[61] compared to the weekly dose of alendronate administered in this study suggests that mineral inhibition by BPs had minimal impact on new bone formation.

There are also limitations in this study. Because of the lethality in Brtl/+ pups,[31] and the desire to only use male mice to control for gender, a breeding scheme was chosen to result in litters of pups that could only be Brtl/+. This required crossing Brtl/Brtl with WT mice and may induce additional recessive genetic variation. However, the Brtl/+

mice used in this study were not more than 6 generations from the WT and Brtl/+ colony founders, minimizing the effects of this breeding scheme on the results. The Brtl/+ mice used in this study still weighed less than their WT counterparts and the intact tibia showed the expected structural biomechanical deficiencies that would be expected in OI, so the mice used in the study are still a viable OI model. Another limitation is that the untreated control group did not receive saline injections as a control. This choice was made to improve translational interpretation because no 'untreated' patient would receive injections. The untreated mice were still handled weekly during weighing like their treated counterparts, and the mice which did receive treatment did not need to be sedated for the relatively simple subcutaneous injection so this bias may be minimal. Another limitation is that the ANCOVA statistical analysis used weight as a covariate when analyzing the biomechanical data instead of using the bone size directly. However, weight is an appropriate proxy for size and could be used as a covariate to analyze the fractured and intact limbs simultaneously. Last, while four time points were analyzed to encompass the range of ossification and early remodeling to understand changes in fracture healing dynamics, there are still aspects of late remodeling dynamics that were not directly examined. Investigations that look at later time points are needed to understand if fracture calluses from mice treated with alendronate during healing will ever remodel and return to a normal cortical morphology.

In conclusion, fracture calluses contain woven bone during healing that seemed to override the biomechanical deficiencies inherent in intact bones from Brtl/+ mice. Treating these mice with alendronate during fracture healing resulted in larger calluses with increased structural biomechanical properties. However, this altered the normal

dynamics of healing by preventing the decrease in callus volume later in the healing process. If the same is true in OI patients taking bisphosphonates during healing, this geometric advantage may help reduce the inherent risk of re-fracture during healing, but would increase the healing time. However, since these larger calluses will contain more bisphosphonates that could potentially reside in the skeleton for a prolonged period of time in these pediatric patients, and since fracture healing seems to be relatively normal when alendronate treatment was not present during healing, a plausible clinical approach may also be to halt treatment at the time of fracture and resume therapeutic treatment after the fracture is well healed and the callus is mostly resorbed.

Acknowledgments

I would like to thank Jeff Meganck and Dana Begun for their significant contribution to the writing of this chapter and acquisition of the biomechanical, polarized light, μCT, and histological data. Other contributors to the scientific content of this chapter include A. Swick, Kenneth Kozloff, L. Zhang, Steven Goldstein, Michael Morris, Joan Marini, and Michelle Caird. I would also like to give a special thanks to Bonnie Nolan and Kathy Sweet for their skilled assistance with the animal surgeries and care, Sharon Reske, Xixi Wang and Jason Combs for their assistance with animal husbandry and care, Dennis Kayner and Charles Roehm for their assistance with design and fabrication of the torsion testing system. Funding for this work includes support from the National Science Foundation Graduate Research Fellowship Program (JAM), the University of Michigan musculoskeletal core center (SAG; NIH AR46024), the

regenerative sciences training grant (SAG; NIH T90 DK070071), and the University of Michigan Department of Orthopaedic Surgery (MSC).

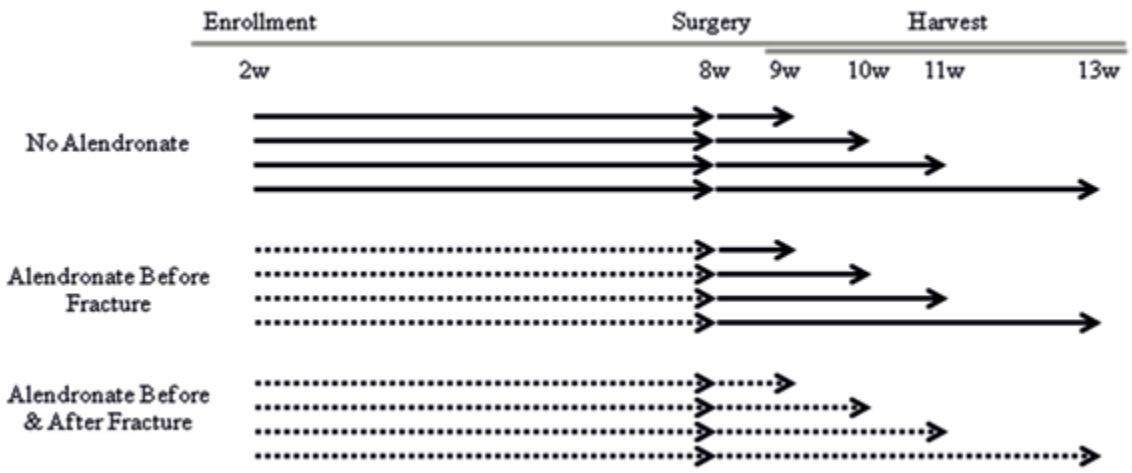

Figure 5.1 Study Design of alendronate treatment. Solid arrows indicate periods of time when no alendronate injections were given. Dashed lines indicate periods of time when mice were given subcutaneous injections of alendronate once weekly.

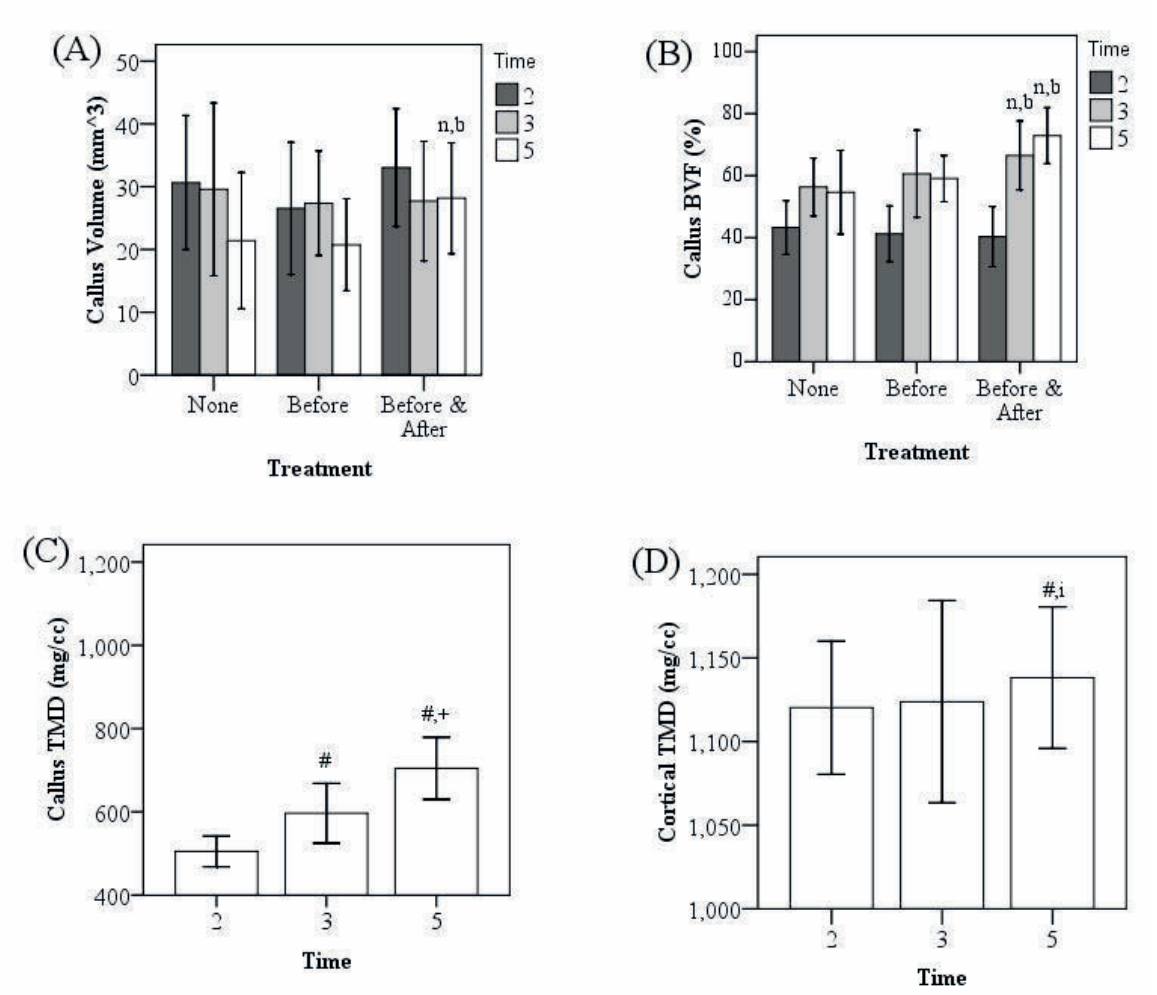

Figure 5.2 Quantitative μCT results for callus morphology and densitometry. These results are for (A) callus volume and (B) bone volume fraction during healing. The tissue mineral densities were also examined for the (C) bone in the callus and (D) residual cortical bone. Notations indicate significance ($p<0.05$) with respect to no alendronate treatment (n), alendronate treatment before fracture (b), 2 weeks of healing (#) or 3 weeks of healing (+). There was also a trend in comparison to 3 weeks of healing (i; $p=0.064$). Results are shown as mean ± one standard deviation.

Figure 5.3 μCT images of tibiae treated with alendronate. Representative sagittal planes of tibiae taken from (A) WT mice after 5w of healing and (B) from the intact tibiae of 9w old mice.

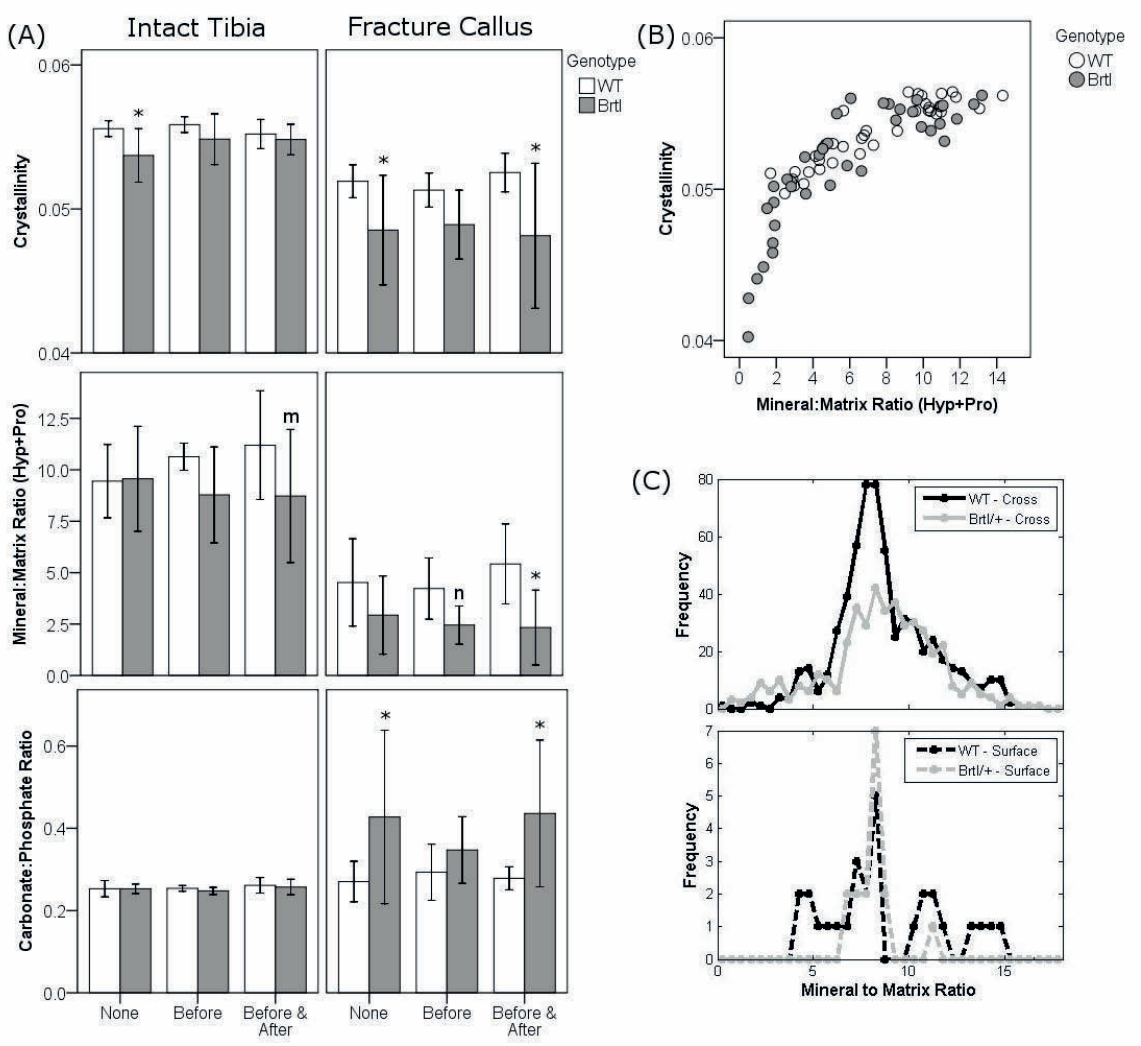

Figure 5.4 Raman microspectroscopy results after 3 weeks healing. This figure shows the results for (A) crystallinity, mineral to matrix ratio and carbonate to phosphate ratio. In (B), crystallinity was then plotted against the mineral to matrix ratio to look at relationships in these metrics. In (C), histograms for spectra taken at the surface (bottom) appear to be a reasonable sampling of spectra taken through the cortical thickness (top). Results for (A) are presented as mean ± one standard deviation. Notations indicate significance with respect to genotype (*;$p<0.05$). There were also trends toward changes in the genotype (m; $p=0.076$ and n; $p=0.075$). No significant differences were found

between treatment groups. Results for the bar graphs are shown as mean ± one standard deviation.

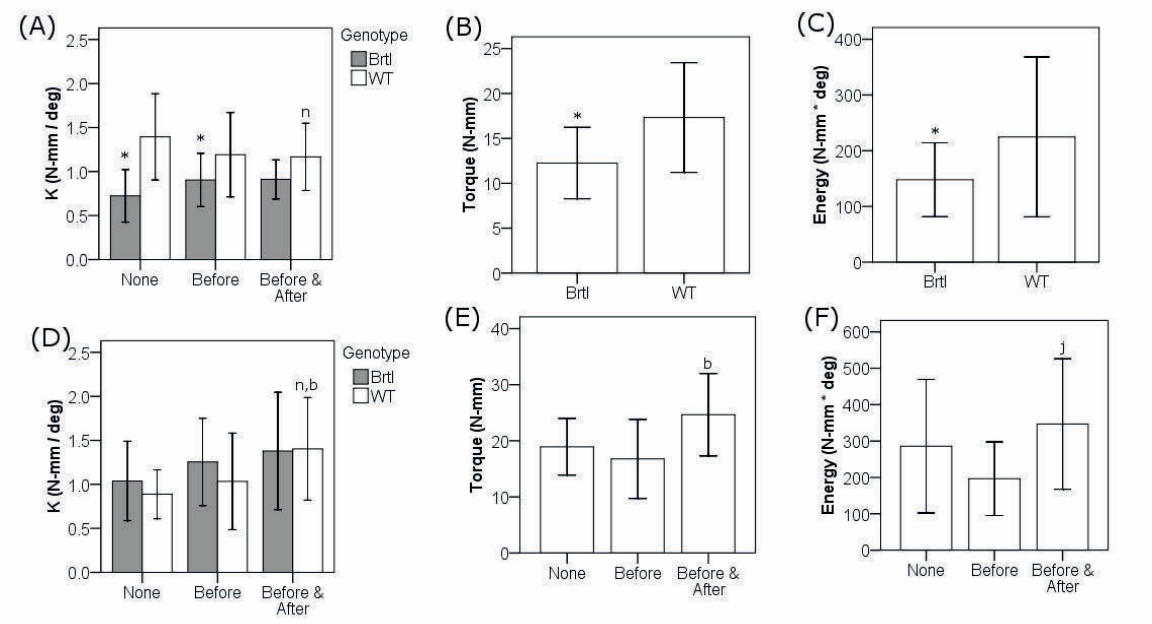

Figure 5.5 Biomechanical changes in fracture calluses based on genotypic and treatment protocol variations. The differences are shown after 3 weeks of healing (A-C) or 5 weeks of healing (D-F) for stiffness (A, D), torque at failure (B, E) or energy to failure (C, F). Notations indicate significance with respect to no alendronate treatment (n), alendronate treatment before fracture (b), or between the genotypes (*). In (F), there was also a trend toward a difference between the mice which received alendronate during healing and those where alendronate treatments were stopped at the time of fracture (j; p=0.053). Results are shown as mean ± one standard deviation.

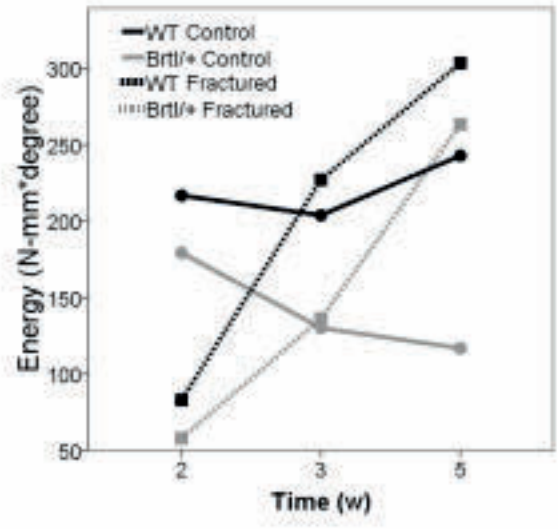

Figure 5.6 Examination of energy to failure during healing for mice which did not receive any alendronate treatments. The lines are for the intact (solid line) or fractured (dashed line) tibiae from either WT (black) or Brtl/+ (gray) mice. No error bars are shown for simplicity. There was a decreased energy to failure in both genotypes after 2 weeks of healing. After 5 weeks of healing, there was a statistically significant difference between the fractured and intact tibiae for Brtl/+ mice. Points indicate the mean.

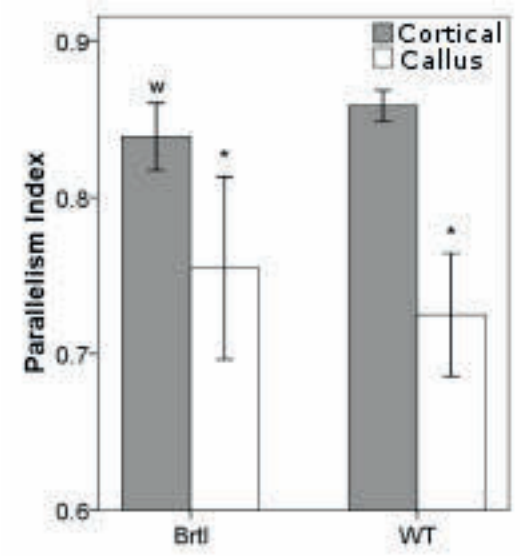

Figure 5.7 Parallelism Index results for polarized light analysis after 5w of healing. Notations indicate significance with respect to the cortical bone within a genotype (*; $p<0.05$). For the cortical bone, there is also a trend toward a difference between the genotypes (w; $p = 0.072$). Results are shown as mean ± one standard deviation.

References

1. Rowe DW (2008) Osteogenesis Imperfecta. In: Bilezikian JP, Raisz LG, Martin TJ (eds) Principles of Bone Biology. Academic Press, Burlington, p 1511-1531

2. Rauch F, Travers R, Parfitt AM, Glorieux FH (2000) Static and dynamic bone histomorphometry in children with osteogenesis imperfecta. Bone 26:581-589

3. Russell RG, Watts NB, Ebetino FH, Rogers MJ (2008) Mechanisms of action of bisphosphonates: similarities and differences and their potential influence on clinical efficacy. Osteoporos Int 19:733-759

4. Rauch F, Glorieux FH (2004) Osteogenesis imperfecta. Lancet 363:1377-1385

5. Gatti D, Antoniazzi F, Prizzi R, Braga V, Rossini M, Tato L, Viapiana O, Adami S (2005) Intravenous neridronate in children with osteogenesis imperfecta: a randomized controlled study. J Bone Miner Res 20:758-763

6. Letocha AD, Cintas HL, Troendle JF, Reynolds JC, Cann CE, Chernoff EJ, Hill SC, Gerber LH, Marini JC (2005) Controlled trial of pamidronate in children with types III and IV osteogenesis imperfecta confirms vertebral gains but not short-term functional improvement. J Bone Miner Res 20:977-986

7. Rauch F, Munns CF, Land C, Cheung M, Glorieux FH (2009) Risedronate in the treatment of mild pediatric osteogenesis imperfecta: a randomized placebo-controlled study. J Bone Miner Res 24:1282-1289

8. Sakkers R, Kok D, Engelbert R, van Dongen A, Jansen M, Pruijs H, Verbout A, Schweitzer D, Uiterwaal C (2004) Skeletal effects and functional outcome with olpadronate in children with osteogenesis imperfecta: a 2-year randomised placebo-controlled study. Lancet 363:1427-1431

9. Gertz BJ, Holland SD, Kline WF, Matuszewski BK, Porras AG (1993) Clinical pharmacology of alendronate sodium. Osteoporos Int 3 Suppl 3:S13-16

10. Ward LM, Denker AE, Porras A, Shugarts S, Kline W, Travers R, Mao C, Rauch F, Maes A, Larson P, Deutsch P, Glorieux FH (2005) Single-dose pharmacokinetics and tolerability of alendronate 35- and 70-milligram tablets in children and adolescents with osteogenesis imperfecta type I. The Journal of clinical endocrinology and metabolism 90:4051-4056

11. Papapoulos SE, Cremers SC (2007) Prolonged bisphosphonate release after treatment in children. N Engl J Med 356:1075-1076

12. Whyte MP, McAlister WH, Novack DV, Clements KL, Schoenecker PL, Wenkert D (2008) Bisphosphonate-induced osteopetrosis: novel bone modeling defects, metaphyseal osteopenia, and osteosclerosis fractures after drug exposure ceases. J Bone Miner Res 23:1698-1707

13. Marini JC (2009) Bone: Use of bisphosphonates in children-proceed with caution. Nat Rev Endocrinol 5:241-243

14. Lyles KW, Colon-Emeric CS, Magaziner JS, Adachi JD, Pieper CF, Mautalen C, Hyldstrup L, Recknor C, Nordsletten L, Moore KA, Lavecchia C, Zhang J, Mesenbrink P, Hodgson PK, Abrams K, Orloff JJ, Horowitz Z, Eriksen EF, Boonen S, Trial HRF (2007) Zoledronic acid and clinical fractures and mortality after hip fracture. The New England journal of medicine 357:1799-1809

15. Munns CF, Rauch F, Zeitlin L, Fassier F, Glorieux FH (2004) Delayed osteotomy but not fracture healing in pediatric osteogenesis imperfecta patients receiving pamidronate. J Bone Miner Res 19:1779-1786

16. Pizones J, Plotkin H, Parra-Garcia JI, Alvarez P, Gutierrez P, Bueno A, Fernandez-Arroyo A (2005) Bone healing in children with osteogenesis imperfecta treated with bisphosphonates. J Pediatr Orthop 25:332-335

17. Amanat N, Brown R, Bilston LE, Little DG (2005) A single systemic dose of pamidronate improves bone mineral content and accelerates restoration of strength in a rat model of fracture repair. J Orthop Res 23:1029-1034

18. Amanat N, McDonald M, Godfrey C, Bilston L, Little D (2007) Optimal timing of a single dose of zoledronic acid to increase strength in rat fracture repair. J Bone Miner Res 22:867-876

19. Bauss F, Russell RG (2004) Ibandronate in osteoporosis: preclinical data and rationale for intermittent dosing. Osteoporos Int 15:423-433

20. Cao Y, Mori S, Mashiba T, Westmore MS, Ma L, Sato M, Akiyama T, Shi L, Komatsubara S, Miyamoto K, Norimatsu H (2002) Raloxifene, estrogen, and alendronate affect the processes of fracture repair differently in ovariectomized rats. J Bone Miner Res 17:2237-2246

21. Gerstenfeld LC, Sacks DJ, Pelis M, Mason ZD, Graves DT, Barrero M, Ominsky MS, Kostenuik PJ, Morgan EF, Einhorn TA (2009) Comparison of effects of the bisphosphonate alendronate versus the RANKL inhibitor denosumab on murine fracture healing. J Bone Miner Res 24:196-208

22. Greiner SH, Wildemann B, Back DA, Alidoust M, Schwabe P, Haas NP, Schmidmaier G (2008) Local application of zoledronic acid incorporated in a poly(D,L-lactide)-coated implant accelerates fracture healing in rats. Acta Orthop 79:717-725

23. Koivukangas A, Tuukkanen J, Kippo K, Jamsa T, Hannuniemi R, Pasanen I, Vaananen K, Jalovaara P (2003) Long-term administration of clodronate does not prevent fracture healing in rats. Clinical orthopaedics and related research:268-278

24. Lenehan TM, Balligand M, Nunamaker DM, Wood FE, Jr. (1985) Effect of EHDP on fracture healing in dogs. J Orthop Res 3:499-507

25. Li C, Mori S, Li J, Kaji Y, Akiyama T, Kawanishi J, Norimatsu H (2001) Long-term effect of incadronate disodium (YM-175) on fracture healing of femoral shaft in growing rats. J Bone Miner Res 16:429-436

26. Li J, Mori S, Kaji Y, Kawanishi J, Akiyama T, Norimatsu H (2000) Concentration of bisphosphonate (incadronate) in callus area and its effects on fracture healing in rats. J Bone Miner Res 15:2042-2051

27. Madsen JE, Berg-Larsen T, Kirkeby OJ, Falch JA, Nordsletten L (1998) No adverse effects of clodronate on fracture healing in rats. Acta Orthop Scand 69:532-536

28. McDonald MM, Dulai S, Godfrey C, Amanat N, Sztynda T, Little DG (2008) Bolus or weekly zoledronic acid administration does not delay endochondral fracture repair but weekly dosing enhances delays in hard callus remodeling. Bone 43:653-662

29. Peter CP, Cook WO, Nunamaker DM, Provost MT, Seedor JG, Rodan GA (1996) Effect of alendronate on fracture healing and bone remodeling in dogs. J Orthop Res 14:74-79

30. Li J, Mori S, Kaji Y, Mashiba T, Kawanishi J, Norimatsu H (1999) Effect of bisphosphonate (incadronate) on fracture healing of long bones in rats. J Bone Miner Res 14:969-979

31. Forlino A, Porter FD, Lee EJ, Westphal H, Marini JC (1999) Use of the Cre/lox recombination system to develop a non-lethal knock-in murine model for osteogenesis imperfecta with an alpha1(I) G349C substitution. Variability in phenotype in BrtlIV mice. J Biol Chem 274:37923-37931

32. Kozloff KM, Carden A, Bergwitz C, Forlino A, Uveges TE, Morris MD, Marini JC, Goldstein SA (2004) Brittle IV mouse model for osteogenesis imperfecta IV demonstrates postpubertal adaptations to improve whole bone strength. J Bone Miner Res 19:614-622

33. Uveges TE, Kozloff KM, Ty JM, Ledgard F, Raggio CL, Gronowicz G, Goldstein SA, Marini JC (2009) Alendronate treatment of the brtl osteogenesis imperfecta mouse improves femoral geometry and load response before fracture but decreases predicted material properties and has detrimental effects on osteoblasts and bone formation. J Bone Miner Res 24:849-859

34. Taylor DK, Meganck JA, Terkhorn S, Rajani R, Naik A, O'Keefe RJ, Goldstein SA, Hankenson KD (2009) Thrombospondin-2 Influences the Proportion of Cartilage and Bone During Fracture Healing. J Bone Miner Res 24:1043-1054

35. (1996) Fracture and dislocation compendium. Orthopaedic Trauma Association Committee for Coding and Classification. Journal of orthopaedic trauma 10 Suppl 1:v-ix, 1-154

36. Meganck JA, Kozloff KM, Thornton MM, Broski SM, Goldstein SA (2009) Beam Hardening Artifacts in Micro-Computed Tomography Scanning can be Reduced by X-ray Beam Filtration and the Resulting Images can be used to Accurately Measure BMD. Bone 45:1104-1116

37. Esmonde-White FWL, Schulmerich MV, Esmonde-White KA, Morris MD (2009) Automated Raman spectral preprocessing of bone and other musculoskeletal tissues. Proceedings of the SPIE 7166:716605-716610

38. Lieber CA, Mahadevan-Jansen A (2003) Automated method for subtraction of fluorescence from biological Raman spectra. Appl Spectrosc 57:1363-1367

39. Kazanci M, Fratzl P, Klaushofer K, Paschalis EP (2006) Complementary information on in vitro conversion of amorphous (precursor) calcium phosphate to hydroxyapatite from Raman microspectroscopy and wide-angle X-ray scattering. Calcif Tissue Int 79:354-359

40. Dehring KA, Crane NJ, Smukler AR, McHugh JB, Roessler BJ, Morris MD (2006) Identifying chemical changes in subchondral bone taken from murine knee joints using Raman spectroscopy. Appl Spectrosc 60:1134-1141

41. Awonusi A, Morris MD, Tecklenburg MM (2007) Carbonate assignment and calibration in the Raman spectrum of apatite. Calcif Tissue Int 81:46-52

42. Kohn DH, Sahar ND, Wallace JM, Golcuk K, Morris MD (2009) Exercise alters mineral and matrix composition in the absence of adding new bone. Cells Tissues Organs 189:33-37

43. Wallace JM, Golcuk K, Morris MD, Kohn DH (2009) Inbred strain-specific response to biglycan deficiency in the cortical bone of C57BL6/129 and C3H/He mice. J Bone Miner Res 24:1002-1012

44. Ruifrok AC, Johnston DA (2001) Quantification of histochemical staining by color deconvolution. Anal Quant Cytol Histol 23:291-299

45. Smith EJ, McEvoy A, Little DG, Baldock PA, Eisman JA, Gardiner EM (2004) Transient retention of endochondral cartilaginous matrix with bisphosphonate treatment in a long-term rabbit model of distraction osteogenesis. J Bone Miner Res 19:1698-1705

46. Uveges TE, Collin-Osdoby P, Cabral WA, Ledgard F, Goldberg L, Bergwitz C, Forlino A, Osdoby P, Gronowicz GA, Marini JC (2008) Cellular mechanism of decreased bone in Brtl mouse model of OI: imbalance of decreased osteoblast function and increased osteoclasts and their precursors. J Bone Miner Res 23:1983-1994

47. Rieppo J, Hallikainen J, Jurvelin JS, Kiviranta I, Helminen HJ, Hyttinen MM (2008) Practical considerations in the use of polarized light microscopy in the analysis of the collagen network in articular cartilage. Microscopy research and technique 71:279-287

48. Silva MJ, Brodt MD, Wopenka B, Thomopoulos S, Williams D, Wassen MH, Ko M, Kusano N, Bank RA (2006) Decreased collagen organization and content are associated with reduced strength of demineralized and intact bone in the SAMP6 mouse. J Bone Miner Res 21:78-88

49. Silver LM (1995) Mouse genetics : concepts and applications. Oxford University Press, New York

50. Kozloff KM, Weissleder R, Mahmood U (2007) Noninvasive optical detection of bone mineral. J Bone Miner Res 22:1208-1216

51. Al Muderis M, Azzopardi T, Cundy P (2007) Zebra lines of pamidronate therapy in children. The Journal of bone and joint surgery 89:1511-1516

52. Kozloff KM, Sinder BP, Caird MS (2010) Spatial heterogeneity of bisphosphonate delivery and retention influences local healing of bone in model of disuse osteopenia. In: Transactions of the 56th annual meeting of the Orthopaedic Research Society. New Orleans, LA, USA., p 461

53. Tonna EA (1964) Fracture Callus Formation in Young and Old Mice Observed with Polarized Light Microscopy. The Anatomical record 150:349-361

54. Delos D, Yang X, Ricciardi BF, Myers ER, Bostrom MP, Camacho NP (2008) The effects of RANKL inhibition on fracture healing and bone strength in a mouse model of osteogenesis imperfecta. J Orthop Res 26:153-164

55. Duvall CL, Taylor WR, Weiss D, Wojtowicz AM, Guldberg RE (2007) Impaired angiogenesis, early callus formation, and late stage remodeling in fracture healing of osteopontin-deficient mice. Journal of Bone and Mineral Research 22:286-297

56. Nudelman F, Pieterse K, George A, Bomans PHH, Friedrich H, Brylka LJ, Hilbers PAJ, With Gd, Sommerdijk NAJM (2010) The role of collagen in bone apatite formation in the presence of hydroxyapatite nucleation inhibitors. Nature Materials 9:1004-1009

57. Paschalis EP, Mendelsohn R, Boskey AL (2011) Infrared assessment of bone quality: a review. Clin Orthop Relat Res 469:2170-2178

58. Nancollas GH, Tang R, Phipps RJ, Henneman Z, Gulde S, Wu W, Mangood A, Russell RG, Ebetino FH (2006) Novel insights into actions of bisphosphonates on bone: differences in interactions with hydroxyapatite. Bone 38:617-627

59. Fleisch H, Russell RG, Bisaz S, Casey PA, Muhlbauer RC (1968) The influence of pyrophosphate analogues (diphosphonates) on the precipitation and dissolution. Calcif Tissue Res:Suppl:10-10a

60. Kim CW, Yun YP, Lee HJ, Hwang YS, Kwon IK, Lee SC (2010) In situ fabrication of alendronate-loaded calcium phosphate microspheres: controlled release for inhibition of osteoclastogenesis. J Control Release 147:45-53

61. Bisaz S, Jung A, Fleisch H (1978) Uptake by bone of pyrophosphate, diphosphonates and their technetium derivatives. Clin Sci Mol Med 54:265-272

CHAPTER VI

A COMBINED RAMAN AND SOLID-STATE NMR INVESTIGATION OF APATITE CRYSTALLINITY

1 Introduction

Bone, a complex hierarchical composite system, is a dual-phase material composed of an organic matrix reinforced with a rigid mineral. The main component of the organic phase is type I collagen (~90%), along with small amounts of various noncollagenous proteins and polysaccharides [1, 2]. Bone mineral, on the other hand, is mainly an apatitic crystal having a structure similar to the synthetic mineral calcium hydroxyapatite (HA), $Ca_{10}(PO_4)_6(OH)_2$. However, unlike the synthetic hydroxyapatite, bone mineral is poorly crystalline and nonstoichiometric. In addition to very small amounts of other ions (such as Na^+, Mg^{2+}, F^-), bone mineral contains 5–8% carbonate ion, CO_3^{2-}, by weight. Predominantly, the carbonate is present as B-type carbonate, i.e. with carbonate substituting for phosphate ions. There is also a small amount of A-type carbonate (carbonate replacing hydroxide ion) as well as labile carbonate in the hydrated surface area. [3, 4].

Synthetic B-type carbonated apatites (CAps) are commonly used as model compounds for investigating chemical properties of bone mineral, and have been the subject of extensive research due to their importance in a variety of biomedical

applications such as grafts and scaffolds for reconstructing or regenerating bone defects, osteoconductive implant coatings, and vehicles for drug delivery [5, 6]. Several research groups have synthesized bone-like apatites under near-physiological conditions [7, 8]. The biological response to synthetic apatites, both *in-vitro* and *in-vivo*, depends, in part, on the degree of carbonation and crystallinity of the apatite. A-type carbonates are rarely used as model compounds in part because A-type carbonation is a small percentage of the total and in part because their synthesis requires high temperatures, high pressures or both [9]. Mature bovine cortical bone (BCB), murine femoral (MF) bone and human dental enamel (HE) were used to provide context for interpreting the synthetic apatite crystallinity.

Bone mineral is formed through physiological pathways subjected to highly regulated conditions in the body. Protein-mediated deposition of calcium phosphate begins mostly in the gap region in type I collagen fibrils [10]. The crystallites form into plate-like structures elongated mostly along the *c*-axis, which is parallel to the long axis of type-I collagen fibrils. Proper formation of bone mineral provides optimum bone material properties, known as bone quality. Bone mineral crystallinity measurements are commonly made as inverse band width of a mineral infrared or Raman band, or as ratio of site components of a vibrational band. In turn, such measurements are calibrated against powder X-ray diffraction data.

In the bone quality literature crystallinity is generally treated as a convenient measure of departure of mineral properties from those of reference specimens. The crystallite dimensions and microstrains themselves are not usually reported. Crystallinity is a widely used indicator of bone quality because it is associated with bone fragility [11,

12]. Deviations in bone crystallinity from values observed in healthy young adults may indicate reduced bone strength. For example, bone mineral crystallinity generally increases with age [13, 14]; and higher crystallinity is characteristic of osteoporotic bone [15-17]. Fourier transform infrared spectroscopy (FTIR) has long been used for measuring bone mineral crystallinity [16, 18]. In X-ray diffraction (XRD) crystallography, the term crystallinity is conventionally defined as a measure of the crystal length along the *c*-axis [10, 13] with a contribution from lattice strain. [19] According to the Debye-Scherrer equation, crystallinity is inversely proportional to the full-width at half-maximum (FWHM) of a reflection band along that axis. Similar crystallinity/inverse bandwidth relationships are also used in other spectroscopic techniques.

Linear correlations with powder diffraction data rather than calculations from a governing equation are usually used to define crystallinity. Akkus and co-workers have correlated CAp crystallinity and inverse Raman bandwidths, and have applied these correlations to bone mineral [20-22]. Similar correlations have been reported by Kazanci *et al.* [23]. To the best of our knowledge, no analogous correlations have been reported for solid-state nuclear magnetic resonance (NMR) data on CAps or bone, although broader NMR line shapes have been observed in disordered minerals [24-26]. Solid-state NMR spectroscopy is a powerful tool to obtain high-resolution structural information on bone specimens at the atomic-level. While ^{1}H and ^{13}C NMR experiments have been used for the structural studies of bone matrix components [27-31], ^{31}P and ^{43}Ca magic-angle spinning (MAS) NMR experiments are commonly used to study structural changes in

bone mineral [24, 32-36]. Over the past decade, solid-state NMR methodologies have also been used to study the crystallinity of semi-crystalline polymers [37-39].

Because NMR has not previously been reported for bone crystallinity measurements, we undertook a systematic study of NMR for the investigation of the structure and crystallinity of bone mineral and its substitutes, the results from ^{31}P MAS NMR measurements on a series of B-type CAps with various carbonate levels are analyzed and compared with crystallinity measurements performed by powder X-ray diffraction (XRD) and Raman spectroscopy. Carbonate content for the synthetic CAps and bone minerals was determined by FTIR. ^{31}P NMR isotropic chemical shifts and their bandwidths (FWHM) were extracted from the experimentally measured line shapes, and related to percent carbonation.

In the course of our NMR crystallinity validation, we took advantage of the opportunity to better understand the nature of carbonate composition dependence on apatite crystallinity. We observed that NMR and Raman spectroscopy show similar carbonate composition-dependent variation in the position of ^{31}P isotropic chemical shift and the wavenumber of the PO_4^{-3} ν_1 symmetric stretch. Remarkably, the composition dependence is nearly binary and is not observed in inverse bandwidths. This is relevant in understanding the mineral properties of bone, and enamel which have distinctly different carbonate contents. We supplemented our measurements with atomic force microscopy (AFM) measurements of carbonated apatite particle sizes. AFM has been used to measure bone crystallite length and length distributions [10, 40] and more recently, periodicity and deviations from periodicity of bone matrix spacings.[41, 42] Unlike vibrational and

magnetic resonance spectroscopies, AFM measures geometric properties directly, rather than indirectly.

2 Materials and Methods

2.1 Sample Preparation

Our study includes a series of synthetic carbonated apatites (CAps) with 0.26 wt%, 2.3 wt%, 3.3 wt%, 5.5wt%, 6.8 wt%, 8.5 wt%, and 10.3 wt% CO_3^{2-} content, in addition to bovine cortical bone (BCB) powder, powder from six-month old murine femora (MF) (n=2, combined), and intact adult human tooth enamel (n=2, combined). The CAp series was synthesized at low temperatures (80–90 °C) following the aqueous precipitation method published by Penel *et al.* for B-type apatites [43]. Variations in the published method were limited to replacing sodium phosphate and sodium carbonate with the corresponding ammonium salts for the purpose of reducing cationic substitution into calcium sites.

Bovine femora were harvested from freshly slaughtered animals (2–4 years old). Femora were stripped of soft tissue, and cortical bone specimens were prepared from central diaphyseal sections. Each diaphysis was sectioned on a band saw into parallelepipeds. Calcium-buffered saline was used during all machining steps to avoid heating the bone and to maintain tissue saturation and ionic balance. Sections randomly chosen from an inventory of ten femora with respect to longitudinal and circumferential location were milled into a powder while cryogenically cooled with liquid nitrogen. Right and left femora were collected from two mice, (male, C57BL6, age 6 months), and milled

into a powder in a similar fashion to the bovine bone powder. Human teeth were used as is for Raman measurements.

Crystallinity measurements by X-ray diffraction, solid-state NMR and Raman spectroscopy were carried out on the bone powders. Because the collagenous matrix has overlapping peaks with carbonate in Fourier transform infrared (FTIR) spectra of bone powder, the bovine cortical bone powder was deproteinated for FTIR analysis. However, the murine powder was not deproteinated due to a limited amount of powder.

Deproteinated bone samples were prepared according to the procedure published by Termine *et al.* [44]. Briefly, 2 g of bovine bone powder was immersed directly into 20 mL of hydrazine (95%, Sigma Aldrich) and stirred at 55 °C in a glass bottle for 1 hour. Then the temperature was increased to 60 °C. After 4 hours of reaction, the sample was washed by water then ethanol to remove viscous supernatant. After drying at 37 °C for 1 hour, the sample was immersed into 10 mL of hydrazine and stirred at 60 °C for 19 hours to completely remove all remaining protein and collagen and then rewashed with water and ethanol, and dried at 37 °C for 1 hour.

Weight percent of carbonate ions was determined by FTIR spectroscopy using $Ca_3(PO_4)_2/BaCO_3$ mixtures in KBr for calibration [45]. Additionally, the CAp series was calibrated to carbonated apatite standards analyzed coulometrically (Galbraith Labs, Knoxville, TN). The two calibrations agreed within experimental error.

2.2 Nuclear Magnetic Resonance Experiments

All solid-state ^{31}P NMR experiments were carried out on a Varian VNMRJ 600 MHz NMR spectrometer (operating at a Larmor frequency of 242.8 MHz for ^{31}P) equipped with a 4-mm triple-resonance magic-angle spinning (MAS) probe at room

temperature (25 °C) under 10 kHz MAS conditions. The ^{31}P NMR spectra were recorded using a single 5 μs excitation pulse, a 20 s recycle delay, and a 80 kHz proton decoupling during signal acquisition. Phosphorus-31 NMR chemical shifts were referenced with respect to 85% aqueous phosphoric acid. Bandwidths of the ^{31}P NMR band, measured as the full width at half maximum (FWHM), were reported in Table 1 for conventionality, and inverse bandwidths ($FWHM^{-1}$) were used as the NMR crystallinity metric for comparison to Raman and XRD.

2.3 X-Ray Powder Diffraction Experiments

XRD spectra were recorded on an X-ray powder diffractometer using a copper X-ray tube operating at 40 kV and 30 mA (Scintag X1, Thermo Optec Corp, Cupertino, CA). The specimens were scanned at a reflection angle (2θ) of 20° to 37° using a step rate of 0.5°/min. The inverse of the FWHM for the *c*-axis reflection band was used as the measure of crystallinity in the XRD spectra.

2.4 Raman Spectroscopy Experiments

All Raman experiments were performed using a locally constructed Raman microscope as described elsewhere [46]. The major components of this instrument are a 785 nm diode laser (Invictus, Kaiser Optical Systems, Inc., Ann Arbor, MI), a Nikon E600 epi-fluorescence microscope fitted with a 20x/0.75 NA S Fluor objective (Nikon, Inc., Melville, New York), a spectrograph (HoloSpec Kaiser Optical Systems, Inc.) and a deep depletion CCD detector (DU401-BR-DD, Andor Technologies, Belfast, Northern Ireland). Raman data were processed in MATLAB software (v. 7.0, The Math Works, Natick, Massachusetts) with corrections for cosmic ray spikes, image curvature, dark current, and variations in the CCD quantum efficiency. Bone spectra were digitally

resolved according to protocol reported in Ref [46]. Four Gaussian-Lorentzian functions were fit in the 900-1010 cm^{-1} region to distinguish the PO_4^{3-} ν_1 band from nearby matrix bands. No band fitting was performed on the enamel or CAp spectra as there was no interference of matrix bands. Bandwidths and shifts of the PO_4^{3-} ν_1 symmetric stretch band were reported in a similar fashion to ^{31}P NMR data; that is they were reported as FWHM in Table 1 for conventionality, and inverse bandwidths ($FWHM^{-1}$) were used as the Raman crystallinity metric. Linear regression analysis was used to compare crystallinity metrics of the CAps. Spectroscopic relationships are reported as r^2-values, coefficients and p-values.

2.5 Atomic Force Microscopy Experiments

Synthetic CAp samples were suspended in methanol at a concentration of 0.1–0.01 g/L. Aggregation of particles was minimized by sonicating the suspensions for one hour at <40°C. Particle suspensions were dropped on a mica slide and solvent was wicked away. AFM imaging was performed in tapping mode having a resolution of approximately 10 nm. Monodispersed particles lightly adhered to the slide with a surface density of approximately 50 particles/um^2. Particles were isolated digitally using the Gwyddion open-software package where images were thresholded and particles were defined by pixel connectivity. Obvious aggregates and touching particles were identified by visual inspection and digitally excluded. Particle size was measured along the longest dimension.

3 Results and Discussion

Solid-state ^{31}P NMR spectra and Raman spectra of synthetic apatites containing different carbonate levels (0.26–10.3 wt%), bovine cortical bone (BCB), and murine femora (MF) are shown in Figure 6.1and Figure 6.2 respectively. Powder XRD patterns for the same powders are shown in Figure 6.3. Band widths, band shifts, and crystallinity, were extracted from these spectra and patterns and are reported in Table 6.1. Crystallinity in the synthetic CAp series, as measured by XRD, varies inversely with ^{31}P NMR and Raman PO_4^{3-} ν_1 bandwidths. Crystallinities for the CAp series range from 20.1 nm to 58.1 nm and vary monotonically with carbonate content. NMR inverse bandwidths of the CAp series exhibit a linear relationship to crystallinity ($r^2 = 0.97$, m = 0.0127, b = 0.0667, $p_m < 0.01$, $p_b = 0.13$, Figure 6.4a) and correlate well with Raman PO_4^{3-} ν_1 inverse bandwidths ($r^2 = 0.99$, m = 6.1779, b = -0.001, $p_m < 0.01$, $p_b = 0.89$, Figure 6.4b). Raman PO_4^{3-} ν_1 inverse bandwidths also have a linear relationship with crystallinity ($r^2 = 0.98$, m = 0.0021, b = 0.0108, $p_m < 0.01$, $p_b = 0.09$, not shown).

The ^{31}P NMR spectra of the studied species (Figure 6.1) have similar line shapes, each consisting of a single and almost featureless broad peak at ~3.0–3.5 parts per million (ppm) from 85% H_3PO_4(aq), in accordance with the published ^{31}P NMR data for bone minerals and their synthetic standards [25, 26]. Although chemical shift anisotropy and heteronuclear ^1H–^{31}P dipolar coupling were completely eliminated by the high magic-angle sample spinning and high-power proton decoupling respectively, the structure-less shapes of the peaks result from the overlapping/superposition of multiple line shapes corresponding to magnetically non-equivalent phosphorous-containing sites, and from the structural disorder in the chemical environment around the phosphorous nuclei. The full-width at half-maximum (FWHM) range for the CAp series is 1.18–3.0 ppm and increases

with increasing carbonate content, whereas it varies inversely with crystallinity (Figure 6.4a). This change in bandwidth is mainly due to the continuous distribution of ^{31}P chemical shifts, which may correspond to local distortions of each phosphate site due to chemical structural effects, as well as to slight differences in the chemical composition of the samples.

What was unexpected was an abrupt transition in the position on the energy scale of both the NMR and Raman bands investigated. The transition occurs in the same short range of compositions in both cases. The ^{31}P NMR chemical shift remains constant until 5.5% CO_3^{2-}, and then increases, reaching a plateau at 8.5% CO_3^{2-} (Table 6.1). The Raman PO_4^{3-} ν_1 band exhibits similar behavior (Figure 6.2): bandwidth varies inversely with crystallinity, while the wavenumber remains constant at 961 cm^{-1} with increasing carbonate until 5.5% CO_3^{2-}, and then shifts to 958 cm^{-1} and plateaus at 8.5 wt% CO_3^{2-} (Table 6.1).

Atomic force microscopy also reveals a near-binary distribution of sizes (Figure 6.6A). We observed that in the low carbonate range crystallite lengths varied over a wide range and had average sizes of 195, 165, 175nm for 2.3, 3.5, and 5.4 wt% carbonate. The high carbonate range contained crystals with average sizes of 74, 52, 57nm for 6.8, 8.8, and 10.3wt% carbonate.

Two types of bone specimens were chosen for comparison with the CAp series: bovine cortical bone (BCB) and murine femoral (MF) bone. The BCB, taken from the mid-diaphysis of bovine femora, resembles the CAp5 apatite (6.8 wt% CO_3^{2-}). Both the ^{31}P NMR and Raman PO_4^{3-} ν_1 bandwidths of the BCB match those of CAp5 within experimental error, as does carbonate content. However, the ^{31}P NMR chemical shift is

3.50 ppm and Raman PO_4^{3-} ν_1 is 957 cm^{-1} for the BCB specimens measured here, which is just beyond the shift range seen in the highly carbonated CAp samples. On the other hand, the MF bones measured here most closely resemble CAp7 in crystallinity, ^{31}P NMR bandwidth, and Raman PO_4^{3-} ν_1 bandwidth, but not in position of the Raman PO_4^{3-} ν_1 and ^{31}P NMR bands. Importantly, MF has a carbonate content of 5.6%, while CAp7 has a carbonate content of 10.3%.

Although the mechanism that accounts for reduced crystallinity in murine bone is unknown, this unpredicted behavior appears to be consistent across spectroscopies. It is important to note that bone mineral contains two additional factors which are absent in CAps: 1) bone mineral contains a variety of trace ionic substitutions in addition to carbonate, and 2) the organic matrix surrounding the mineral causes increased strain on the lattice.

It is well known that solid solutions are capable of transitioning from one crystalline form to another or to an amorphous phase with increasing ionic substitutions. More subtle changes within a crystalline lattice such as molecular interactions can go unnoticed by XRD but can be observed by solid-state NMR and Raman. The minerals synthesized in this study form the apatitic phase throughout the range of carbonate substitution levels (0.26–10.3 wt%) as evidenced by XRD spectra (Figure 6.3). However, Raman PO_4^{3-} ν_1 band positions and ^{31}P NMR spectral shifts show a transition point between 5.5 and 6.8 wt% CO_3^{2-} that is not observed in the [002] reflection band in the XRD pattern. This transition is not a crystalline phase transition, but rather a transition of the amount of strain placed upon the PO_4^{3-} ions by the distribution of counter-ions around them. When a carbonate ion is substituted for a phosphate ion, a volume of distortion is

created around the carbonate causing a strain on the surrounding ions. Because it contains one fewer oxygen atom, the carbonate ion has a lower ionic volume than phosphate ion, which decreases strain in neighboring ions. Evidence for this can be seen in the Raman spectra where increasing carbonate substitution results in lower energy PO_4^{3-} vibrations. As in NMR, the effect can be viewed as an electrostatic effect. With low carbonate content these volumes of distortion in the apatite are likely far apart and perturb locally; but in highly carbonated apatites the distortion is continuous resulting in a bulk effect on the material. The shift occurs at a carbonate substitution level of about one in six phosphates replaced, which is approximately one carbonate per apatite unit cell. This bulk effect has been characterized by a sudden shift in the Raman PO_4^{3-} ν_1 band from 961 cm^{-1} to 958 cm^{-1} as well as a sudden shift in the ^{31}P NMR phosphate peak from 2.91 ppm to 3.36 ppm occurring in the 5.5–6.8 wt% carbonate range, as seen in Figure 6.5. NMR chemical shifts are sensitive to the shielding/deshielding of electrons, which causes a shift to a higher frequency in low electron density environments. It follows that highly carbonated apatites should also exhibit a higher chemical shift, as confirmed in this study. Human enamel (HE) had a carbonate content of 1.8 wt% and a Raman PO_4^{3-} ν_1 band centered at 961 cm^{-1} (Table 1), which is consistent with what is predicted by the locally distorted CAp samples of comparable carbonate content (0.26–5.5 wt% CO_3^{2-}).

The Raman shift for the bone specimens was 960 cm^{-1} which agrees with band shifts predicted from the CAp series based on carbonate content, and also agrees with literature values for mature bone [20]. Recently mineralized bone has a Raman shift at 955–957 cm^{-1}, which has been attributed to high HPO_4^{2-} content rather than CO_3^{2-} content [47]. However, carbonate levels have also been found to be elevated in immature bone

[48, 49]. The ^{31}P NMR peaks for the bone specimens were shifted to a higher frequency beyond the range of the most highly carbonated member of our CAp series, but nothing similar was observed in the Raman spectra. This may be attributed to the presence of additional cations (e.g. Na^+, Mg^{2+}) in the bone mineral specimens. The ^{31}P NMR chemical shifts appear to be more sensitive to these additional ions than Raman PO_4^{3-} ν_1 band position because electron density changes, but ionic volume does not. It follows that while carbonate content affects mineral crystallinity, it is not the sole determining factor for crystallinity in bone mineral. Furthermore, carbonate level may be indicative of crystallinity in synthetic minerals, but may not be the exclusive predictor of crystallinity in bone mineral.

Overall, we have analyzed the crystallinity of mature bovine cortical bone, mature mouse femur and a series of CAp with various carbonate levels using three different experimental techniques. We have found that both ^{31}P NMR and Raman PO_4^{3-} ν_1 band positions divide carbonated apatites into two classes: low carbonate/high crystallinity and high carbonate/low crystallinity. Within these classes the spectral band positions show little carbonate-composition dependence.

From a broader perspective, we have demonstrated that solid-state NMR provides excellent opportunities to probe the crystallinity of bone mineral and its synthetic substitutes. We have also shown that ^{31}P NMR inverse bandwidths correlate well with the XRD crystallinity and Raman PO_4^{3-} ν_1 inverse bandwidths. It is hoped that our study would stimulate both investigation into the implications of a binary response to carbonate substitution in apatites and broad implementation of the various cutting-edge solid-state

NMR techniques using higher magnetic fields and advanced pulse sequences to investigate bone minerals and other structurally similar bio-mineral system.

Table 6.1 Crystallinity measured by spectroscopic broadening and shifting of mineral bands with respect to carbonate content

Mineral ID	CO_3 [a] (wt%)	XRD		Raman PO_4^{3-} ν_1 [d]		^{31}P NMR	
		Crystallinity[b] (nm)	Center[c] (º)	FWHM (cm^{-1})	Center (cm^{-1})	FWHM (ppm)	δ_{iso} [e] (ppm)
CAp1	0.26	58.1±2.2	25.8	7.3±0.1	961	1.18±0.03	2.91
CAp2	2.3	47.1±1.9	25.75	9.7±0.2	961	1.58±0.04	2.91
CAp3	3.3	40.6±3.4	25.75	10.9±0.2	961	1.77±0.06	2.91
CAp4	5.5	31.5±2.0	25.75	13.3±0.2	961	2.17±0.07	2.91
CAp5	6.8	27.6±0.25	25.8	15.7±0.2	959	2.56±0.09	3.10
CAp6	8.5	22.0±2.0	25.75	16.5±0.3	958	2.6±0.1	3.36
CAp7	10.3	20.1±2.4	25.8	18.2±0.3	958	3.0±0.1	3.36
BCB[g]	6.7	26.0±0.74	25.8	16.4±0.6	957	2.7±0.1	3.50
MF[h]	5.6	21.5±1.5	25.85	18.6±0.3	960	3.1±0.1	3.57
HE[i]	1.8[f]	–	–	11.9±0.2	961	–	–

[a] Measured by FTIR as weight percent, [b] measured along *c*-axis (002) in units of nanometers, [c] *c*-axis (002) band position in units of degrees, [d] Phosphate symmetric stretch in units of wavenumbers (cm^{-1}) and band center error was lower than the instrument resolution, [e] Isotropic ^{31}P NMR chemical shift and error was less than the instrument resolution, [f] percent carbonate of human enamel was calculated from interpolated carbonate-to-phosphate ratios, I(1071)/I(961), of the CAp series, [g] bovine cortical bone, [h] murine femora, [i] human enamel.

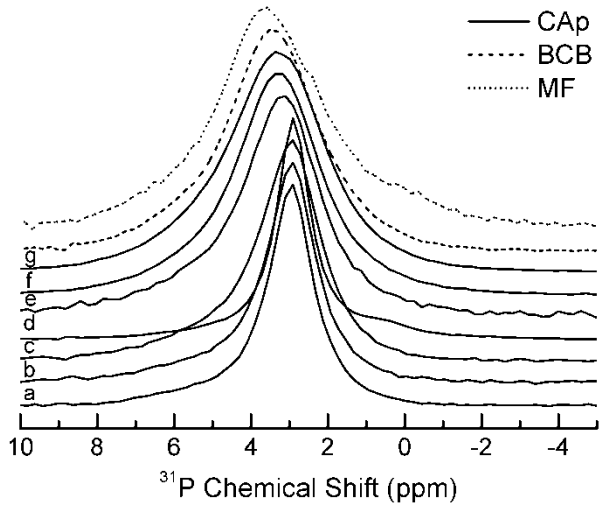

Figure 6.1 ^{31}P NMR spectra of apatites containing different carbonate weight percentages (a: 0.26 %, b: 2.3 %, c:3.3 %, d:5.5 %, e: 6.8 %, f: 8.5%, g: 10.3%), bovine cortical bone (BCB), and mouse femur (MF) samples. The spectra were recorded under MAS conditions at 10 kHz. Band heights were normalized.

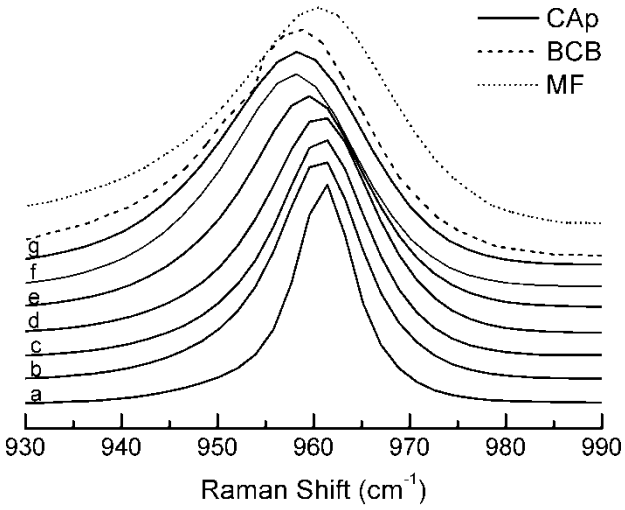

Figure 6.2 Raman spectra of apatites containing different carbonate weight percentages (a: 0.26%, b: 2.3%, c:3.3%, d:5.5%, e: 6.8%, f: 8.5%, g: 10.3%), bovine cortical bone (BCB), and mouse femur (MF) samples. Band heights were normalized.

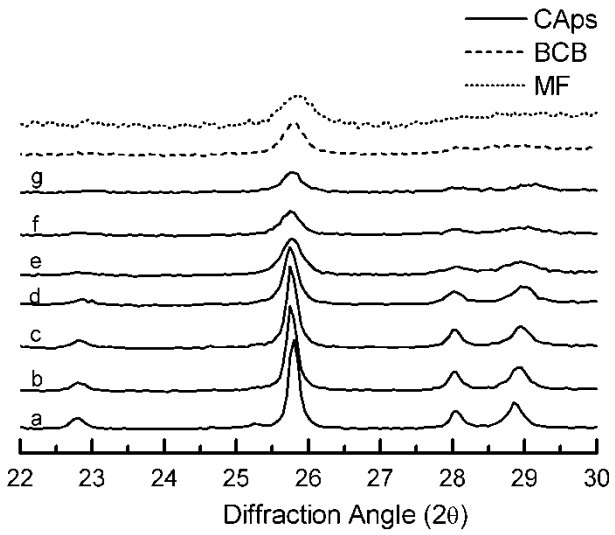

Figure 6.3 XRD diffraction pattern of apatites containing different carbonate weight percentages (a: 0.26%, b: 2.3%, c:3.3%, d:5.5%, e: 6.8%, f: 8.5%, g: 10.3%), bovine cortical bone (BCB), and mouse femur (MF).

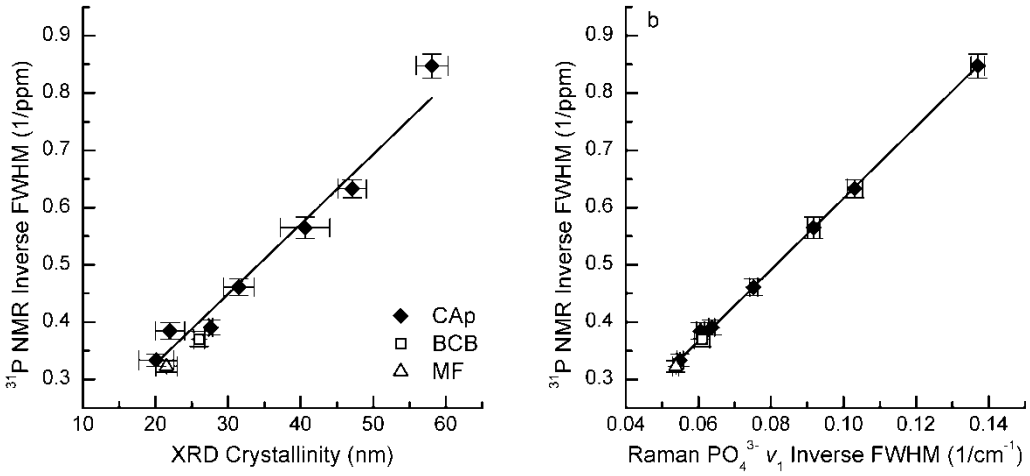

Figure 6.4 ^{31}P NMR inverse bandwidth measurements (FWHM) of synthetic carbonated apatites (0.26–10.3 wt% CO_3^{2-}), bovine cortical bone, and mouse femur compared to (a) crystallinity by x-ray diffraction, and (b) Raman PO_4^{3-} v_1 inverse bandwidth. X-Y Error bars represent standard deviations of repeated measures (XRD, n=3; NMR, n=3, Raman, n=10).

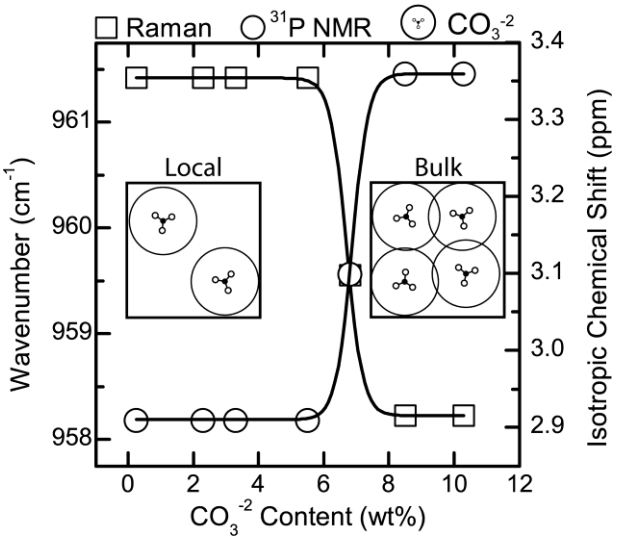

Figure 6.5 Dual y-y plot of Raman PO_4^{3-} ν_1 wavenumber shift and ^{31}P NMR isotropic chemical shift of mineral phosphate bands from synthetic carbonated apatites (0.26–10.3 wt% CO_3^{2-}). Inset illustrates the arrangement of distortions occurring in the crystal lattice due to carbonate substitution.

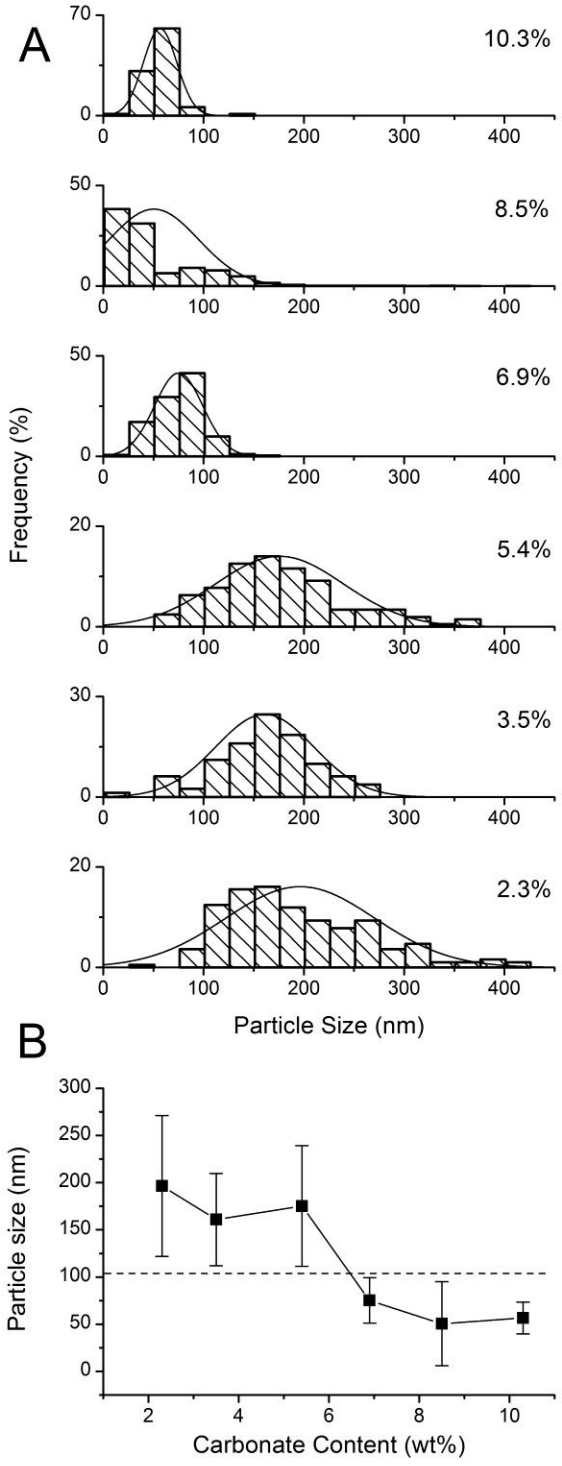

Figure 6.6 Particle sizing of synthetic apatites by atomic force microscopy. A) Histogram plots of long-axis particle sizes, B) Plot of mean particle size vs. carbonate substitution. Y-axis bars represent distribution width at half max.

References

1. Robey PG (2008) Noncollagenous Bone Matrix Proteins. In: Bilezikian JP, Raisz LG, Martin TJ (eds) Principles of Bone Biology. Academic Press, Burlington, p 335-350

2. Robey PG, Boskey AL (2008) The Composition of Bone. In: Rosen CJ (ed) Primer on the Metabolic Bone Diseases and Disorders of Mineral Metabolism. The American Society for Bone and Mineral Research, Washington D.C.

3. LeGeros RZ (1994) Biological and Synthetic Apatites. In: Brown PW, Constantz B (eds) Hydroxyapatite and Related Materials. CRC Press, Boca Raton, p 3-28

4. Lowenstam HA, Weiner S (1989) On Biomineralization. Oxford University Press, Inc., New York

5. Abjornson C, Lane JM (2006) Demineralized bone matrix and synthetic bone graft substitutes. In: Friedlaender GE, Mankin HJ, Goldberg VM (eds) Bone Grafts and Bone Graft Substitutes. American Academy of Orthopaedic Surgeons, Rosemont, IL, p 9-20

6. Finkemeier CG (2002) Bone-grafting and bone-graft substitutes. J Bone Joint Surg Am 84:454-464

7. Bigi A, Panzavolta S, Rubini k (2004) Setting mechanism of a biomimetic bone cement. Chem Mater 16:3740-3745

8. Kannan S, Lemos AF, Ferreira JMF (2006) Synthesis and mechanical performance of biological-like hydroxyapatites. Chem Mater 18:2181-2186

9. Fleet ME, Liu X (2005) Local structure of channel ions in carbonate apatite. Biomaterials 26:7548-7554

10. Eppell SJ, Tong W, Katz JL, Kuhn L, Glimcher MJ (2001) Shape and size of isolated bone mineralites measured using atomic force microscopy. J Orthop Res 19:1027-1034

11. Faibish D, Ott SM, Boskey AL (2006) Mineral changes in osteoporosis: a review. Clin Orthop Relat Res 443:28-38

12. Felsenberg D, Boonen S (2005) The bone quality framework: determinants of bone strength and their interrelationships, and implications for osteoporosis management. Clin Ther 27:1-11

13. Chatterji S, Wall JC, Jeffery JW (1981) Age-related changes in the orientation and particle size of the mineral phase in human femoral cortical bone. Calcif Tissue Int 33:567-574

14. Hanschin RG, Stern WB (1995) X-ray diffraction studies on the lattice perfection of human bone apatite (Crista iliaca). Bone 16:355S-363S

15. Boskey AL, DiCarlo E, Paschalis E, West P, Mendelsohn R (2005) Comparison of mineral quality and quantity in iliac crest biopsies from high- and low-turnover osteoporosis: an FT-IR microspectroscopic investigation. Osteoporos Int 16:2031-2038

16. Mendelsohn R, Paschalis EP, Sherman PJ, Boskey AL (2000) IR mocroscopic imaging of pathological states and fracture healing of bone. Appl Spectrosc 54:1183-1191

17. Paschalis EP, Betts F, DiCarlo E, Mendelsohn R, Boskey AL (1997) FTIR microspectroscopic analysis of human iliac crest biopsies from untreated osteoporotic bone. Calcif Tissue Int 61:487-492

18. Pleshko N, Boskey A, Mendelsohn R (1991) Novel infrared spectroscopic method for the determination of crystallinity of hydroxyapatite minerals. Biophys J 60:786-793

19. Baig AA, Fox JL, Young RA, Wang Z, Hsu J, Higuchi WI, Chhettry A, Zhuang H, Otsuka M (1999) Relationships among carbonated apatite solubility, crystallite size, and microstrain parameters. Calcif Tissue Int 64:437-449

20. Akkus O, Adar F, Schaffler MB (2004) Age-related changes in physicochemical properties of mineral crystals are related to impaired mechanical function of cortical bone. Bone 34:443-453

21. Akkus O, Polyakova-Akkus A, Adar F, Schaffler MB (2003) Aging of microstructural compartments in human compact bone. J Bone Miner Res 18:1012-1019

22. Yerramshetty JS, Lind C, Akkus O (2006) The compositional and physicochemical homogeneity of male femoral cortex increases after the sixth decade. Bone 39:1236-1243

23. Kazanci M, Fratzl P, Klaushofer K, Paschalis EP (2006) Complementary Information on In Vitro Conversion of Amorphous (Precursor) Calcium Phosphate to Hydroxyapatite from Raman Microspectroscopy and Wide-Angle X-Ray Scattering. Calcif Tissue Int V79:354-359

24. Kaflak-Hachulska A, Chmielewski D, Gorecki A, Slosarczyk A, Kolodziejski W (2006) Efficiency of 1H --> 31P NMR cross-polarization in bone apatite and its mineral standards. Solid State Nucl Magn Reson 29:345-348

25. Kaflak-Hachulska A, Samoson A, Kolodziejski W (2003) 1H MAS and 1H --> 31P CP/MAS NMR Study of Human Bone Mineral. Calcif Tissue Int 73:476-486

26. Kolodziejski W (2005) Solid-State NMR Studies of Bone. In: Klinowski J (ed) New Techniques in Solid-State NMR. Springer Berlin / Heidelberg, p 235-270

27. Aliev AE (2005) Solid-state NMR studies of collagen-based parchments and gelatin. Biopolymers 77:230-245

28. Saito H, Yokoi M (1992) A 13C NMR study on collagens in the solid state: hydration/dehydration-induced conformational change of collagen and detection of internal motions. J Biochem 111:376-382

29. Wilson EE, Awonusi A, Morris MD, Kohn DH, Tecklenburg MM, Beck LW (2006) Three structural roles for water in bone observed by solid-state NMR. Biophys J 90:3722-3731

30. Zhu P, Xu J, Sahar N, Morris MD, Kohn DH, Ramamoorthy A (2009) Time-resolved dehydration-induced structural changes in an intact bovine cortical bone revealed by solid-state NMR spectroscopy. J Am Chem Soc 131:17064-17065

31. Xu J, Zhu P, Morris MD, Ramamoorthy A (2011) Solid-State NMR Spectroscopy Provides Atomic-Level Insights Into the Dehydration of Cartilage. J Phys Chem B 115:9948-9954

32. Aue WP, Roufosse AH, Glimcher MJ, Griffin RG (1984) Solid-state phosphorus-31 nuclear magnetic resonance studies of synthetic solid phases of calcium phosphate: potential models of bone mineral. Biochemistry 23:6110-6114

33. Cho G, Wu Y, Ackerman JL (2003) Detection of hydroxyl ions in bone mineral by solid-state NMR spectroscopy. Science 300:1123-1127

34. Wu Y, Ackerman JL, Kim HM, Rey C, Barroug A, Glimcher MJ (2002) Nuclear magnetic resonance spin-spin relaxation of the crystals of bone, dental enamel, and synthetic hydroxyapatites. J Bone Miner Res 17:472-480

35. Xu J, Zhu P, Gan Z, Sahar N, Tecklenburg M, Morris MD, Kohn DH, Ramamoorthy A (2010) Natural-abundance 43Ca solid-state NMR spectroscopy of bone. J Am Chem Soc 132:11504-11509

36. Kuhn LT, Grynpas MD, Rey CC, Wu Y, Ackerman JL, Glimcher MJ (2008) A comparison of the physical and chemical differences between cancellous and cortical bovine bone mineral at two ages. Calcif Tissue Int 83:146-154

37. Asano A, Tanaka C, Murata Y (2007) NMR determination of crystallinity for poly(3-L-lysine). Polymer 48:3809-3816

38. Zhang L, Hansen EW, Helland I, Hinrichsed E, Roots ALJ (2009) Crystallinity in Ethene-1-Hexene Copolymers Determined by 1H and 13C NMR. A Comparative Study. Macromolecule 42:5189-5195

39. Tsuji H, Kamo S, Horrii F (2010) Solid-state C-13 NMR analyses of the structures of crystallized and quenched poly(lactide)s: Effects of crystallinity, water absorption, hydrolytic degradation, and tacticity. Polymer 51:2215-2220

40. Tong W, Glimcher MJ, Katz JL, Kuhn L, Eppell SJ (2003) Size and shape of mineralites in young bovine bone measured by atomic force microscopy. Calcif Tissue Int 72:592-598

41. Wallace JM, Erickson B, Les CM, Orr BG, Banaszak Holl MM (2010) Distribution of type I collagen morphologies in bone: relation to estrogen depletion. Bone 46:1349-1354

42. Wallace JM, Chen Q, Fang M, Erickson B, Orr BG, Banaszak Holl MM (2010) Type I collagen exists as a distribution of nanoscale morphologies in teeth, bones, and tendons. Langmuir 26:7349-7354

43. Penel G, Leroy G, Rey C, Bres E (1998) MicroRaman Spectral Study of the PO4 and CO3 Vibrational Modes in Synthetic and Biological Apatites. Calcif Tissue Int V63:475-481

44. Termine JD, Eanes ED, Greenfield DJ, Nylen MU, Harper RA (1973) Hydrazine-deproteinated bone mineral. Calcif Tissue Int 12:73-90

45. Featherstone JD, Pearson S, LeGeros RZ (1984) An infrared method for quantification of carbonate in carbonated apatites. Caries Res 18:63-66

46. McElderry JD, Kole MR, Morris MD (2011) Repeated freeze-thawing of bone tissue affects Raman bone quality measurements. J Biomed Opt 16:071407

47. Crane NJ, Popescu V, Morris MD, Steenhuis P, Ignelzi JMA (2006) Raman spectroscopic evidence for octacalcium phosphate and other transient mineral species deposited during intramembranous mineralization. Bone 39:434-442

48. Tarnowski CP, Ignelzi MA, Jr., Morris MD (2002) Mineralization of developing mouse calvaria as revealed by Raman microspectroscopy. J Bone Miner Res 17:1118-1126

49. Boskey AL, Coleman R (2010) Aging and bone. J Dent Res 89:1333-1348

CHAPTER VII

REPEATED FREEZE-THAWING OF BONE TISSUE AFFECTS RAMAN BONE QUALITY MEASUREMENTS

1 Introduction

The preservation of bone tissue for Raman spectroscopic analysis is essential for maintaining physical and material properties for continued or repeated experimentation. Fixing and embedding bone as a preservation technique has been studied for Fourier transform infrared spectroscopy[1-4] and has been widely used for Raman spectroscopy with similar success.[5, 6] However, fixing agents can alter tissue components from their native state. Ethanol denatures bone matrix proteins and dissolves lipids. Fixing bone in ethanol perturbs protein secondary structure. Formalin binds to proteins and forms cross-links which perturb the tertiary structure of proteins but has little effect on the amide bonding.[7] The addition of any fixing agent comes with added complexity in the spectral background which can be challenging to remove.

Within the last ten years it has become apparent that probing bone using Raman spectroscopy is best done on fresh or frozen tissues.[6, 8-12] Raman bone studies involving other testing where the tissue cannot be fixed often require multiple steps and specimens are therefore frozen and thawed several times. This can be problematic since little is understood about the effects of freezing and thawing on Raman bands.

Mechanical tests of frozen collagenous tissues compared to fresh tissues shows that effects can be evident after freezing.[13-17] Compressive stress tests on knee cartilage showed comparable decreases in stress for both slow frozen (-20°C) and flash frozen (-80°C) tissues.[13] Hydration tests on frozen intervertebral discs revealed increased permeability through the collagenous layers which increased the water content in the disc nucleus.[15-17] However, it was noted by Bass et al. that water content was reduced within the collagen layers after freezing despite the increased permeability.[16]

How many times can a bone be frozen before it yields erroneous spectroscopic data? It is the aim of the authors to address this question in terms of Raman microspectroscopy. By submitting cortical bone to repeated freezing and thawing, we have identified changes in key spectral features as a result of bone degradation. It is not our aim to provide a rigorous analysis of the biology of bone degradation.

2 Materials and Methods

2.1 Preparation of Mouse Femora

Six femora were harvested fresh from 20 day old male C57BL/6 mice and all soft tissue was removed. Femora were immediately attached to a glass microscope slide with the posterior side of the mid-diaphysis facing upward using glue (Instant Krazy Glue, Elmer's Products, Inc., Columbus, OH). The glue was allowed to set for more than 20 min, but no more than 30 min. Femora were then polished transversely using a range of fine polishing paper (1200, 2000, 3000 grit) by inverting the slide/femur and gently gliding the bone against the paper in a figure eight motion. Several drops of 1x Hank's balanced salt solution (HBSS) were used to lubricate the polishing surface. Femora were

polished until an optically flat and smooth region was achieved in the mid-diaphysis, which was approximately 2 mm long. A notch was made with a scalpel perpendicular to the long axis at one end of the region of interest to create a landmark for reproducible orientation under a microscope.

All experiments on tissue designated as freeze-thaw cycle 0 (FTC 0) were finished within three hours of femoral extraction and within six hours of sacrifice. Femora were individually wrapped in HBSS-soaked gauze and frozen at -23°C for at least twelve hours. Bones were then thawed at room temperature using HBSS solution for approximately 30 min before acquisition of spectra. The bones were kept moist at all times during the experiment. This process was repeated four times for each bone.

2.2 Raman Microscopy

Specimens were loaded onto the stage of a custom built Raman microscope comprising a fluorescence microscope (Eclipse ME600, Nikon Instruments Inc., Melville, NY), a 785 nm stabilized diode laser (Invictus, Kaiser Optical Systems, Inc., Ann Arbor, MI), imaging spectrograph with a 50 μm slitwidth (Holospec f/1.8i, Kaiser Optical Systems, Inc.), and deep depletion, back-illuminated CCD camera (Classic CCD, Andor Technologies, South Windsor, CT). The laser was expanded through a 20x, 0.75NA objective along one axis (100x7 μm) for line-scan imaging. Each line was averaged across the spatial axis. Twelve line spectra were acquired per specimen using 25 μm step sizes starting with the laser line parallel to the notch. Spectral integration was 90 s per step. Post-processing of spectra was performed using calibration and baselining techniques commonly practiced in the field.

2.3 Bone Metrics

Several Raman spectroscopic parameters were used to assess the changes in the matrix component of cortical bone such as the normalized height of amide I (1664 cm^{-1}/959 cm^{-1}), amide III (1270 cm^{-1}/959 cm^{-1}), proline and hydroxyproline ([853 cm^{-1}+876 cm^{-1}]/959 cm^{-1}), and the CH_2 scissor mode (1450 cm^{-1}/959 cm^{-1}). Mineral parameters such as crystallinity (959 cm^{-1} inverse FWHM) and carbonate content (1070 cm^{-1}/959 cm^{-1} height ratio) were also used. Weak matrix bands at 924 and 943 cm^{-1} were digitally resolved from the phosphate band using the Marquardt non-linear curve fitting algorithm.[18] The carbonate band was digitally resolved using the curve fitting technique which was described by Awonusi et al.[19] A repeated-measures one-way ANOVA with *post-hoc* analysis was performed to assess changes in each metric. Within-group significance was measured using Greenhouse-Geisser probabilities. Pairwise significance was measured only between the FTC 0 group and subsequent FTC group using Bonferonni corrected probabilities. All statistical analysis was done using SPSS.

3 Results

After repeated freezing and thawing, the femora were visibly degraded. The notch made in the tissue for orientation purposes became less distinct and the surface became less smooth as evidenced by a reduction of focus. Small bits of soft tissue were found adhered to the gauze after later FTCs. In spite of the noticeable physical degradations, Raman spectra were consistently obtained in a reproducible location through all FTCs. It was difficult to acquire spectra beyond FTC 4 due to the loss of focus and orientation.

Repeated freezing and thawing of the femora induced significant changes in the amide bands as shown in Figure 7.1. The amide I band height ($p = 0.01$, within FTC groups) had an overall decrease of 21%. Pairwise differences were significant after only two FTCs and trended toward significance after one FTC. The amide III band height ($p = 0.03$, within FTC groups) decreased 11% with significant pairwise differences after three FTCs and a trend toward significance in FTC groups 1 and 2. The pro/hyp band combination and the CH_2 scissoring band did not change significantly from the unfrozen tissue.

Mineral parameters were also investigated for degradation through freezing and thawing and are shown in Figure 7.2. Crystallinity values were consistent between mice as evidenced by small variances (~1% RSD) within each group. Crystallinity did change significantly ($p = 0.003$, within FTC groups), decreasing by 4%. Declining values of the crystallinity parameter were measured after only one FTC and more notably after three and four FTCs in pairwise comparisons with the FTC 0 group. Mineral carbonate substitution did not show significant change after four FTCs. Positions of the phosphate and carbonate bands did not fluctuate by more than half a wavenumber.

4 Discussion

Degradation of the tissue was evident in Raman spectra which show changes in both mineral and matrix bands with the most pronounced changes in the amide band heights. Band area ratios were also measured for the amide bands and found to be consistent with the decreases shown in Figure 7.1. It is unclear whether these spectroscopic changes are indicative of actual matrix removal from the cortical bone or

simply changes in the optical properties of the tissue. However, the changes in the matrix due to freezing and thawing seemed to affect the amide bands more than other matrix bands. The similarity in trend between the amide I and amide III bands suggests degradation of the protein secondary structure or denaturation. There were no pronounced changes in the pro/hyp bands that would indicate loss of collagen in the bone matrix.

Mineral measurements revealed declining crystallinity while carbonate content remained unchanged. The precision of the two measurements differed substantially. The 1020–1080 cm^{-1} region is complicated with several phosphate peaks (ν_3) of comparable height which carbonate overlaps. Fitting multiple components decreases the accuracy of curve-fit estimates. A power analysis ($\alpha = .95$, $\beta = .8$) of the pooled standard deviations revealed that changes in carbonate levels of >13% could be detected. By the same analysis, crystallinity was found to be much more sensitive as it was capable of detecting >2% changes. The 900–990 cm^{-1} region could be consistently fit to three components, shown in Figure 7.3, across the region of cortical bone. This fit can be reproduced in mature wild type mouse cortical bone. Not accounting for the matrix bands at 924 and 943 cm^{-1} results in a 10% overestimation of the band width. This means that changes in phosphate band width could be detected down to <1 cm^{-1} on a spectrograph with 6 cm^{-1} resolution. It is clear that any changes occurring to the mineral due to freezing and thawing are small and below the detection limits of current carbonate-to-phosphate measurements.

The crystallinity parameter is an estimate of crystal size along the c-axis but can be influenced by several confounding factors. Ionic substitution by carbonate or other ions lowers crystal perfection which is reflected in lower crystallinity values. The

molecular environment at the mineral surface can either induce or prevent ordering of surface ions into a stable apatitic form. Lastly, randomization of crystal orientation is capable of decreasing the apparent crystallinity. Therefore, crystallinity should be thought of as a lower limit to the crystal size. This study is incapable of distinguishing which factor is responsible for the apparent decrease in crystallinity values. However, the release of mineral from denatured matrix proteins may be sufficient to lower crystallinity values either by randomization of crystal orientation or by destabilization of surface ions.

Freezing and thawing bone multiple times results in spectral artifacts similar to fixation but to a lesser extent. Pleshko et al. measured FTIR spectra of bone fixed in ethanol and formalin showing that ethanol led to artifacts in the amide region while formalin slightly altered mineral crystallinity.[2] Although freezing and thawing displayed alterations in both the amide and mineral bands, they were only sizeable after several cycles. Therefore, for best results it is recommended that Raman spectroscopy studies of bone be limited to one freezing and thawing.

5 Conclusion

Degradation of bone tissue after repeated freezing and thawing had a significant impact on both matrix and mineral spectroscopic features and may interfere with bone quality measurements as early as one freezing.

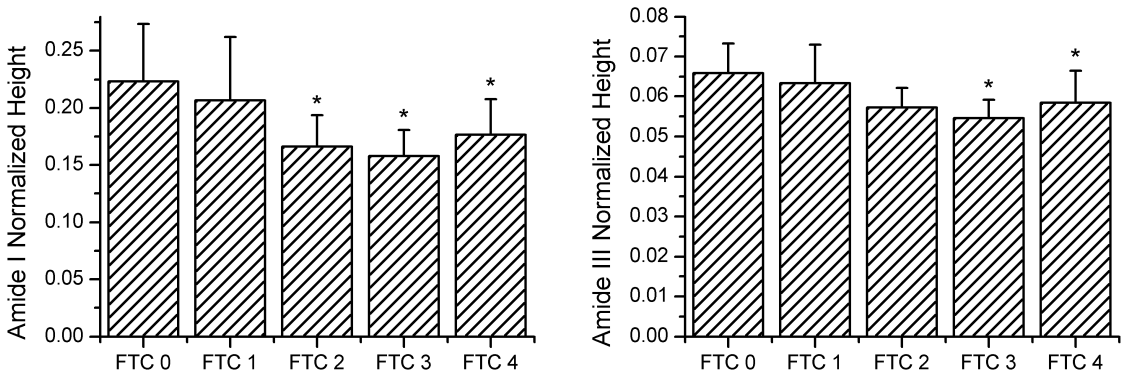

Figure 7.1 Raman measurements of the Amide I and Amide III band heights on cortical bone. Changes in band heights were first evident in Amide I after FTC 2, and then in Amide III after FTC 3. The FTC 1 group may also be indicative of subtle changes in the bone as it deteriorates. Asterisks are indicative of a Bonferonni pairwise difference from FTC 0 with significance of $p < 0.05$.

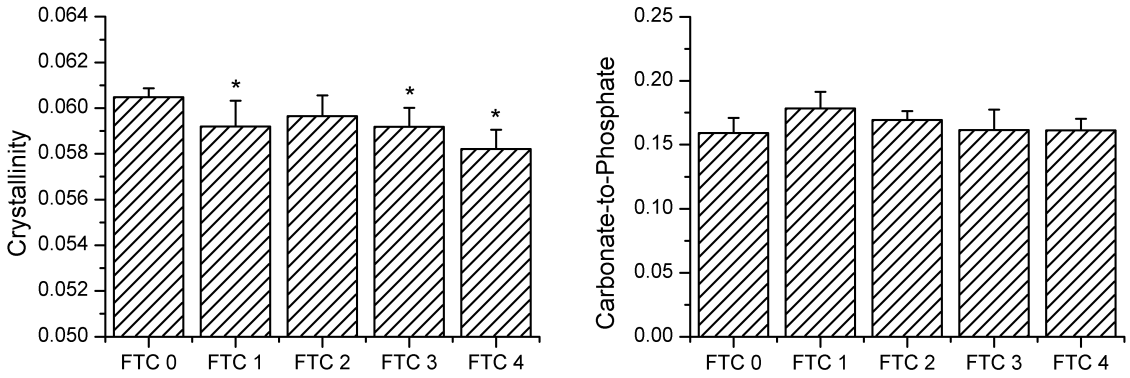

Figure 7.2 Crystallinity and carbonate-to-phosphate Raman measurements on cortical bone. Crystallinity showed decreased levels after one FTC and further decline after subsequent freezing and thawing while carbonate levels did not vary significantly. Asterisks are indicative of a Bonferonni pairwise difference from FTC 0 with significance of $p < 0.05$.

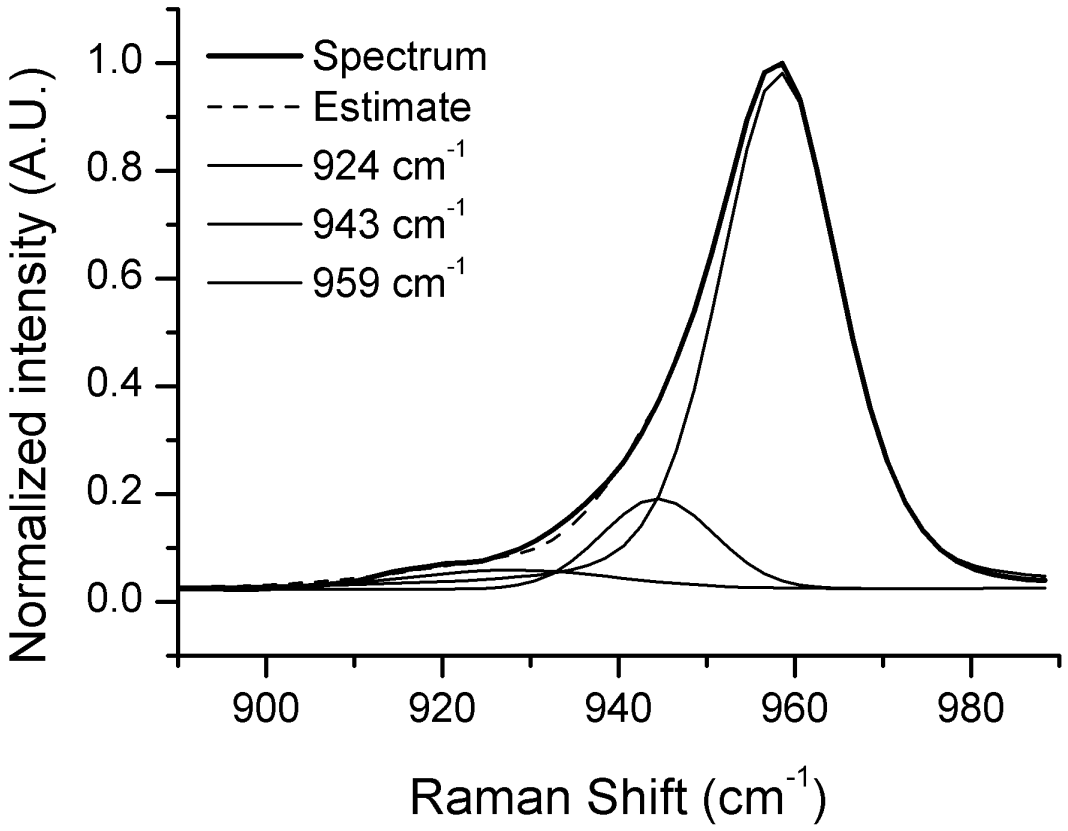

Figure 7.3 Non-linear curve fitting results for the 882–982 cm^{-1} region. Three Gaussian/Lorentzian functions were used to represent the phosphate 959 cm^{-1} band and two matrix bands at 943 cm^{-1} and 924 cm^{-1}. Region was truncated to not include the phenylalanine band at 1002 cm^{-1} and the proline and hydroxyproline bands at 853 cm^{-1} and 876 cm^{-1}. Fitting the band reveals the true symmetry of the underlying phosphate peak.

References

1. Boskey AL, Cohen ML, Bullough PG (1982) hard tissue biochemistry: a comparison of fresh-frozen and formalin-fixed tissue samples. Calcif Tissue Int 34:328-331

2. Pleshko NL, Boskey AL, Mendelsohn R (1992) An FT-IR microscopic investigation of the effects of tissue preservation on bone. Calcif Tissue Int 51:72-77

3. Pleshko NL, Boskey AL, Mendelsohn R (1992) An infrared study of the interaction of polymethyl methacrylate with the protein and mineral components of bone. J Histochem Cytochem 40:1413-1417

4. Aparicio S, Doty SB, Camacho NP, Paschalis EP, Spevak L, Mendelsohn R, Boskey AL (2002) Optimal methods for processing mineralized tissues for Fourier transform infrared microspectroscopy. Calcif Tissue Int 70:422-429

5. Yeni YN, Yerramshetty J, Akkus O, Pechey C, Les CM (2006) Effect of fixation and embedding on Raman spectroscopic analysis of bone tissue. Calcif Tissue Int 78:363-371

6. Carden A, Morris MD (2000) Application of vibrational spectroscopy to the study of mineralized tissues (review). J Biomed Opt 5:259-268

7. Scarano A, Iezzi G, Piattelli A (2003) Common fixatives In Hard-Tissue Histology. In: An YH, Martin KL (eds) handbook of Histology Methods for Bone and Cartilage. Humana Press, New Jersey

8. Dooley KA, McCormack J, Fyhrie DP, Morris MD (2009) Stress mapping of undamaged, strained, and failed regions of bone using Raman spectroscopy. J Biomed Opt 14:044018

9. Schulmerich MV, Cole JH, Dooley KA, Morris MD, Kreider JM, Goldstein SA, Srinivasan S, Pogue BW (2008) Noninvasive Raman tomographic imaging of canine bone tissue. J Biomed Opt 13:020506

10. Schulmerich MV, Dooley KA, Morris MD, Vanasse TM, Goldstein SA (2006) Transcutaneous fiber optic Raman spectroscopy of bone using annular illumination and a circular array of collection fibers. J Biomed Opt 11:060502

11. Ager JW, Nalla RK, Breeden KL, Ritchie RO (2005) Deep-ultraviolet Raman spectroscopy study of the effect of aging on human cortical bone. J Biomed Opt 10:034012

12. Morris MD, Matousek P, Towrie M, Parker AW, Goodship AE, Draper ER (2005) Kerr-gated time-resolved Raman spectroscopy of equine cortical bone tissue. J Biomed Opt 10:14014

13. Kennedy EA, Tordonado DS, Duma SM (2007) Effects of freezing on the mechanical properties of articular cartilage. Biomed Sci Instrum 43:342-347

14. Lewis PB, Williams JM, Hallab N, Virdi A, Yanke A, Cole BJ (2008) Multiple freeze-thaw cycled meniscal allograft tissue: A biomechanical, biochemical, and histologic analysis. J Orthop Res 26:49-55

15. Hongo M, Gay RE, Hsu JT, Zhao KD, Ilharreborde B, Berglund LJ, An KN (2008) Effect of multiple freeze-thaw cycles on intervertebral dynamic motion characteristics in the porcine lumbar spine. J Biomech 41:916-920

16. Bass EC, Duncan NA, Hariharan JS, Dusick J, Bueff HU, Lotz JC (1997) Frozen storage affects the compressive creep behavior of the porcine intervertebral disc. Spine (Phila Pa 1976) 22:2867-2876

17. Johnstone B, Urban JP, Roberts S, Menage J (1992) The fluid content of the human intervertebral disc. Comparison between fluid content and swelling pressure profiles of discs removed at surgery and those taken postmortem. Spine (Phila Pa 1976) 17:412-416

18. Press WH, Teukolsky SA, Vetterling WT, Flannery BP (1992) Numerical Recipes in C. Cambridge University Press, New York

19. Awonusi A, Morris M, Tecklenburg M (2007) Carbonate Assignment and Calibration in the Raman Spectrum of Apatite. Calcified Tissue International 81:46-52

CHAPTER VIII
CONCLUSION: A KINETIC VIEW OF MINERAL NUCLEATION AND GROWTH

Mammalian bone mineral plays a key role in skeletal physiology. The amount, size and crystal structure of the mineral have a significant impact on bone strength and calcium homeostasis. This thesis explores the dynamic nature of mineral during the formation process. Based on the studies herein, it is concluded that bone mineral formation is sensitive to a combination of chemical and biological factors that mediate the properties of the solid-state. Mineral deposition is mediated by the circadian clock which induces near-24-hour bursts of mineral deposition during neonatal bone development. The rate of mineral deposition reaches a maximum in the early evening. When compared to the timed expression of components to the molecular clock, mineral appears to be most closely associated with maximum *Clock*:*Bmal* transcriptional activity. A link between *Clock:Bmal* and mineralizing proteins has not been established previously. This is an exciting direction for future research considering the importance of understanding anabolic pathways of bone formation in pharmaceutical agent discovery.

Downstream from the *Clock:Bmal* transcription factor, non-collagenous proteins (NCPs) in the extracellular matrix nucleate solid mineral which proceeds rapidly into a small apatitic crystal form. However, when the nucleation step is enhanced through BSP overexpression, mineral is deposited as an amorphous solid phase that is gradually hydrated as part of a crystallization process. This crystallization pathway is hypothesized

to be inhibited by other NCPs in native mineralization conditions. Continuation of this work may include both overexpression and knock-out models of other known nucleator and inhibitor NCPs. These studies may reveal other unique mineralization pathways from which NCP function can be inferred. However, to identify the true function of NCPs in the mineralization process minimum perturbation of the native conditions may be necessary.

After the nucleation step in the mineralization process, small crystallites increase in length until a certain size is achieved. The growth phase occurs in a linear fashion over several days. This step appears to be independent of the circadian pathway displaying no observable periodic changes. Crystal sizes in both developing and fracture healing bone mineral do not exceed 23 nm in length. Disruption of collagen, as in the case of Brtl/+ mice, significantly delays mineral growth but does not alter this crystal size limit. Study of synthetic apatites in a protein-free environment reveals a crystal-size dependency on carbonate content. Therefore, the crystal growth step in mineralization may not be dependent on direct protein interaction, as is the case with the nucleation step.

Raman probes for *in situ* monitoring of mineral kinetics are capable of crystal characterization with minute temporal resolution. The main limitations to this technique stem from the inability to detect trace components that are important to the mineralization process. The Raman spectra of NCPs are not sufficiently different from collagen to selectively follow their expression *in situ*. Biochemical techniques such as real-time PCR, fluorescence vital stains, and bioluminescence gene targeting can be useful for selectively measuring protein expression. Furthermore, mineralization kinetics in endochondral ossification, which occurs in long bones, is problematic due to the presence of previously

formed mineral throughout the tissue. For this reason the experiments in this thesis have been mainly restricted to intramembranous ossification in the calvarial fontanel region. However, the extraction and culture of growth plates from long bones may provide an adequate growth model for establishing mineral kinetics in endochondral ossification. Lastly, Raman spectroscopy cannot provide an adequate view of protein-mineral binding. However, these interactions are currently being explored using techniques in solid-state NMR that are sensitive to through-space dipolar couplings between the mineral surface and protein residue side chains.

APPENDICES

APPENDIX I

COPYRIGHT PERMISSION

jdmac jdmac <jdmac@umich.edu>

JBO Reprint Permission

Scott McNeill <scottm@spie.org> Fri, Dec 2, 2011 at 12:09 PM
To: John-David McElderry <jdmac@umich.edu>

Dear John-David McElderry,

Thank you for seeking permission from SPIE to reprint material from our publications. As an author of the cited work, you retain co-owner rights to the original content therein. Publisher's permission is hereby granted under the following conditions: (1) the material to be used has appeared in our publication without credit or acknowledgment to another source; and (2) you credit the original SPIE publication. Include the authors' names, title of paper, volume title, SPIE volume number, and year of publication in your credit statement.

Sincerely,

Scott McNeill for
Eric Pepper, Director of Publications
SPIE
P.O. Box 10, Bellingham WA 98227-0010 USA
360/676-3290 (Pacific Time) eric@spie.org
[Quoted text hidden]

McElderry J-DP, Kole MR, Morris MD (2011) Repeated freeze-thawing of bone tissue affects Raman bone quality measurements. J Biomed Optics 16:071407

APPENDIX II

OUTLINE OF INSTRUMENT AUTOMATION FOR RAMAN/FLUORESCENCE MICROSCOPE IN LABVIEW

Brief explanation of case and event structures

I. Initialize variables (Fig. A3 no. 11)

II. Main Program Loop (Fig. A3 no. 12)

A. Case 0 Data acquisition loop actions Fig. A3, no. 13)

1. Case0 empty

2. Case1 activate stage movement in "II. B. Case1, 2. Stage Controls" (Fig. A3 no. 14)

3. Case2 Activate iDus

4. Case3 Activate iXon

5. Case4 Loop indexing and bookkeeping (Fig. A2 no. 8)

B. Case 1 Event Structures

1. Joystick safety limit switch (Fig. A4 no. 15)

2. Stage Controls (Fig. A2 no. 9, Fig. A4 no. 16)

3. Coordinate interface controls (Fig. A2 no. 9, Fig. A4 no. 17)

4. Shutter Controls (Fig. A2 no. 7, Fig. A4 no. 18)

5. Scrollbar Controls (Fig. A2 no. 9, Fig. A4 no. 19)

C. Case 2

1. Data acquisition loop delay (Fig. A2 no. 8&9)
2. Activate/deactivate buttons during loop
3. Scrollbar event for iDus image(Fig. A1 no. 2)

D. Case3 Switch to iDus handle

E. Case4 iDus Controls (Fig. A1 no. 4, Fig. A4 no. 20)

1. Event0 Report status/retrieve image (Fig. A1 no. 2)
2. Event1 Initialize iDus (Fig. A1 no. 6)
3. Event2 Temperature controls
4. Event3 Set-up acquisition
5. Event4 Exposure time controls
6. Event5 Acquire image
7. Event6 Acquire video
8. Event7 Abort controls
9. Event8 Initialize shutdown sequence

F. Case5 Save iDus data to ascii

G. Case6 Switch to iXon handle

H. Case7 Load dark file for iXon

I. Case8 iXus Controls (Fig. A1 no. 3, Fig. A4 no. 21)

1. Event0 Report status/retrieve image (Fig. A1 no. 1)
2. Event1 Initialize iXus (Fig. A1 no. 6)
3. Event2 Temperature controls
4. Event3 Set-up acquisition
5. Event4 Exposure time controls

6. Event5 Acquire image

7. Event6 Acquire video

8. Event7 Abort controls

9. Event8 Initialize shutdown sequence

J. Save iXon data to ascii

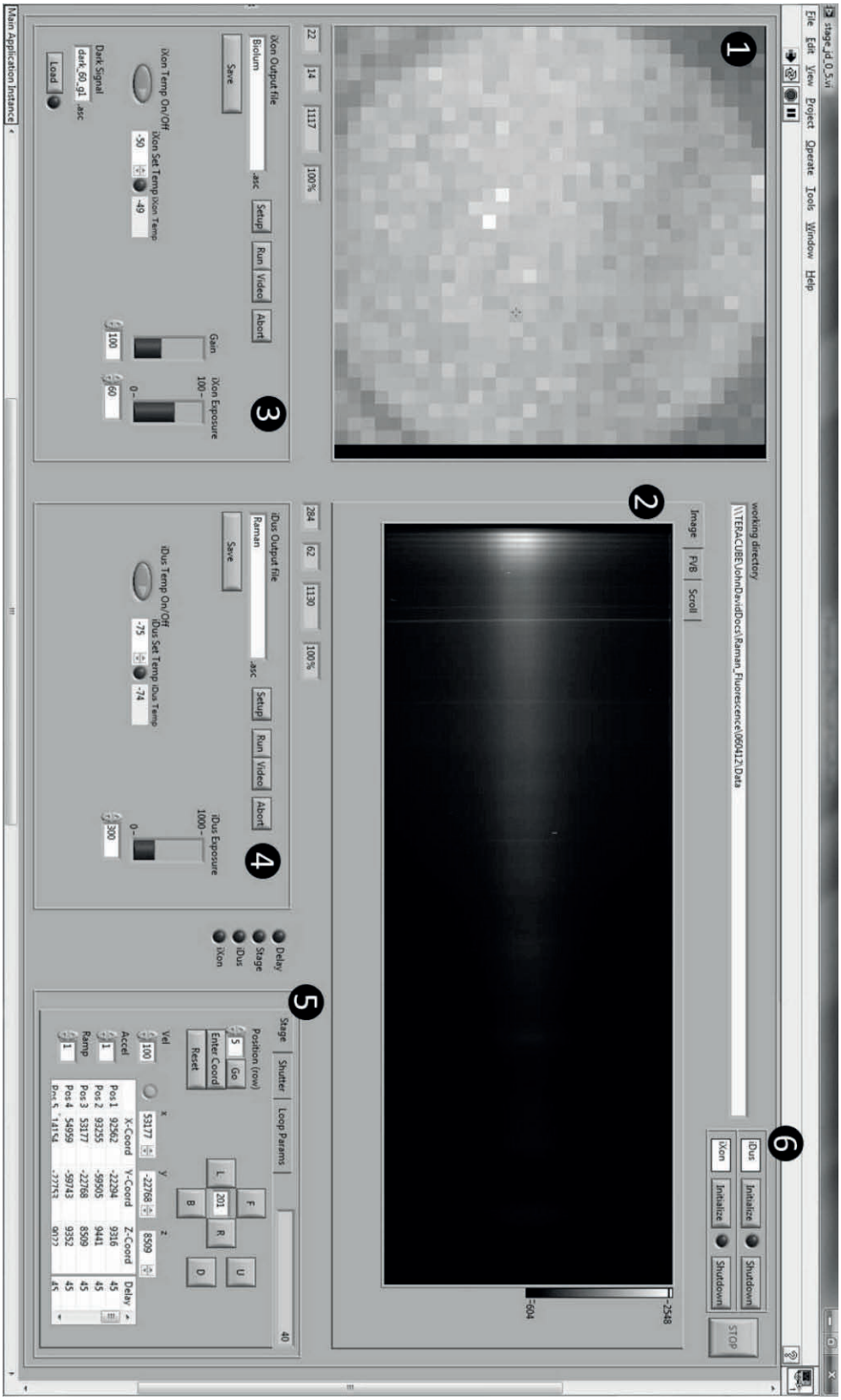

Figure A.1 Graphical User Interface

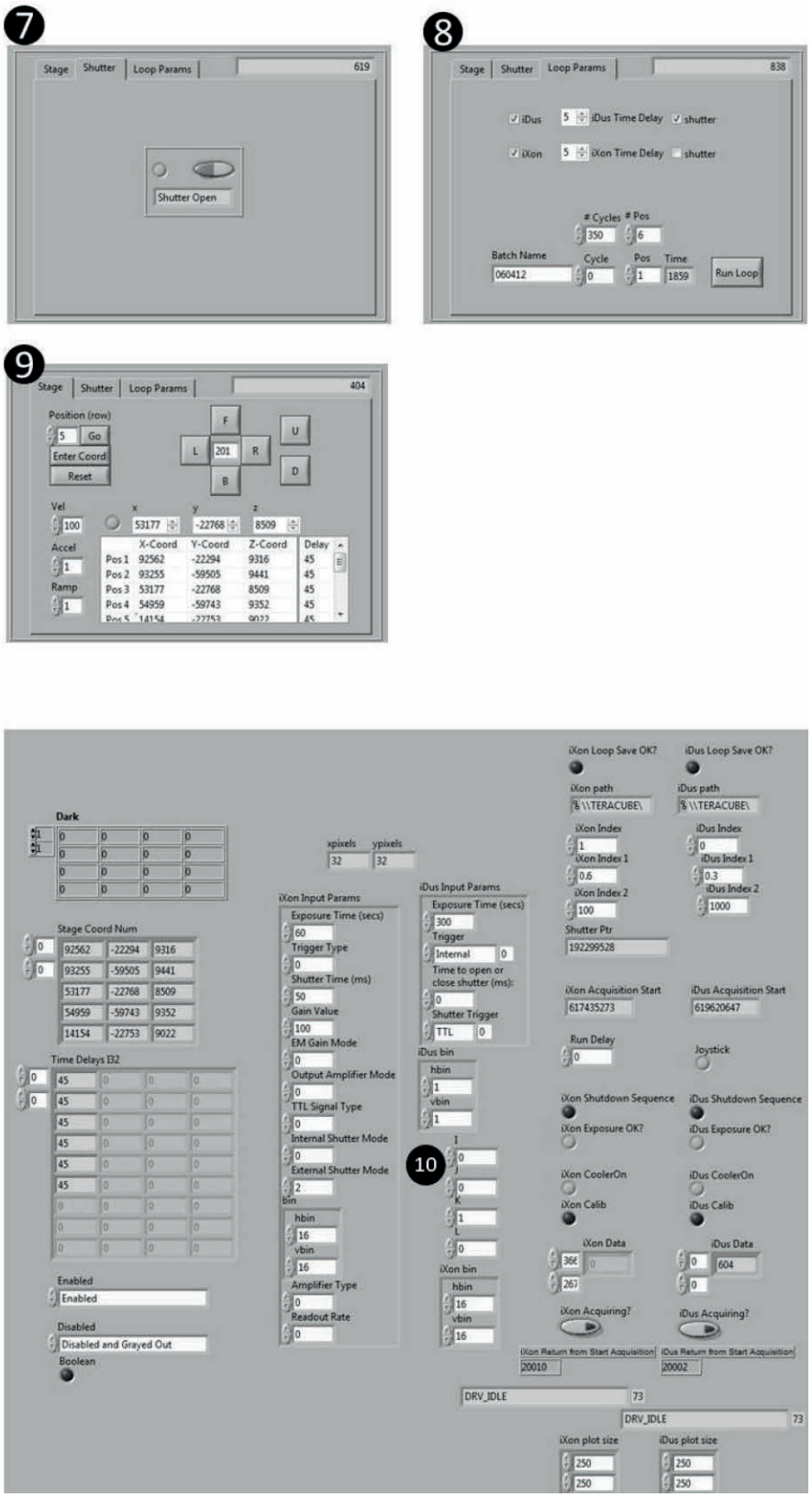

Figure A.2 Additional Folders and Buttons on GUI

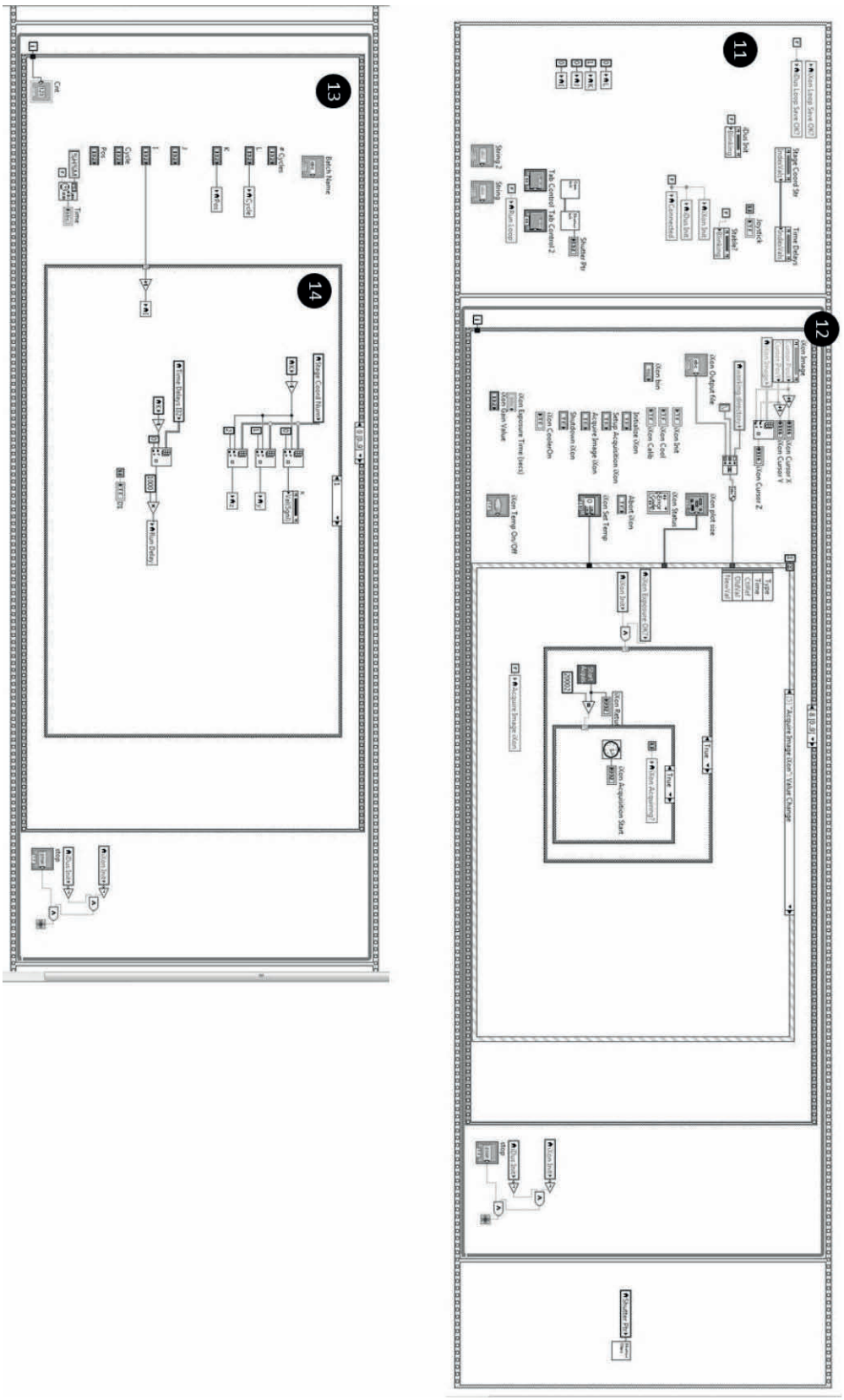

Figure A.3 Block Diagram Overview

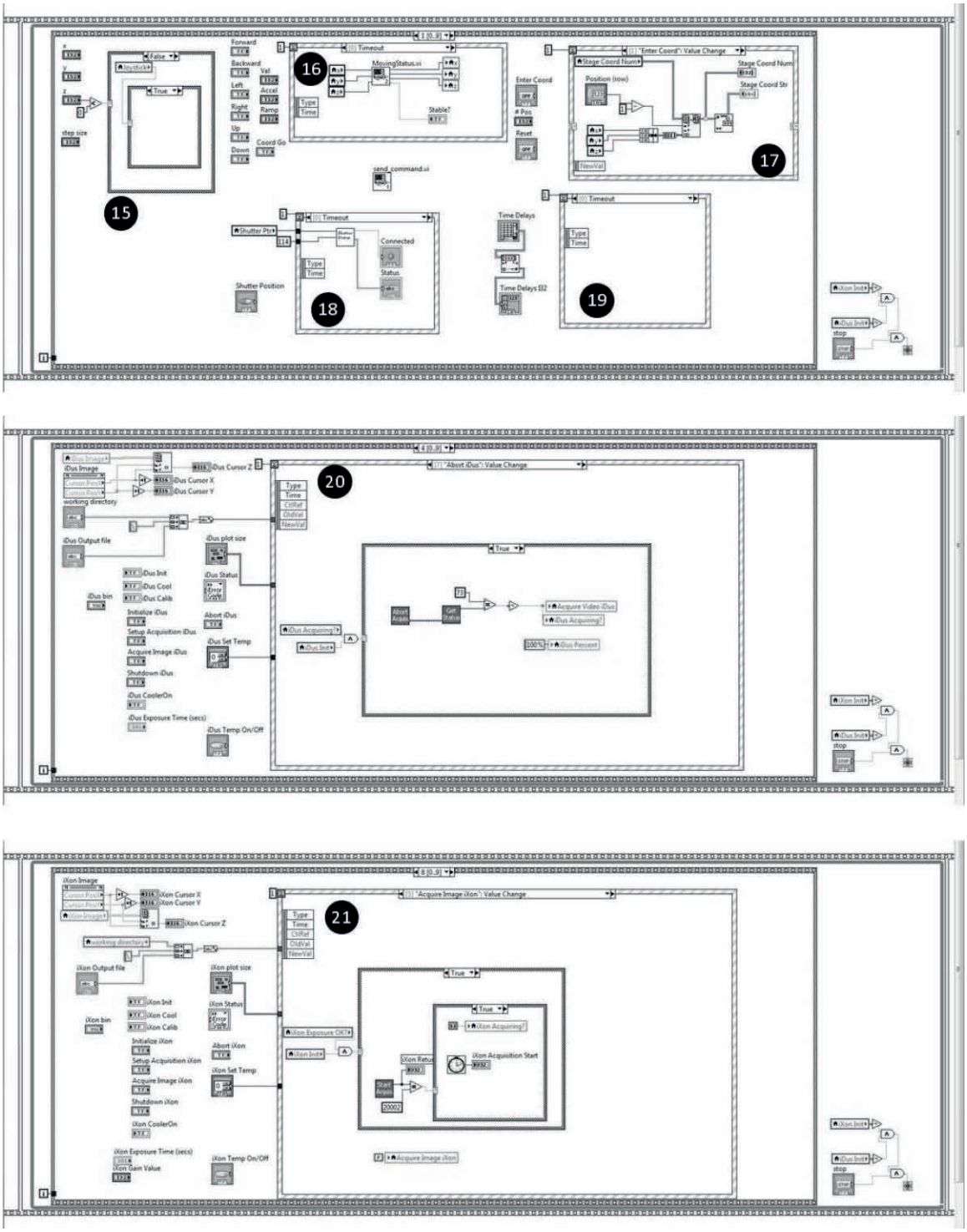

Figure A.4 Cases in the Data Loop.

APPENDIX III

MATLAB SCRIPTS FOR PROCESSING RAMAN SPECTRA

PREPROCESS.m

```
% Set-up parallel computing capabilities
matlabpool open 4

%%
% LOAD THE FILES

FileName{1} = input('Input neon filename:  ','s');
neon=francisandor([FileName{1} '.asc']);
FileName{2} = input('Input dark filename for neon:  ','s');
darkneon=francisandor([FileName{2} '.asc']);
FileName{3} = input('Input teflon filename:  ','s');
teflon=francisandor([FileName{3} '.asc']);
FileName{4} = input('Input dark filename for teflon:  ','s');
darkteflon=francisandor([FileName{4} '.asc']);
FileName{5} = input('Input white dichroic filename:  ','s');
white=francisandor([FileName{5} '.asc']);
FileName{6} = input('Input dark filename for white dichroic:  ','s');
darkwhite=francisandor([FileName{6} '.asc']);
FileName{7} = input('Input TFORM filename:  ','s');
load(FileName{7});

% Unspike all calibration files
visispike('neon');
disp('unspike neon');
pause()
visispike('darkneon');
disp('unspike darkneon');
pause()
visispike('teflon');
disp('unspike teflon');
pause()
visispike('darkteflon');
disp('unspike darkteflon');
pause()
visispike('white');
disp('unspike white');
pause()
visispike('darkwhite');
disp('unspike darkwhite');
pause()

%% CORRECT THE NEON

im_neon = imtransform(neon.', TFORM, 'bilinear');
im_darkneon = imtransform(darkneon.',TFORM,'bilinear');
im_white = imtransform(white.',TFORM,'bilinear');
% im_white = whitefilter(im_white.');
im_white = im_white.';
im_darkwhite = imtransform(darkwhite.',TFORM,'bilinear');
im_neon = (im_neon-im_darkneon);
```

```
sum_neon = sum(im_neon);

% find the neon peaks
[maxy,maxi] = findmaxima(sum_neon);

% load the known wavelength values
cal_vector = xlsread('red2_excel_calibration.xls');

% split the loaded values into wavelengths and pixels
wavelen = cal_vector(1,:);
est_pix = cal_vector(2,:);

wavelen(est_pix<5)=[];
est_pix(est_pix<5)=[];

% find the closest pixels
known_pix=nan(size(est_pix));
for i=1:numel(est_pix);
    [y,j] = min(abs(est_pix(i)-maxi));
    known_pix(i) = maxi(j);
end

% calculate the rshift coefficients
coef = wavelen/[known_pix.^3;known_pix.^2;known_pix;ones(size(known_pix))]; % coef
eventually becomes 50x4

clear neon800ms dark1 maxy maxi cal_vector wavelen est_pix known_pix

%% CORRECT THE TEFLON

im_teflon = imtransform(teflon.',TFORM,'bilinear');
im_darkteflon = imtransform(darkteflon.',TFORM,'bilinear');
im_white = imtransform(white.',TFORM,'bilinear');

% im_white = whitefilter(im_white);
im_darkwhite = imtransform(darkwhite.',TFORM,'bilinear');
whiteNIST = dlmread('090520AI.prn');
im_teflon = (im_teflon-im_darkteflon).*(im_white);
sum_teflon = sum(im_teflon);

% initial laser wavelength estimate
laser_wl=830.00;

cm2=[];
laser_wl2=[];
pos2=[];

% iteratively find a better laser wavelength
cm=rshift(1:size(sum_teflon,2),coef,laser_wl);
[interp_data,interp_axis]=FEW_interpolate(sum_teflon,cm,50);

[y,i]=max(interp_data);
pos=interp_axis(i);

oldl=nan;

while abs(pos-732)>0.01
    grandl=oldl;
    oldl=laser_wl;
    if (pos<732)
        % make laser wl bigger
        laser_wl = laser_wl - 0.005;
    else
        % make laser wl smaller
        laser_wl = laser_wl + 0.005;
    end

    if (grandl==laser_wl) % it is jittering around the same point.
        break;
    end
```

```
    % iteratively find a better laser wavelength
    cm=rshift(1:size(sum_teflon,2),coef,laser_wl);
    [interp_data,interp_axis]=FEW_interpolate(sum_teflon,cm,50);
    % plot(interp_axis,interp_data); zoom on

    [y,i]=max(interp_data);
    pos=interp_axis(i);
end

    cm2=[cm2;cm];
    laser_wl2=[laser_wl2;laser_wl];
    pos2=[pos2;pos];

cm=cm2;

pixaxis=(1:length(cm));
wlaxis=polyval(coef,pixaxis);
whiteNISTinterp=spline(whiteNIST(:,1),whiteNIST(:,2),wlaxis)';
intensitycal=im_white./repmat(whiteNISTinterp',[size(im_white,1),1]);
intensitycal=intensitycal/max(intensitycal(:));

save calibration_file intensitycal cm;
laser_wl=laser_wl2;
pos=pos2;

disp('Laser Wavelength');
disp(laser_wl);

%% Transform all data and baseline

file = input('Input file details, i.e. dat*asc:  ','s');
file_vector = dir(file);
FileName{8} = input('Input dark filename for data:  ','s');
dark=francisandor([FileName{8} '.asc']);
disp('loading dark');
FileName{7} = input('Input TFORM filename:  ','s');
load(FileName{7});

visispike('dark');
disp('unspike dark');
pause()
im_dark = imtransform(dark.',TFORM,'bilinear');


for i = 1:10;
    fileroot = file_vector(i).name;
    FileName{9} = fileroot(1:end-4);
    spectra.raw = francisandor([FileName{9} '.asc']);
    disp('Loading spectra');
    load calibration_file;
    tic;
    im_dark = imtransform(dark.',TFORM,'bilinear');
    more off;

    % For single spectra
    im_data = imtransform(spectra.raw.',TFORM,'bilinear'); % Correct aberations
    im_data = (im_data-im_dark)./(intensitycal);
    spectra.tformed = im_data(8:254,100:1022);
    tformed = spectra.tformed;
    baselined_spectrum2d = zeros(size(tformed));
    baseline2d = baselined_spectrum2d;
    parfor k = 1:size(spectra.tformed,1)
        [baselined_spectrum,baseline]=GIFTSv3_jd(tformed(k,:)',1); % Baseline Subtraction
        baselined_spectrum2d(k,:)=baselined_spectrum;
        baseline2d(k,:)=baseline;
        disp(k);
    end
    spectra.baselined_spectrum = baselined_spectrum2d;
    spectra.baseline = baseline2d;

    spectra.rshift=cm(100:1022);
```

```
    elapsed_time = toc
    save ([FileName{9} '_tformed'], 'spectra','elapsed_time');
    disp(['Saved' num2str(i)]);
    clear spectra
end

clear

%% Fitting spectra

optim.peakcount = 1;
optim.background.enable = true;
optim.background.order = 1;
optim.background.coeffs = [0,0];
optim.background.fix = [0,0];
optim.background.ulim = [1e19,1e19];
optim.background.llim = [-1e19,-1e19];
optim.peak(1).enable = true;
optim.peak(1).name = {'phosphate v1'};
optim.peak(1).type = 3;
optim.peak(1).params = [960,1,19,.5];
optim.peak(1).fix = [0,0,0,0];
optim.peak(1).ulim = [965,2,30,1];
optim.peak(1).llim = [945,.5,10,0];

MaxIter = 500;
verbose = false;
heightmax = false;
heightfind = false;
basemax = false;
Rleft = 382;
Rright = 431;

file = input('Input file details, i.e. dat*asc:  ','s');
file_vector = dir(file);

for i = 1:size(file_vector,1);
fileroot = file_vector(i).name;
FileName{9} = fileroot(1:end-4);
load(FileName{9});
disp('Loading spectra');

spectra.crystallinity.image=ones(25,247);
spectra.shift.image=ones(25,247);
for j = 1:25
    for k = 1:247
        ydata = squeeze(spectra.GIFTSv3.baselined_spectrum(j,k,:));
        maximum = max(ydata(382:431));
        ydata = ydata'/maximum; % Normalize Spectra
        xdata = spectra.rshift;
        [estimate, output,peaks,iter,chisq,exitcode] =
gramscurvefit_1_4(ydata,xdata,Rleft,Rright,optim,MaxIter,verbose,heightmax,heightfind,bas
emax);
        spectra.crystallinity.image(j,k) = output.peak(1).finalparams(3);
        spectra.shift.image(j,k) = output.peak(1).finalparams(1);
        disp(k);
    end
    disp(j);
end
figure(1);
surf(spectra.crystallinity.image(1:24,94:139));
figure(2);
surf(spectra.shift.image(1:24,94:139));
pause(2);
save ([FileName{9}], 'spectra');
disp(['Saved' i]);
end

%% Statistics
```

```
file = input('Input file details, i.e. dat*asc:  ','s');
file_vector = dir(file);

crystallinity = ones(2,size(file_vector,1));
shift = ones(2,size(file_vector,1));
xsize = 24;
ysizehi = 130;
ysizelo = 100;

for i = 1:size(file_vector,1);
fileroot = file_vector(i).name;
FileName{9} = fileroot(1:end-4);
load(FileName{9});

coefs = xlsread('crystallinity_calibration.xls');

crystallinity(1,i) =
median((1./reshape(spectra.crystallinity.image(1:xsize,ysizelo:ysizehi),1,xsize*(ysizehi-
ysizelo+1))-coefs(1,2))./coefs(1,1));
crystallinity(2,i) =
iqr((1./reshape(spectra.crystallinity.image(1:xsize,ysizelo:ysizehi),1,xsize*(ysizehi-
ysizelo+1))-coefs(1,2))./coefs(1,1));

shift(1,i) =
median(reshape(spectra.shift.image(1:xsize,ysizelo:ysizehi),1,xsize*(ysizehi-
ysizelo+1)));
shift(2,i) = iqr(reshape(spectra.shift.image(1:xsize,ysizelo:ysizehi),1,xsize*(ysizehi-
ysizelo+1)));
end

crystallinity=[crystallinity(:,17:25),crystallinity(:,1:15)];
shift=[shift(:,17:25),shift(:,1:15)];

compiled.crystallinity = crystallinity;
compiled.shift = shift;
save compiled compiled


matlabpool close
```